Performance of nickel base superalloy components in gas turbines

Dahl, Kristian Vinter

Publication date:
2006

Document Version
Publisher's PDF, also known as Version of record

Performance of nickel base superalloys in gas turbines

Ph. D. Thesis

February 2006

by

Kristian Vinter Dahl

Department of Manufacturing Engineering and Management

The Technical University of Denmark (DTU)

DK-2800 Kgs. Lyngby, Denmark

Preface

The present thesis is submitted in candidacy for a Ph.D.-degree from the Technical University of Denmark (DTU). The work presented in this thesis was carried out under supervision of Professor Andy Horsewell and Affiliated Professor John Hald during the period September 2002 to January 2006 at the Department of Manufacturing Engineering and Management.

The project was financed by Danish power company Energy E2, which is gratefully acknowledged.

Kgs. Lyngby 9/2/2006 Kristian Vinter Dahl

Acknowledgements

First I would like to thank my two supervisors John Hald and Andy Horsewell who have been excellent throughout the whole period of my study. Thank you for your support, many interesting discussions and for always being interested in my work.

I would also like to thank all the members of my monitoring group; Niels Jørgen Markworth and Søren Limkilde Hansen from Energy E2 and Niels Henriksen and Rasmus Berg Frandsen from Elsam. A special thanks to Niels Jørgen Markworth for providing interesting case problems from the Danish gas turbines, some of which have made it into this final thesis.

Also thanks to:

All my colleagues at the department for providing a nice atmosphere.

Steffen Munch, Flemming B. Grumsen, Anette Hansson and Hilmar Danielsen for nice discussions and help with specimen preparation and TEM investigations.

My officemate Thomas Christiansen and Allan Stojko for many good conversations both scientific and social.

My family for all their support.

Abstract

The topic of this thesis is the microstructural behaviour of hot section components in the industrial gas turbine.

The major part of the work treats the interdiffusion between a Co-36.5Ni-17.5Cr-8Al-0.5Y, MCrAlY coating and the underlying IN738 superalloy. The main purpose of the investigation was to develop reliable methods for the estimation of metal temperature of service exposed components from the observed interface behaviour. The main work on this subject is included in the form of papers in appendices I), II) and III).

Furthermore a number of case studies of the behaviour of hot section components in the Danish gas turbines were performed and are included as part of the main thesis. Two of the case studies *Negative Creep of Ni Superalloys* and *Identification of precipitates in IN792 after long time service exposure* merited a separate treatment and are included as separate papers in appendices IV) and V).

I) A new approach for the measurement of average composition profiles in the scanning electron microscope across the interface between superalloys and coatings was developed. The approach allows for the easy measurement of average profiles even though both coating and superalloy contain a large amount of precipitate phases dispersed throughout the microstructure.

II) The developed measurement approach was then used to quantify the interdiffusion taking place at the interface between a Co-36.5Ni-17.5Cr-8Al-0.5Y, MCrAlY coating and the underlying IN738 superalloy in a large matrix of specimens isothermally heat treated for up to 12,000 hours at temperatures 875°C, 925°C or 950°C. Microstructural investigations and calculated phase fraction diagrams using Thermo-Calc showed that a precipitate free zone formed between the coating and superalloy and grew with time. The width of the growing zone was estimated on the basis of average intensity profiles obtained from experimental x-ray maps measured by energy dispersive spectroscopy in a scanning electron microscope. A simple parabolic growth model was then set up for estimating the metal temperature near the coating/ substrate interface based on the growth kinetics of the precipitate free zone.

Parameters for the model were extracted from measurements of the width of the growing precipitate free zone with time. The developed model was then used to estimate metal temperatures for a service exposed, first stage gas turbine blade from a Danish gas turbine.

III) Finally the multi-phase, multi-element interdiffusion was modelled using the finite difference software DICTRA and compared with the average composition profiles measured across the interface and the general experimental findings from I) and II).

IV) Negative Creep in Nickel base Superalloys

The case concerns the phenomenon negative creep that was found to occur in Nimonic 80A bolts used for fixation of heat shields in the hot gas ducts of Danish gas turbines. The term negative creep is used to describe a time-dependent contraction of a material rather than the extension normally seen during creep tests. The volume contraction is typically caused by a solid-state transformation, in the case of Nimonic 80A, formation of the ordered Ni_2Cr phase after several thousands of service hours.

V) Identification of precipitates in IN792 after long time service exposure

The case paper treats the finding of plate-like precipitates in an uncoated IN792 blade. The precipitates had a morphology that initially pointed in the direction of σ-phase, but advanced microstructural investigations, including the use of focused ion beam milling (FIB) and electron energy loss spectroscopy (EELS) in the transmission electron microscope, established that the precipitates were carbides.

Resume

Emnet for denne afhandling er opførslen af højtemperatur komponenter i industrielle gas turbiner; specifikt de ændringer i mikrostruktur som driftseksponering medfører.

Hovedparten af arbejdet omfatter beskrivelsen af interdiffusion imellem en IN738 superlegering og den pålagte Co-36.5Ni-17.5Cr-8Al-0.5Y, MCrAlY coating. Hovedformålet med undersøgelserne var at finde en konsistent fremgangsmåde til at estimere metaltemperatur af driftseksponerede emner. Hovedresultatet af dette arbejde er inkluderet i form af tre papers i appendiks I), II) og III).

Der er desuden lavet en række mindre case undersøgelser, som er inkluderet i afhandlingens indledende afsnit. To af case undersøgelserne omhandlende negativ krybning af Ni superlegeringer og identifikation af faseudskillelser i IN792 var af et sådant omfang, at de er skrevet som selvstændige papers og er medtaget som appendiks IV) og V).

I) Der blev udviklet en ny fremgangsmåde til at måle kompositions-profiler i scanning elektron mikroskop. Fremgangsmåden gør det muligt på en nem måde at måle middel-kompositions profiler over grænseflader, selv ved tilstedeværelse af store andele af præcipitat-faser.

II) Den udviklede målemetode blev brugt til at kvantificere den interdiffusion, som sker ved grænsefladen mellem en Co-36.5Ni-17.5Cr-8Al-0.5Y coating og den underliggende IN738 superlegering for en stor forsøgsmatrice af emner isotermt varmebehandlet i op til 12.000 timer ved 875, 925 eller 950ºC. Mikrostrukturundersøgelser og fase-fraktionsdiagrammer beregnet i Thermo-Calc viste at en udskillelsesfri zone blev dannet mellem coating og superlegering og at denne voksede parabolsk med tid. Tykkelsen af zonen blev estimeret på basis af gennemsnits intensitets-profiler udregnet fra x-ray maps målt ved energi-dispersiv spektroskopi i scanning elektron mikroskop. En simpel parabolsk vækstlov blev brugt til at estimere metaltemperaturen ved grænsefladen mellem coating og superlegering baseret på vækstkinetikken af den udskillelsesfri zone. Parametrene til modellen blev udregnet fra målinger af tykkelsen af den udskillelsesfri zone som funktion af tid. Modellen blev herefter

brugt til at estimere metaltemperaturer for et første-trins, driftseksponeret turbineblad fra en dansk gas turbine.

III) Interdiffusionen ved grænsefladen blev modelleret ved hjælp af multi-fase og multi-element ”finite-difference” modellering i DICTRA. De simulerede kompositions-profiler blev herefter sammenlignet med målte profiler.

IV) Negativ krybning af Ni superlegeringer

Negativ krybning blev observeret i Nimonic 80A bolte brugt til fiksering af varmeskjolde i danske gas turbiner. Udtrykket negativ krybning bliver brugt til at beskrive den tidsafhængige kontraktion af materiale i modsætning til den forlængelse, der normalt ses ved krybning. Volumen-kontraktionen sker typisk på grund af en fastfase transformation. For Nimonic 80A dannes en ordnet Ni_2Cr fase efter lange driftstider, hvilket medfører en kontraktion.

V) Identifikation af udskillelser i IN792 efter lang driftstid

Case undersøgelse der behandler fundet af nåle-formede partikler i et ikke-coatet IN792 turbine blad. Udskillelserne havde en morfologi, som pegede i retning af σ-fase, men avancerede mikrostruktur-undersøgelser ved hjælp af ”focused ion beam milling” (FIB) og ”electron energy loss spectroskopi” (EELS) fastslog at udskillelserne var karbider.

Contents

List of publications

1. K. V. Dahl, J. Hald and A. Horsewell
Grey-scale conversion x-ray mapping by EDS of multi-element and multi-phase layered microstructures
(Submitted to *Journal of Microscopy* 19/12/2005; included in this thesis as Appendix I)
I performed the experimental work, calculations and wrote the paper.

2. K. V. Dahl and J. Hald
Estimation of Metal Temperature of MCrAlY Coated IN738 Components Based on Interdiffusion Behaviour
(Accepted by *Energy Materials: Materials Science & Engineering for Energy Systems* 26/01/2006; included in this thesis as Appendix II)
I performed the experimental work, calculations and wrote the paper.

3. K. V. Dahl and J. Hald
Modelling of Interdiffusion between MCrAlY coating and IN738 superalloy
(In Manuscript; included in this thesis as Appendix III)
I performed the modeling and wrote the paper.

4a. K. V. Dahl and J. Hald
Negative Creep in Nickel Base Superalloys
(Conference paper, BALTICA VI – Life Management and Maintenance for Power Plants (2004) vol. 1, pp. 329-343; included in this thesis as Appendix IV)

4b. K. V. Dahl and J. Hald
Negativ krybning af Ni superlegeringer
(Conference paper, Materialeopførsel og skadesanalyse; Dansk Metallurgisk Selskab – Vintermødet (2004), pp. 201-218)
(Not included in this thesis because of overlap with 4a.)

4c. K. V. Dahl and J. Hald
Negativ krybning af Ni superlegeringer
(Teknisk Nyt – Special, 2004, 37, pp. 34-36 – In Danish)
(Not included in this thesis because of overlap with 4a.)
I performed the experimental investigations with exception of the dilatometer tests, and I wrote the papers.

5. K. V. Dahl and J. Hald
Identification of precipitates in IN792 after long time service exposure
(In manuscript; included in this thesis as Appendix V)
I made the LOM and SEM investigations and made the calculations. I also wrote the paper.

Introduction

The increased use of natural gas for the production of electricity and heat in Denmark has resulted in an increased number of industrial gas turbines run by Danish power producers. Both operating and maintenance costs of these gas turbines have been higher than expected.

The most critical components in the gas turbine in terms of operating costs and life time expenditure are hot section components such as blades and vanes. These components are manufactured in nickel or cobalt base superalloys with high creep strength, and are also often equipped with protective coatings. During service the hot section components are exposed to the hot gas environment inside the turbine and to mechanical and chemical influences that result in a degradation of the components by creep, fatigue or high temperature corrosion.

The overall purpose with the present project was to gain an increased knowledge about the general performance of the hot section components and the degradation mechanisms that limit their life time. Since most of the damage mechanisms are temperature dependent (oxidation, corrosion, creep etc.), the actual metal temperature of components is an extremely important parameter for life-management. A major purpose with the present work was therefore to investigate methods for the estimation of metal temperature.

The experimental part of the project involved the use of electron microscopy methods to characterise the microstructure of both laboratory samples and service exposed components. Specifically the microstructural changes taking place at the interface between coating and substrate superalloy.

During the course of the project also a number of smaller experimental investigations were carried out when interesting case-scenarios arose during overhauls etc.

The theoretical part of the project involved the use of the experimental data to develop and validate thermodynamic and kinetic models of the microstructural degradation by the use of the modelling software Thermo-Calc and DICTRA.

Nickel base superalloys and their performance in gas turbines

The term superalloy was introduced shortly after World War II and was used to describe a series of alloys intended for service at elevated temperatures of above ~650ºC. The superalloys are usually divided up into three major classes depending on whether it is a nickel-, iron- or cobalt-based alloy. In addition to these elements the superalloys may contain lesser amounts of elements such as Cr, W, Mo, Ta, Nb, Ti, Al, Hf, Nb, Zr, B, and C that all influence the properties of the single superalloy. In the present work mainly the nickel base superalloys are treated and unless specifically mentioned the term superalloy refers to these alloys.

Today the nickel base superalloys are widely used for high temperature components in areas such as aircraft and land-based industrial gas turbines, rocket engines, chemical and petroleum plants. In the gas turbine the superalloys are used for hot section components such as burners, combustion chambers, vanes and blades. These components are the most critical in terms of thermal efficiency, life time expectancy and operating costs.

Fig. 1 shows a schematic drawing of a gas turbine. In all modern gas turbine engines, the engine produces its own pressurized gas by burning natural gas or jet fuel. The heat that comes from burning the fuel expands air, and the high-speed rush of this hot air spins the turbine.

Gas turbine engines are, theoretically, quite simple. They have three parts:
Compressor - Compresses the incoming air to high pressure.
Combustion area - Burns the fuel and produces high-pressure, high-velocity gas.
Turbine - Extracts the energy from the high-pressure, high-velocity gas flowing from the combustion chamber.

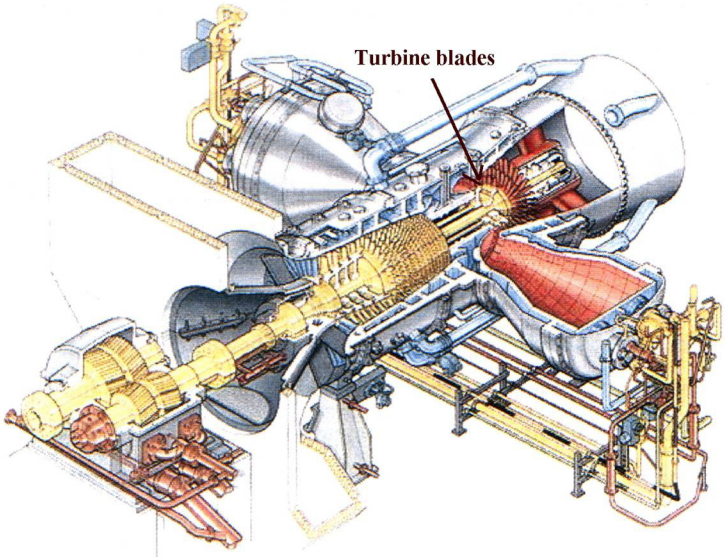

Fig. 1: Schematic drawing of a gas turbine. [1]

A fundamental feature of the gas turbine is that a better thermodynamic efficiency can be reached if the turbine inlet temperature is increased. The upper limit for the temperature is decided by the capability of the materials used for the hot section components.

During service, modern turbine blades can be exposed to gas temperatures exceeding 1600ºC and to both mechanical and chemical degradation in the form of creep, fatigue, oxidation or high temperature corrosion. The continuous evolution of base alloys, protective coatings and component design making this possible has been truly astounding.

In the following a short overview of development in nickel base superalloys and coatings for gas turbines is presented, followed by a number of case studies illustrating some of the challenges encountered in the industrial gas turbine.

Historical development of nickel base superalloys[2,3]

The history of the nickel base superalloys starts with the patent of Marsh [4] from 1906. Marsh discovered that an alloy consisting of Ni with addition of Cr had excellent oxidation resistance at elevated temperatures and that it was well suited for use in electrical heating elements. In the 1920s it was discovered that this alloy had an improved creep strength compared to other materials known at the time [5]. The first reference to a Ni-based alloy containing Al is a patent filed by Heraeus Vacuumschmelze A.G. in 1926 [6]. The alloys described in the patent were specifically claimed for the use as gas- and steam turbine blades,

but no reference to precipitation hardening was mentioned, even though the aluminium content would have made this possible with the correct heat treatment. The use of small additions of titanium and aluminium for precipitation hardening was reported in 1929 by two independent research groups [7 and 8]. In 1940 a patent was filed by L.B. Pfeil [9] of the Mond Nickel Company Ltd. for an alloy with a base composition of at least 20% nickel, 0-30% Cr, 0-9% Co, 0-60% Fe and 0-0.25% C, with additions of 1.5-5% Ti, Mo and W up to 20% and other elements up to 10% permitted. Also a special claim was included for alloys containing up to 5% Al. The heat treatment for the alloy involved a solution treatment at 900ºC followed by fast cooling and then a stabilization at or above the intended service temperature. The alloy was named Nimonic 800 (later Nimonic 80) and was initially made to meet requirements set up by Frank Whittle for turbine blades for his Whittle engine. The first flight of a Whittle gas turbine engine took place in 1941, with nickel alloy turbine blades operating at a gas temperature of 800ºC [10].

Continued alloy development lead to the introduction of an improved version of the Nimonic 80 alloy in 1944, which was then called Nimonic 80A. The Nimonic 80A alloy contained an increased amount of aluminium and was one of the first alloys to really exploit significant age hardening. It was however not discovered until many years later that the precipitates behind this hardening effect were an intermetallic $L1_2$ ordered Ni_3(Al, Ti) phase precipitating coherently with the FCC matrix phase. Today this phase, known as γ' is recognized as one of the most important constituents of modern Ni base superalloys. The early Nimonic alloys also contained limited amounts of carbon allowing secondary carbides to form at grain boundaries. Thus the primary strengthening mechanisms of modern Ni based superalloys were already in place 60 years ago even though they were not fully understood. The microstructure of the Nimonic 80A alloy can be seen in Fig. 2.

Work on wrought alloys continued up through the 1960s but the temperature capability of the wrought alloys was limited by severe metal working difficulties for alloys containing more than approximately 40% γ'. Internal air cooling for components in the hottest sections was beginning to find use, but was also difficult, since the holes had to be drilled out. Investment casting solved both these problems. Fig. 3 shows the evolution in microstructure going from wrought Nimonic 80A to the cast Mar-M-246.

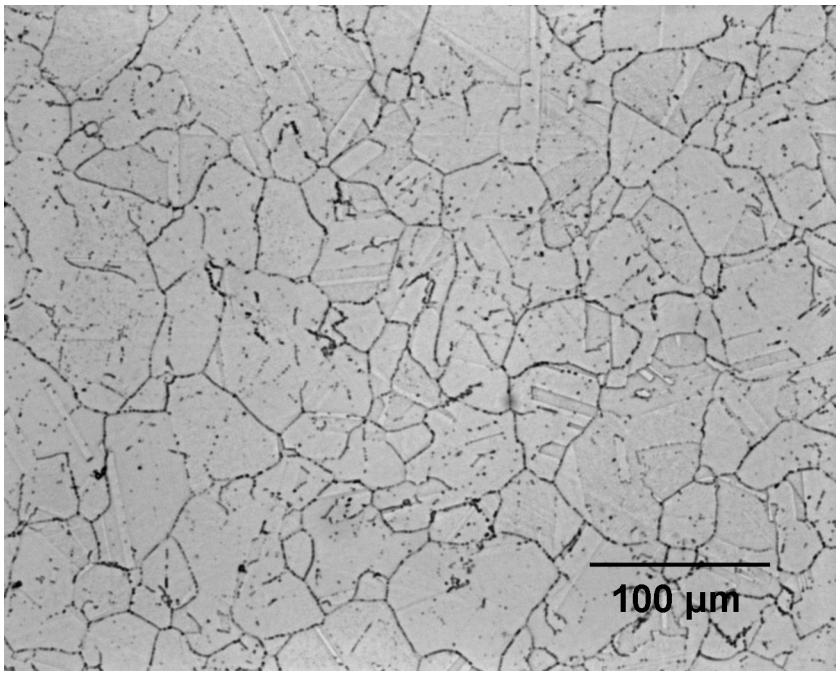

Fig. 2: Microstructure of wrought Nimonic 80A etched to reveal carbides.

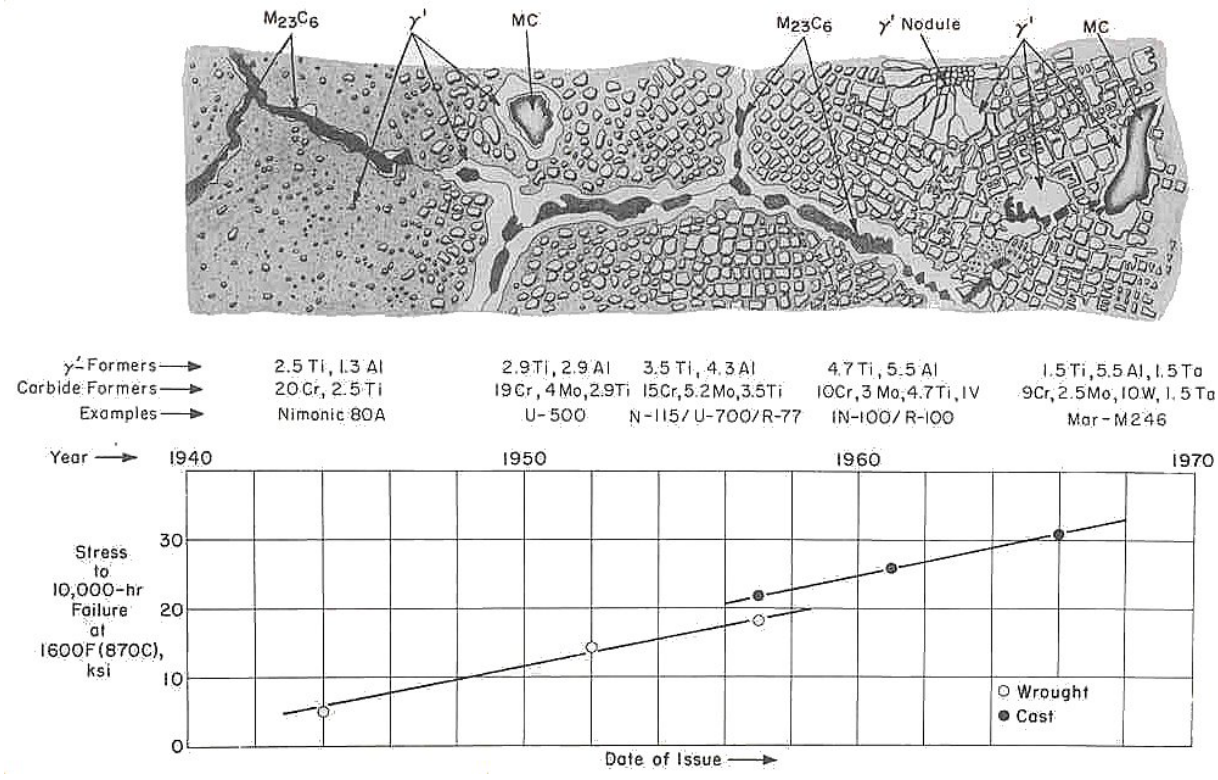

Fig. 3. Genesis of nickel alloy microstructure, 1940-1970, 5000X. Plot shows stress capability of the alloys as a function of approximate date of issue. Structure shown is heat treated for best rupture properties, major features only. Compositions are generalized and typical. [11]

Conventionally cast alloys

Casting initially lead to development of alloys like IN100 that had a high volume fraction of γ'. To maximize the high temperature strength, Cr content was reduced, since increase in Cr content leads to a decrease in γ'-solvus temperature. The low Cr content did however have the downside effect that resistance against hot corrosion was significantly lowered [12]. Thus two different trends in superalloy development was introduced: The first being the singular pursuit of high temperature capability and thus low Cr contents, and the second aiming to achieve good high temperature capability together with good hot corrosion resistance by maintaining a moderately high Cr content [11]. The second trend led to the development of the popular IN738 alloy that is still in use in many applications to this day.

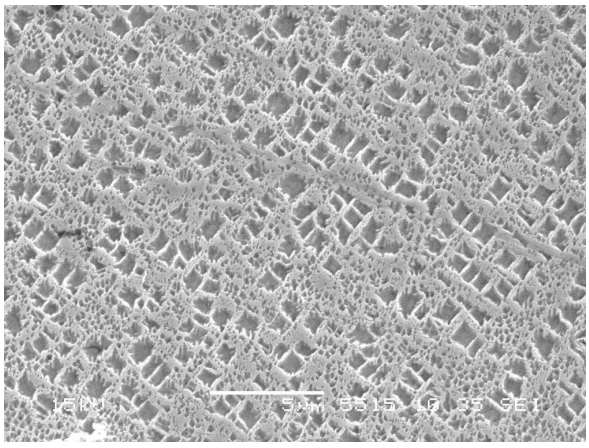

Fig. 4. Bulk microstructure of an IN738 precipitation hardened nickel-based superalloy; The γ'-phase has been etched. The initial heat treatment has resulted in a bimodal γ' distribution in the virgin condition.

A severe problem encountered in some of the early cast alloys was the precipitation of intermetallic phases like σ and μ that occurred after long service hours. The precipitation of σ-phase in IN100 was described by Wlodek [13]. The precipitation is unwanted since it has a deleterious effect on toughness because needle shaped particles may act as sites for crack initiation [11]. Careful control of the alloy chemistry is required to avoid compositions favouring the precipitation of these phases.

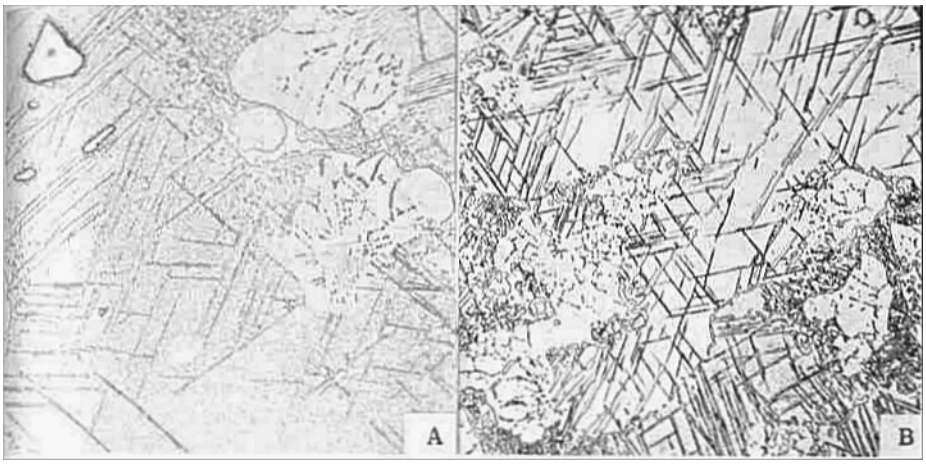

Fig. 5. Precipitation of σ-phase in IN100 [13].

Directionally solidified and single crystal alloys

Versnyder and Guard [14] showed that the creep and rupture properties of superalloy test-pieces could be enhanced by eliminating grain boundaries perpendicular to the stress axis, resulting in a directionally solidified structure. Their findings were then transferred to turbine blades as described in a review paper by Versnyder and Shank [15]. The resulting macrostructure can be observed from Fig. 6. The conventionally cast blade has equiaxed grains that are a few millimetres in diameter, while the directionally solidified blade has columnar grains running through the entire length of the blade. The natural next step was to eliminate all grain boundaries resulting in the single crystal turbine blade also shown in Fig. 6.

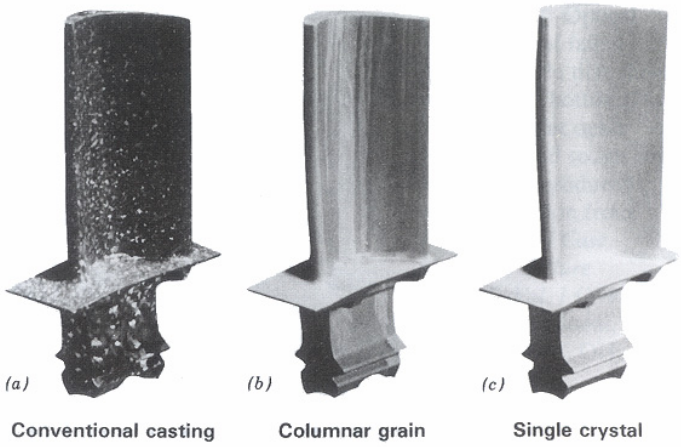

Fig. 6. Equiaxed, directionally solidified and single crystal turbine blade [16].

Casting of the directionally solidified and the single crystal blades is done under close control of the heat flow. Fig. 7 (a) shows a schematic of a common process for directional

solidification. During solidification the dendrites must be made to grow through the length of the casting. This is done by establishing a strong thermal gradient in the temperature range between liquidus and solidus temperatures of the alloy and then passing this gradient from one end of the casting to the other at a rate that maintains the steady state growth of the dendrites. The mold is cooled by withdrawing it from the hot zone as shown in the schematic. The process for manufacturing single crystal alloys is very similar to one used for directional solidification (Fig. 7 (b)), a single grain is selected by a spiral grain selector that permits only the single grain to pass through, and that grain then fills the entire mold cavity.

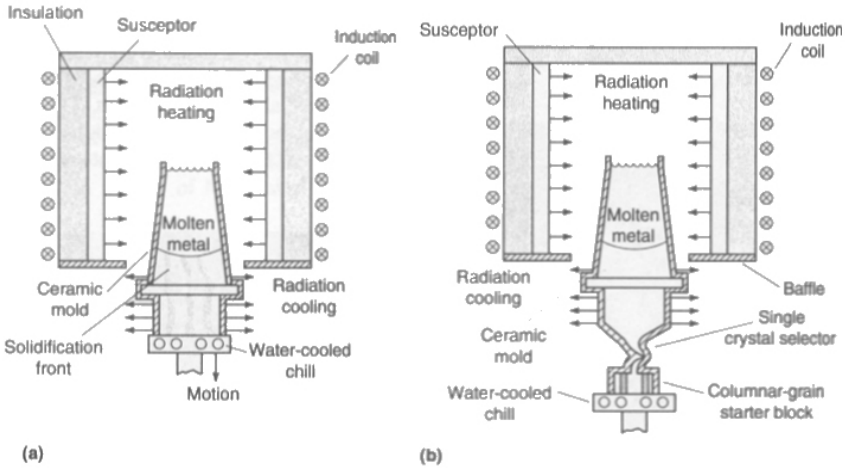

Fig. 7. Schematics of solidification process for (a) directional solidification and (b) single-crystal solidification. [17]

Since the single crystal blades contain no grain boundaries, the grain boundary strengthening elements such as C, B, Zr and Hf are superfluous and can be removed. This allows for a full solution heat treatment of the γ′ otherwise not possible because of the incipient melting temperature of the grain boundary precipitates that lies below the γ′-solvus.

The overall performance of the single crystal blades have improved markedly with the addition of rhenium (second generation (~3 wt% Re) and third generation alloys (~6 wt% Re)). A good review of the evolution of single crystal alloys is given by Caron and Khan [18].

Normal single crystal alloys like the second generation CMSX-4 require expensive multi-step heat treatments in order to obtain the optimum microstructure for high temperature service and also suffer from low casting yields due to casting defects. A recent trend in alloy development has been to reintroduce some of the grain boundary strengthening elements to single crystal alloys. The goal being to manufacture affordable single crystal alloys that offer a bit lower temperature capability but compensates for this with significantly lower

manufacturing costs and also better casting yields because of an increased tolerance against grain boundary defects introduced during casting.

Work on the CM186LC alloy [19] is an example of this. The alloy was originally developed for use in directionally solidified components, but in single crystal form it can be used in the as-cast condition without expensive solution heat treatments (a two stage aging treatment is still applied). Because the CM186LC alloy was originally intended as a DS alloy it contains the grain boundary strengthening elements carbon, boron, hafnium and zirconium. The idea was that these elements would give CM186LC in the single crystal form an increased tolerance against grain boundary defects introduced during casting and thus give a better casting yield. Fig. 8 shows transmission electron microscope images of γ′ in CM186LC.

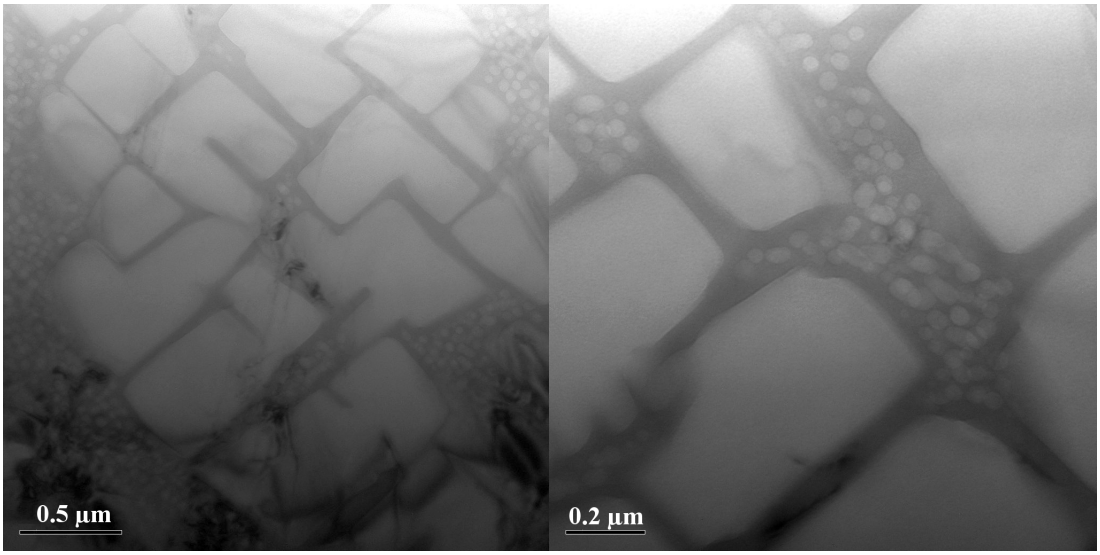

Fig. 8: TEM images of γ′-particles in CM186LC. [20]

Results of creep testing however showed that the CM186LC alloy in the as cast condition could not compete with the CMSX-4 alloy in terms of creep resistance and therefore it could not be used for hot section blading [19]. There is however still interest in this kind of developments.

Fig. 9 shows the microstructure of a CM186LC specimen that has been isothermally heat treated at 1,000ºC for 1,000 hours. Inside the dendrite arms, residual stresses from the casting have resulted in preferential growth of γ′-particles in directions along the dendrite arms.

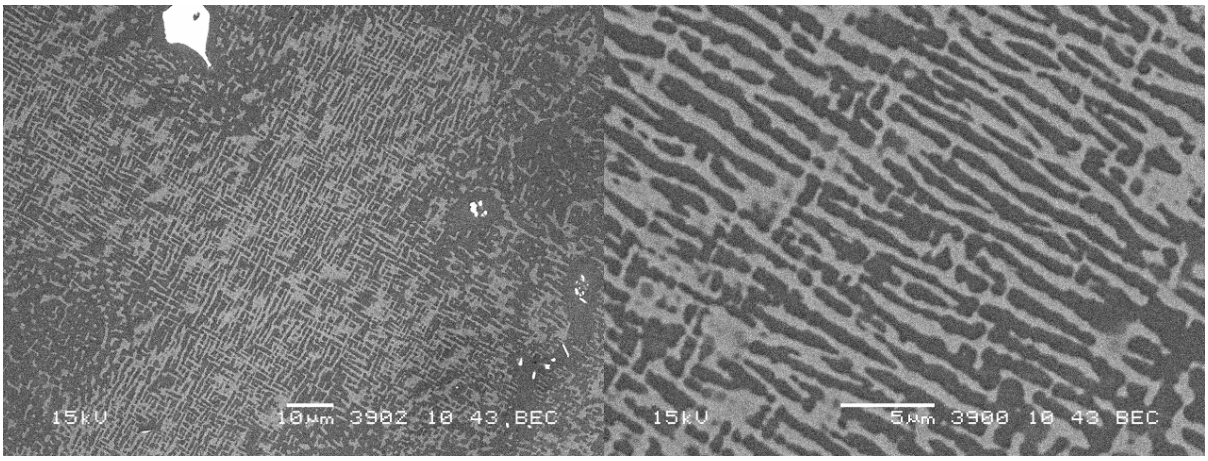

Fig. 9: SEM BSE images of rafting occurring inside the dendrite arms of a CM186LC single crystal alloy. The lack of full solution heat treatment results in an inhomogeneous microstructure with large islands of γ′ in the interdendritic areas. Inside the dendrite arms, residual stresses from the casting have resulted in preferential growth of γ′-particles in directions along the dendrite arms. [20]

Protective Coatings

The resistance of the nickel base superalloys against the aggressive environment in the gas turbine and against degradation mechanisms such as oxidation and hot corrosion depends on formation of Cr_2O_3 or Al_2O_3 protective oxide layers at the surface. The layers formed depend on the chemical composition of the specific superalloy in question and of course especially on the content of chromium and aluminium. For many purposes the inherent resistance against oxidation and hot corrosion is not sufficient and therefore protective coatings are applied.

For the first stages of turbine blades, coated nickel base superalloys have been the material of choice since the 1960s. Since then significant advances have been made not only to the base material but also to the applied coatings, beginning with simple aluminides, followed by modified aluminides with addition of elements such as Si, Cr and Pt, then MCrAlY overlay coatings, and finally ceramic thermal barrier coatings on top of a metallic bond-coat. Excellent historical reviews can be found in the work of M. J. Pomeroy [21], and J. R. Nicholls [22].

Today the focus is not only separately on coatings or on the underlying superalloy substrates but instead on integrated coating/ superalloy systems where the two components are designed to fit each other. On top of being able to protect the base alloy from oxidation and hot corrosion the coating also has to be both mechanically and chemically compatible with the bulk alloy. Start/ stop cycles may cause the coating to crack or spall if there are differences in

heat expansion coefficient and excessive interdiffusion may cause loss of protective elements such as aluminium and chromium through diffusion from coating into the bulk alloy.

A typical coating system could consist of either a Pt modified Al-diffusion bond-coat or a MCrAlY bond-coat with an outer thermal barrier coating (TBC), consisting of tetragonal zirconia stabilised by yttrium [23]. The choice of specific coating will depend both on the underlying superalloy and the surrounding environment (temperature, gas-composition etc.). Fig. 10 shows the relative resistance of coatings against the two major degradation mechanisms; oxidation and hot corrosion. Generally high chromium content is favourable in environments where hot corrosion conditions can be expected and high aluminium content is favourable in high temperature oxidising environments (see Fig. 10).

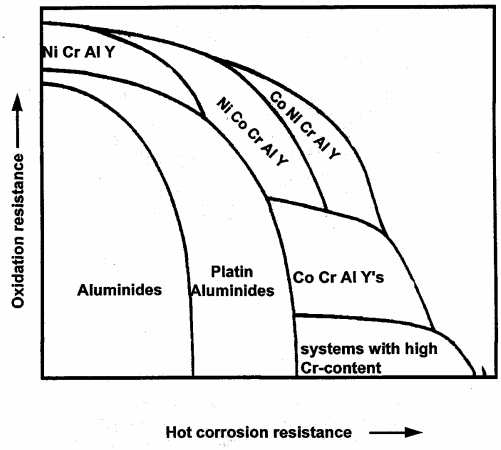

Fig. 10: Relative oxidation and corrosion resistance of coating systems. [24,25]

Fig. 11 shows a TBC coating on top of a PtAl diffusion bond-coat applied to a CM186LC single crystal superalloy. The TBC coating consists of a ceramic layer that acts as an insulator protecting the underlying material from the extreme temperatures in the gas. The underlying bond-coat then protects against oxidation. The insulating effect of the TBC combined with internal cooling enables the underlying superalloys to be used at gas temperatures above their melting points [26].

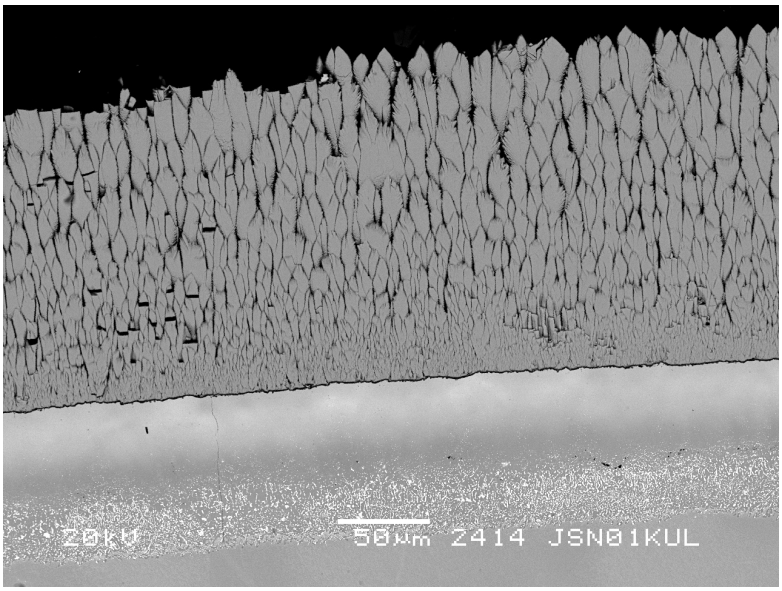

Fig. 11. CM186LC alloy with PtAl bond-coat and thermal barrier coating. [20]

References

[1] Information material on the V64.3 gas turbine from Siemens, Svanemoellevaerket, 1998.
[2] W. Betteridge and J. Heslop: *The Nimonic Alloys – Second edition*, Edward Arnold (Publishers) Limited 1974, 7-22.
[3] A. Strang, J. Cawley and G.W. Greenwood. (Editors): *Microstructural Stability of Creep Resistant Alloys for High Temperature Plant Applications*, IOM Communications Ltd. 1998, 27-47.
[4] A.L. Marsh: UK Patent 2129, 1906.
[5] H.J. Tapsell and J. Bradley: Engineering, **120**, 1925, 614-615.
[6] Heraeus Vacuumschmelze A.G.: UK Patent 286 367, 1926.
[7] Soc. Anon. de. Commentry, Fourchambault et Decazeville: UK Patent 286 367, 1929.
[8] N.B. Pilling and P.D. Merica: US Patents 2 048 163 – 2 048 167, 1929.
[9] L.B. Pfeil: UK Patent 583 162, 1940.
[10] T.A. Taylor: *Proc. Inst. Mech. Eng.*, **153**, 1945, 505-512.
[11] C.T. Sims and W.C. Hagel: The Superalloys, John Wiley and Sons, Inc. 1972, p. 37.
[12] W. Betteridge, S. W. K. Shaw: *Materials Science and Technology*, 1987, **3**, 682-694.
[13] S.T. Wlodek, Trans. ASM, 1964, **57**, 110-119.
[14] F. L. Versnyder and R. W. Guard: *Trans. ASM*, 1960, **52**, 485-493.
[15] F. L. Versnyder and M. E. Shank: *Materials Science and Engineering*, 1970, **6**, 213-247.
[16] W. D. Callister, Jr.: Materials Science and Engineering – An Introduction, John Wiley and Sons, Inc., 2003, p. 225.
[17] J. R. Davis (editor) Heat Resistant Materials – ASM Specialty Handbook, 1997, ASM International, p. 256.
[18] P. Caron and T. Khan: *Aerosp. Sci. Technol.*, 1999, **3**, 513-523.
[19] D. W. Bale, M. Toulios, E. P. Busso, M. B. Henderson and P. Mulvihill: Procedings of the Sixth International Charles Parsons Turbine Conference 16-18 September 2003, Trinity College Dublin, Ireland. A. Strang et al. (editors). 765-777.
[20] K. V. Dahl and John Hald, Microstructure investigations of CM186LC carried out under the COST 522 project.
[21] M. J. Pomeroy: *Materials and Design*, 2005, **26**, 223-231.
[22] J. R. Nicholls: Procedings of the Sixth International Charles Parsons Turbine Conference 16-18 September 2003, Trinity College Dublin, Ireland. A. Strang et al. (editors). 803-826.
[23] G. W. Goward: *Surface and Coatings Technology*, 1998, **108-109**, 73-79.
[24] H. W. Grünling, H. Rechtenbacher and L. Singheiser: *Materials Science Forum*, 1997, **251-254**, 483-502.
[25] A. J. A. Mom, internal reference included as reference 4 in [12].
[26] D. Clarke and S. R. Philpot: *Materials Today*, June 2005, 22-29.

Performance of Ni-superalloy components in Danish gas turbines

During the course of the present project a number of smaller studies were done as a natural part of learning about the behaviour of Ni base superalloys in the gas turbine.

The studies include examples of microstructural degradation happening as an effect of normal service in industrial gas turbines but also include examples of catastrophic failures due to effects such as excessive oxidation, hot corrosion, negative creep and unexpected phase precipitation. The case studies therefore nicely illustrate some of the many challenges that hot section components in modern gas turbines have to face and overcome. Table 1 shows average compositions of selected superalloys, some of which were directly investigated in the case stories that follow, others are shown for comparison.

Table 1: Composition of a selection of Ni base superalloys in weight %.

	B	C	Al	Ti	Cr	Fe	Co	Ni	Zr	Nb	Mo	Hf	Ta	W	Re
Nimonic80A		0.05	1.4	2.25	19.5	1.5	1.0	bal		-	-		-	-	
IN738LC	0.01	0.11	3.4	3.4	16.0		8.5	bal	0.045	0.85	1.75		1.75	2.6	
IN792	0.015	0.08	3.5	3.9	12.4		8.9	bal			1.9	0.5	4.2	3.9	
Mar-M-247	0.015	0.16	5.6	1.0	8.5		10.0	bal	0.04		0.7	1.4	3.0	10.0	
Mar-M-421	0.015	0.14	4.3	1.8	15.8		9.5	bal	0.06		2.0			3.8	
CM186LC	0.015	0.069	5.7	0.7	6.0	0.065	9.3	bal	0.006		0.5	1.4	3.4	8.4	2.9
CMSX-4	<0.002	0.002	5.7	1.01	6.4	0.03	9.6	bal	<0.001	<0.05	0.61	0.1	6.5	6.4	2.9

The case studies included in this chapter are

a) Hot Corrosion of IN738
b) Oxidation and Thermal Fatigue of Mar-M-247 Blades
c) Braze Repair of IN738 V64.3 2nd Stage Blade

a) and b) are examples of degradation happening during service while c) is an unlucky example of a failure happening while trying to repair a blade.

Two case studies merit separate treatment, i.e. Negative creep of Nimonic 80A and the identification of precipitates in IN792 after long time service. These are included as papers in appendices IV) and V).

IV) Negative Creep of Ni Superalloys

The case paper was inspired by a failure of turbine bolts used for fixation of heat shields. The failure was observed in German gas turbines and as a result investigations were done for similar bolts in Danish gas turbines. A literature study and following detailed microstructural investigations revealed that after long service hours in a specific temperature regime an ordering transformation in the Nimonic 80A alloy and in the actual bolts resulted in a volume contraction. The case is an example of the complex and sometimes unexpected microstructural changes that can take place in superalloys after long service hours.

V) Identification of precipitates in IN792 after long time service exposure

This is another example of phase-precipitation occurring after long service hours. A large amount of plate-like precipitates were found beneath the outer oxide layer of an uncoated IN792 turbine blade. The morphology of the precipitates initially led to the wrong conclusion that the precipitates were σ-phase. State of the art microstructural investigations using focused ion beam milling (FIB) to make a thin foil from the local area where the precipitates were found, followed by electron energy loss spectroscopy (EELS) analysis in a transmission electron microscope revealed that the precipitates were actually carbides formed by inward diffusion of carbon.

Hot Corrosion of IN738

A degradation phenomenon that can lead to catastrophic failure of gas turbine components manufactured in nickel base superalloys is hot corrosion. Hot corrosion is a chemically assisted attack that is a result of an aggressive environment. The hot corrosion phenomenon is closely associated with the presence of salt contaminants such as Na_2SO_4 and/ or NaCl, which in combination can form low melting point deposits that dissolve protective oxides [1]. The source of the salts can be either direct ingestion of sea salt in a marine environment or for instance the formation of Na_2SO_4 from combustion of fuels containing both sodium and sulphur [2].

The hot corrosion phenomenon is usually split up into two different types; a high temperature hot corrosion (type I, 800-950ºC) and a low temperature hot corrosion (type II, 600-800ºC) [3].

For type I hot corrosion, the temperature is above the melting point of the salts, while the low temperature type II first involves the formation of a eutectic mixture with low melting point, such as cobalt/sodium or nickel/sodium sulphates.

The example included is not a classic case of hot corrosion, but is a very unfortunate case of high temperature corrosion in large IN738 blades from a Danish gas turbine. During an overhaul the original coating on the blades was stripped using a chemical agent and the blades were then recoated. Remnants of the chemical agent were however left inside the cooling channels when the blades were again put into service and while the blades were effectively protected on the outer surface by the applied coating, the internal surfaces were heavily attacked.

During a following routine inspection one of the blades were cut up, and large cracks (see Fig. 1) running in grain boundaries were found. Some of the cracks ran almost through the whole cross section of the blades.

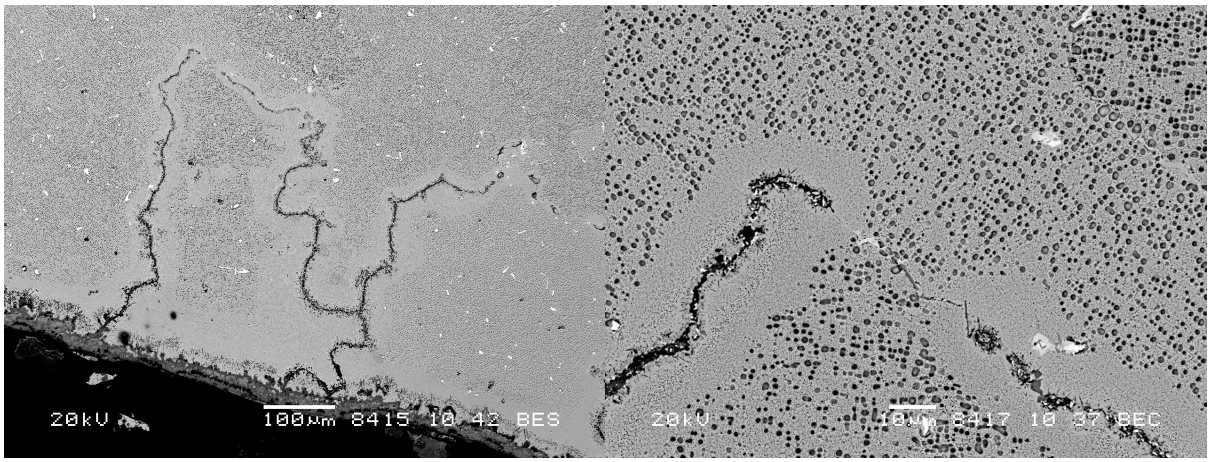

Fig. 1: SEM BSE images of chemically assisted corrosion attack in grain boundaries of an IN738 turbine blade.

References

1 J.R. Nicholls et al.: *Surface and Coatings Technology*, 2001, **149**, 236-244.

2 C.T. Sims and W.C. Hagel: The Superalloys, John Wiley and Sons, Inc. 1972.

3 G. W. Goward: Surface and Coatings Technology, 1998, **108-109**, 73-79.

Oxidation and Thermal Fatigue of Mar-M-247 Blades

The high temperature oxidation resistance of the Ni base superalloys depends on the formation of a continuous layer of protective oxides such as Al_2O_3 or Cr_2O_3. Often coatings are applied to offer an increased amount of Al or Cr and therefore avoid the formation of non-protective base-material oxides. Depending on the specific composition of a superalloy and of course on the temperature of the surrounding environment an uncoated superalloy will also be able to sustain a protective oxide layer. Outward diffusion of Al and/ or Cr from the bulk superalloy to the oxide layer may however result in a depletion of these elements in the substrate. If the oxide cracks or spalls the bulk superalloy depleted in protective elements will then be exposed directly to the high temperature environment resulting in formation of non-protective base-metal oxides. [1]

During a routine check inspection of the Solar Mars turbine in Hirtshals, Denmark in June 2002 damages to the turbine blades at the first stage of the gas producing turbine were discovered and two specimen blades were sent to the Department of Manufacturing Engineering and Management (IPL) at the Technical University of Denmark (DTU).

Fig. 2: Turbine blades with surface defect.

The blades had a service time of 10,879 hours with 823 start/ stop cycles. The temperature just before the first vanes was 970ºC and the actual temperature at the blades has therefore been below this temperature.

The turbine blades were reported to be produced from the high temperature nickel alloy Mar-M-421, but EDS composition measurements revealed that the actual composition was closer to that of Mar-M-247 that has a significantly lower Cr-content.

Table 2: Nominal and measured compositions

	Al	Ti	Cr	Fe	Co	Ni	Mo	Hf	Ta	W	C	Zr	B
Mar-M-421	4.3	1.8	15.8		9.5	62.59	2.0			3.8	0.14	0.06	0.015
Measured	4.9	1.0	8.7	<1.0	10.1	58.7	<1.0	1.4	3.7	10.7			
Mar-M-247	5.6	1.0	8.5		10.0	59.64	0.65	1.4	3.0	10.0	0.16	0.04	0.015

All values in Weight Percent

Inside the cooling channels of both blades heavy oxidation was observed (Fig. 2). This oxidation was the cause for the blade failure and the surface defect on the damaged blade. The oxidation happened in a corner where relatively poor cooling can be expected due to specimen geometry. Since the failure was caused by oxidation inside the cooling channels, the oxidation resistance of the matrix material and not the external coating became critical.

For protection against oxidation the Mar-M-247 alloy relies on its high aluminium content. It does however not seem like the aluminium alone could provide sufficient protection in the relatively cool environment inside the cooling channels. The original Mar-M-421 with higher chromium content would therefore have been a safer choice.

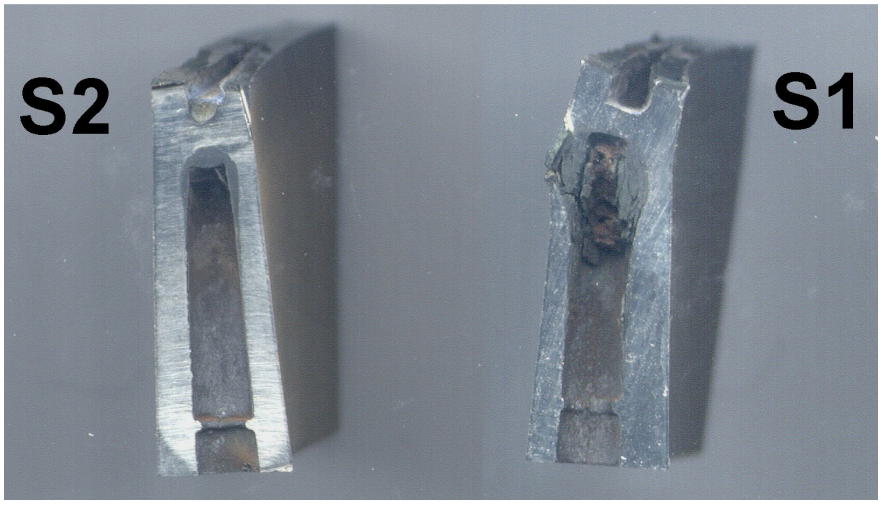

Fig. 3: Heavy oxidation inside the cooling channels of the blades shown in Fig. 2.

The outer protective coating on the blades was a Pt/Al diffusion coating. Along the geometry of the blades several cracks in the coating was found on both blades. The cracks shown in Fig. 4 were found at locations thought to be relatively cool judged from general coating condition and are most probably the result of thermal fatigue due to repeated start/ stop cycles. There

were no signs of oxidation or accelerated attack in the bottom of the cracks, but this could occur at a later stage, and the cracks are therefore potentially quite dangerous.

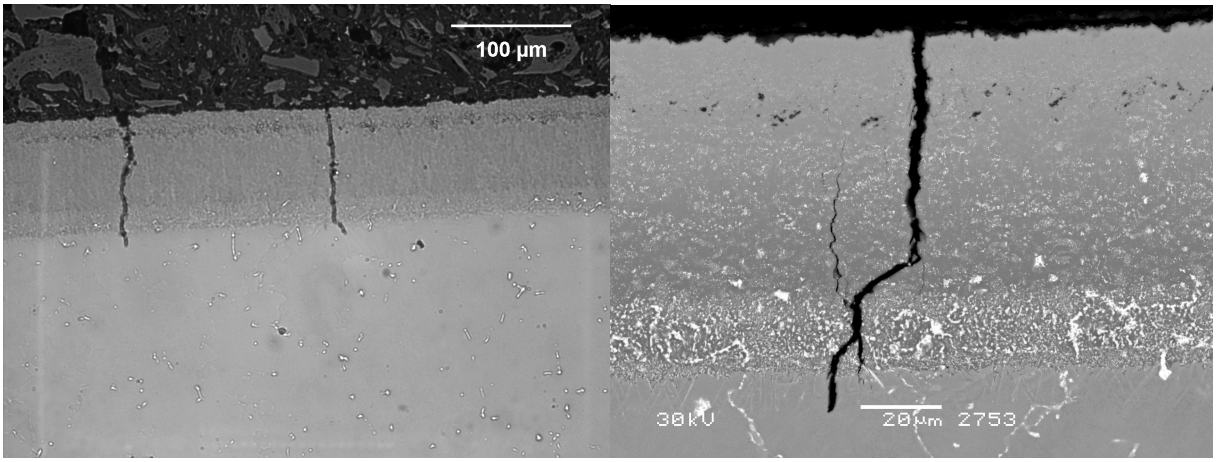

Fig. 4: Left: LOM image of thermal fatigue cracks running all the way through the applied coating. Right: SEM BSE image of a crack.

Summation of case

This small case very nicely illustrates the importance of correct material choice for a specific application. The choice of alloys containing low amounts of Cr may increase the creep strength of an alloy but must be offset against decreased resistance against the surrounding environment in the turbine. In the present case the high aluminium content that offers high temperature oxidation resistance for the Mar-M-247 alloy is not adequate for the intermediate temperature range inside the cooling channels where an alloy with higher chromium content had been a better choice.

References

1 M. J. Bennett, A. J. Tuson, C. F. Knights and C. F. Ayres: *Materials Science and Technology*, 1989, **5**, 841-852.

Braze Repair of IN738 V64.3 2nd Stage Blade

Background

During service, blading components are exposed to severe temperatures and stresses that may result in thermal fatigue cracking of the base material. Braze repair is an important tool for restoration of such cracked or eroded blades. Small cracks can be repaired by diffusion brazing. Diffusion brazing is done at a high temperature where a braze alloy containing a melting point depressant such as boron with the help of capillary effects flows into the crack to be repaired. The braze alloy is then isothermally solidified by diffusion of the melting point depressant (boron) into the parent metal. As boron diffuses into the parent material the solidification front will move in the opposite direction. It is important that the solidification is done isothermally to avoid precipitation of brittle phases (borides).

Case

During a high temperature braze repair a single IN738 blade collapsed and had to be discarded as scrap. Fig. 5 shows the damaged blade before sectioning for metallurgical analysis. It was speculated that the blade had already previously had a high temperature braze repair, and that it collapsed due to the presence of an excessive amount of temperature suppressant like boron.

Fig. 5: The damaged IN738 blade

Two cross-section specimens from the leading edge and trailing edge of the blade respectively were analysed in the light optical microscope and in the scanning electron microscope for EDS composition analysis. The measured compositions were then compared to results of thermodynamic modelling using Thermo-Calc [1] with the database Ni-DATA v. 4 developed by Thermotech Ltd. [2].

Microstructural investigations

Investigation in the light optical microscope (LOM) revealed a large amount of intermetallic phases near the outer surface.

The images presented in Fig. 6 show the leading edge at the point where the cross sectional thickness (from the outer surface to the inner cooling hole surface) is smallest. A large fraction of intermetallic-phases have precipitated at grain boundaries and it looks as though material has fallen of from the inside of the cooling hole. The γ′-particles that are usually seen in the IN738 alloy and give it strength are not present in thin sections and areas near the surface, which corresponds nicely with the assumption that the blade has received a short time, high temperature braze repair.

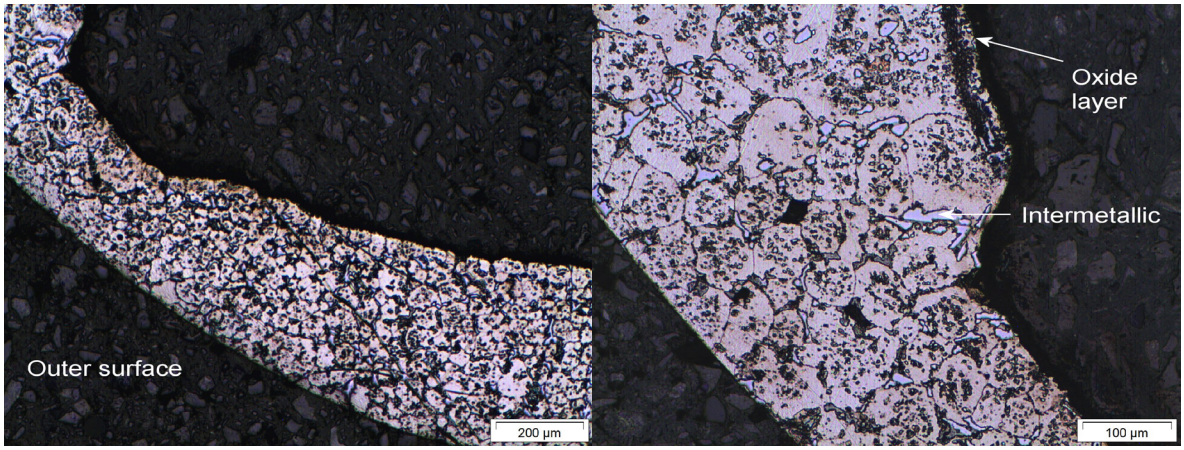

Fig. 6: LOM images of a thin section near a cooling channel at the leading edge of the blade.

Compositions of intermetallics and surrounding matrix were measured by EDS spot analysis and the results are included in table 3.

Table 3: SEM EDS composition measurements (weight %).

	Al	Ti	Cr	Co	Ni	Nb	Mo	Ta	W
Intermetallic*			73.8	3.2	4.8		8.2		10.0
Matrix*	3.8	1.6	12.0	9.6	69.0	0.3	0.8	1.1	1.8
Area	2.8	3.2	16.4	8.5	61.3	0.5	1.9	2.0	3.4

*The listed compositions are an average of at least four different measurement points.

Table 4: Calculated phase compositions at 1100 ºC (weight %) (Fig. 8).

	Al	Ti	Cr	Co	Ni	Nb	Mo	Ta	W	B	C
FCC	2.8	2.9	11.5	9.9	66.6	0.4	-	1.8	4.0	0.011	0.0036
γ´	5.9	6.8	2.1	5.9	72.7	1.2	-	3.8	1.6	-	-
MC	-	36.0	0.05	-	0.006	9.5	-	34.3	7.2	0.0007	12.5
Cr_5B_3	-	-	71.0	-	-	-	18.9	-	-	10.1	-

The large particles are very rich in chromium and also contain significant amounts of molybdenum and tungsten. The compositions lie very close to compositions that would be expected for chromium rich $M_{23}C_6$ carbides. $M_{23}C_6$ carbides are however not normally present at the high temperatures where braze repair is performed. According to the Thermo-Calc calculation shown in Fig. 7, $M_{23}C_6$ is not thermodynamically stable above 1000ºC where a braze repair will typically take place. The areas that have received the braze repair does not deviate much from the bulk composition making it reasonable to assume that the braze alloy used was very close to the bulk material in composition, with an element such as boron used as temperature suppressant.

In order to simulate a case where an excessive amount of boron was present, which could be the case if the blade has had multiple high temperature braze repairs, an equilibrium Thermo-Calc calculation was done for the same composition as Fig. 7 but with addition of 1 wt% boron. The calculations show that a Cr-rich boride (Cr_5B_3) is thermodynamically stable in the temperature regime where a high temperature braze would be performed. Calculated phase compositions at 1100ºC is included in table 4 and show that the Cr_5B_3 is rich in Cr and Mo as also seen in the EDS measurements. It therefore seems likely that the intermetallic phases could be borides.

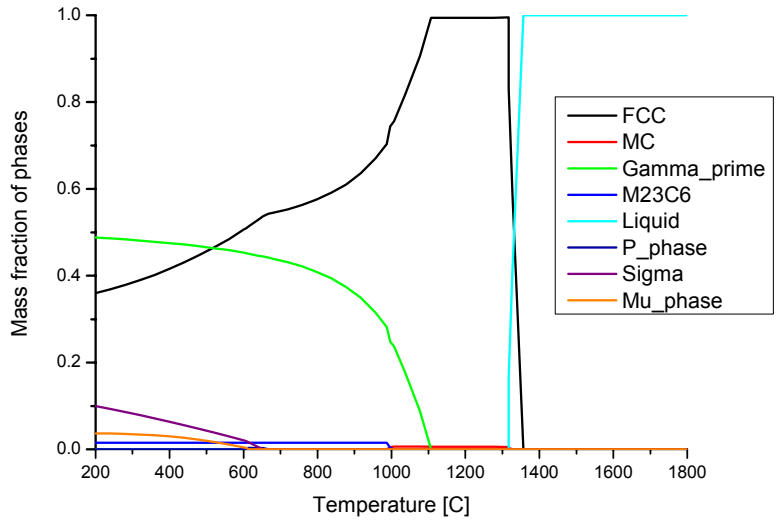

Fig. 7: Calculated phase fractions from the measured "area" composition and 0.08 wt% C.

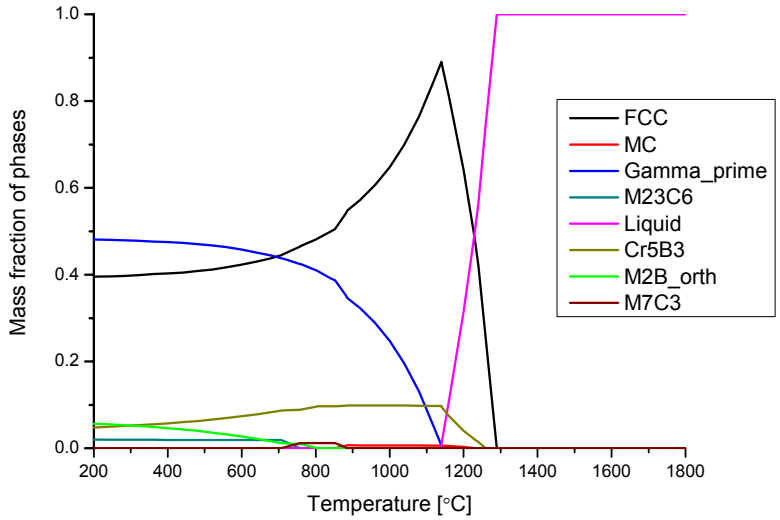

Fig. 8: Same calculation as performed for Fig. 7 but now with addition of 1wt% B.

Summation of case

It is apparent that the blade has had a high temperature braze repair and it seems that the repair has resulted in the precipitation of a large amount of intermetallic phases in grain boundaries near the surface of the blade. At the surface whole grains have fallen of, which may be explained by the presence of the intermetallic phases, if these have a low melting point.

From the EDS composition measurements and thermodynamic equilibrium calculations using Thermo-Calc it seems likely that the intermetallic phases are borides that have formed during the high temperature braze repair. This could happen if an excessive amount of boron was present.

Based on the available information it was however not possible to say whether the excessive amount of boron would be present because of a faulty high temperature braze repair or because the blade has previously had another braze repair resulting in a high amount of boron already being present in the blade.

References

1 B. Sundman, B. Jansson and J. -O. Andersson: *Calphad*, 1985, **9** (2), 153-190.

2 N. Saunders: *SUPERALLOYS 1996 - Procedings of the Eight International Symposium on Superalloys*, Champion, Pennsylvania, 1996, 101-110. Edited by R. D. Kissinger et al.

Estimation of metal temperature

The metal temperature is an extremely important parameter for the life-management of hot section components, since most of the damage mechanisms are temperature dependent (oxidation, corrosion, creep etc.). Because of the complex design of hot section components such as turbine blades (aerodynamic shape and internal cooling systems) large temperature differences are found for different locations in a blade. This makes direct measurement of the metal temperature near to impossible for most cases and instead sophisticated methods for estimating the temperature from the microstructure of service exposed components have been developed.

In the work presented in [1] later in this thesis the measured width of the interdiffusion zone between IN738 and a MCrAlY coating is used to estimate the metal temperature of a service exposed component. In the same way coarsening of γ´-particles can be used to estimate the temperature. This was for instance done by Aurrecoechea et al. [2] to estimate the metal temperature of service exposed Mar-M-421 turbine blades.

Coarsening of γ´ in IN738

During high temperature service the microstructure of a nickel base superalloy changes and is degraded in several ways. One of the most common changes noticeable is coarsening of the strengthening γ´-particles with time. The effect of precipitation hardening and therefore also the creep resistance of the nickel base superalloys is closely connected to the size and spacing of the γ´-precipitates, since they work as obstacles for the movement of dislocations. As the size and interspacing between the precipitates increase with time by γ´-coarsening, the creep resistance of the alloy will therefore also change and be degraded.

The γ´-particles precipitate from a supersaturated solid solution during the initial heat treatment that is applied to obtain the optimum microstructure. A typical heat treatment therefore includes a solution treatment at a high temperature and one or more aging treatments at lower temperatures. Fig. 1 shows the virgin microstructure of IN738 after the initial heat treatment. The heat treatment produces a bimodal distribution of small spheroidal γ´-precipitates and larger cuboidal precipitates.

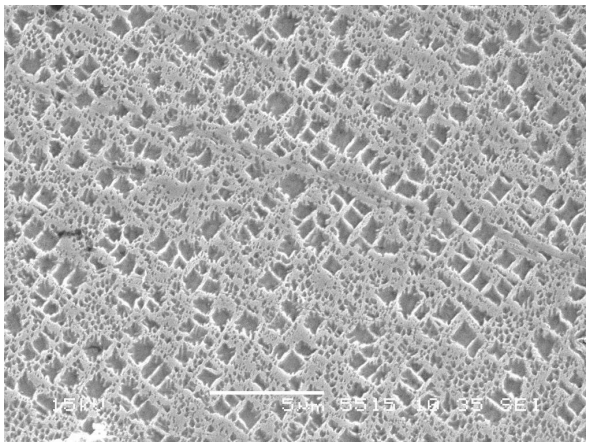

Fig. 1. Initial microstructure of IN738 with bimodal γ´ distribution (SEI); γ´ has been etched.

Fig. 2 shows the microstructure after isothermal heat treatment at 950ºC for 500 and 8,000 hours. It is obvious that a significant change has taken place. Most of the small γ´-particles have dissolved and the large particles have increased in size.

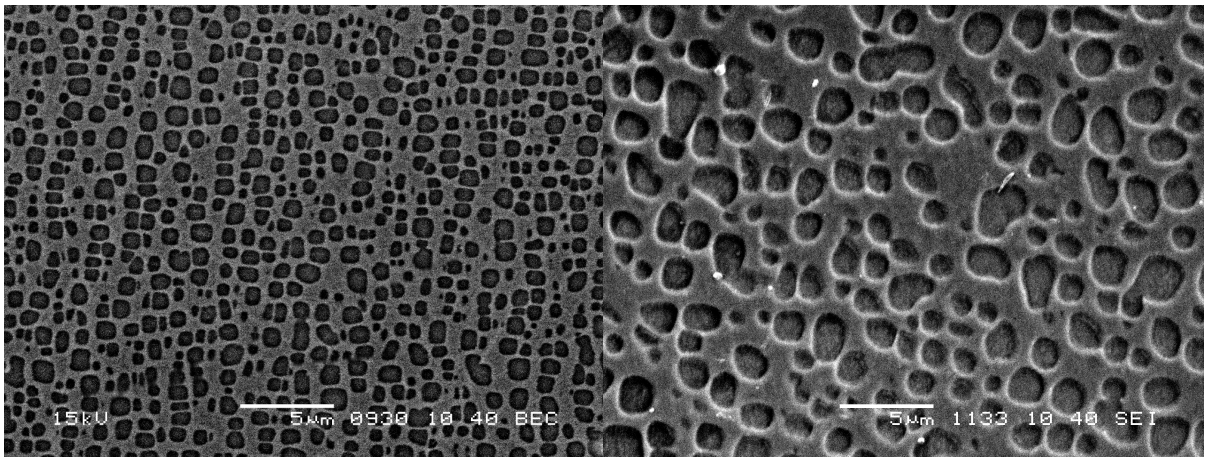

Fig. 2. Left: Microstructure after 500 hours at 950ºC (BSE); Right: Microstructure after 8,000 hours at 950ºC (SEI).

This coarsening can normally be described using an expression for Ostwald ripening where the particle size increase is proportional to the cubic root of time. The coarsening of γ´ has been studied intensively by many authors, examples are Chellman & Ardell [3] and Stevens & Flewitt [4]

Stevens & Flewitt showed that the γ´-particles in the IN738 microstructure grew according to $t^{1/3}$ coarsening kinetics and that the larger cuboids coarsen on the expense of the smaller spheroid particles, while the total volume fraction of γ´ stays at a constant value of 0.45. According to the classical theory by Lifshitz & Slyozov [5] and Wagner [6] the growth equation for a distribution of spherical particles can be described according to:

$$r^3 - r_0^3 = \frac{8}{9}\left(\frac{D\gamma V_m C_e}{RT}\right)t$$

where r is the particle radius and r_0 the initial particle radius. D is the composite coefficient of diffusion for the various elements, γ the free energy of the precipitate/matrix interface, V_m the molar volume of the precipitate, C_e the concentration of γ'-forming elements in equilibrium with a precipitate of infinite radius, R the gas constant and T the temperature.

The measurement of particle radius can be done from images like those shown in Fig. 2. Image processing software is then used to convert the images into binary images by applying a thresholding procedure based on contrast difference between particles and matrix. To obtain sufficient contrast difference it is often necessary to apply an etching procedure that preferentially etches either particles or matrix. It is of utmost importance that this etching procedure etches a specimen uniformly and also that similar results can be obtained for all specimens in a series; in other words that the applied etching procedure has good reproducibility. A study of different etchants for superalloys can be found in [7]. An example of the difficulties associated with finding the correct etching procedure is illustrated in Fig. 3 where the applied etching has had different effects on the three grains visible in the images. It was speculated that the different etching response most likely had to do with different orientations of the grains.

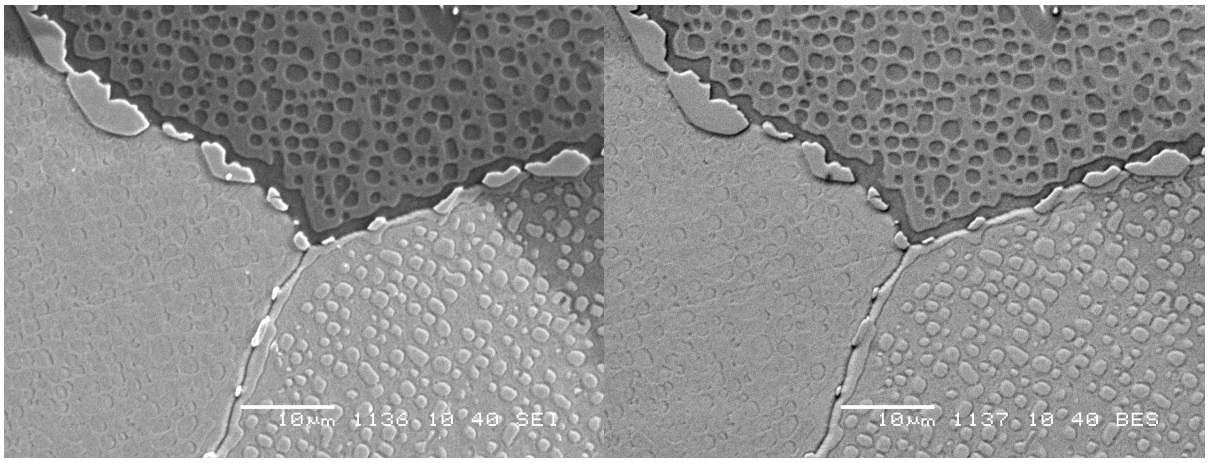

Fig. 3: Etching effects on polycrystalline IN738. The large particles located in grain boundaries are $M_{23}C_6$ carbides; Left: SEI image. Right: BSE shadow image.

When the etching is satisfactory there should be enough contrast difference between matrix and particles to do a threshold. After the thresholding procedure a range of filters are applied

to remove noise while still preserving the correct edge of the particles, for this purpose a procedure described by Højslet [8] was used. Fig. 4 shows the result for an IN738 specimen heat treated isothermally at 950ºC for 500 hours (same as shown in Fig. 2).

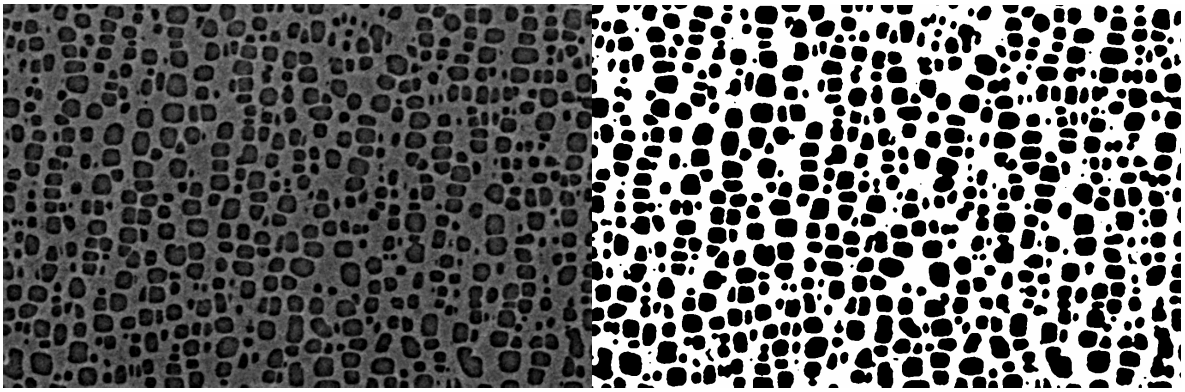

Fig. 4: Left: SEM image; Right: Binarized and filtered end image to be used for estimation of mean γ′-radius. No scale has been included on the images, but the original image is cropped from the image shown in Fig. 2, where a scale can be found.

The obtained image nicely illustrates some of the uncertainties affecting the measurement of γ′-particle size for the IN738 alloy. The bimodal γ′-distribution found in the virgin specimen is still present; hence in order to measure only the larger particles a cut-off size has to be applied so that particles smaller than this size will not be included in the measurement. This cut-off has to be chosen carefully since it will of course affect the end result. There is also the danger that the image-processing steps have made particles lying very close appear like they are one particle. These then have to be manually split into two by the operator in order to get the correct result.

All in all the use of γ′-coarsening for estimation of metal temperature of IN738 seemed to be associated with larger uncertainties than using the measurement of layer growth between the superalloy and the applied coating, and therefore effort was focused on the interdiffusion behaviour.

References

[1] K. V. Dahl and J. Hald, Estimation of Metal Temperature of MCrAlY Coated IN738 Components Based on Interdiffusion Behaviour, included later in this thesis.
[2] J. M. Aurrecoechea, W. D. Brentnall and J. R. Gast: *Journal of Engineering for Gas Turbines and Power*, 1991, **113**, 251-260.
[3] D. J. Chellman and A. J. Ardell: *Acta Metallurgica*, 1974, **22**, 577-588.
[4] R. A. Stevens and P. E. J. Flewitt: *Materials Science and Engineering*, 1979, **37**, 237-247.
[5] I. M. Lifshitz and V. V. Slyozov: *J. Phys. Chem. Solids.*, 1961, **19**, 35.
[6] C. Wagner: *Z. Elektrochem*., 1961, **65**, 581.
[7] T. Boncina, F. Zupanic, A. Krizman, B. Markoli and S. Spaic: *Practical Metallography*, 2004, **8**, 373-385.
[8] L. Højslet and K. Borggreen: Nordtest Technical Report 526; Nordtest project no. 1601-02.

Obtaining average composition profiles across multi-phase layered microstructures

Obtaining composition profiles in the SEM is normally a time consuming task and can also be highly problematic in multiphase alloys. Therefore work was done to find a new way of measuring average composition profiles across such surfaces. For the present project this specifically meant finding a method that allowed for the measurement of average composition profiles across interfaces between superalloys and applied coatings. This is usually a difficult task because of the many precipitate phases present in both bulk superalloy and coatings.

The approach that was applied is described in [1] that is included later in this thesis. The developed approach provided the basis for much of the later work. In the present chapter the approach is shortly described and the equations that were used for the ZAF correction scheme are presented.

As a first approximation interdiffusion between layered structures results in 1D changes in concentration gradients since the major diffusion driving force is perpendicular to the surface and internal interfaces. This is a first order approximation because phase separation e.g. precipitation can occur within each layer and result in diffusion fluxes that are non-perpendicular to interfaces. Thermodynamic and kinetic modeling using software such as DICTRA approximates 1D diffusion fluxes and therefore we need experimental methods compatible with 1D modeling.

The present approach uses 2D x-ray compositional maps obtained using SEM EDS equipment for calculating 1D composition profiles across interfaces between coating and bulk material for gas turbine components. The original x-ray dot maps provided only qualitative information about the distribution of single chemical elements in the form of a dot, if an element was present, and no dot if an element was not present. This qualitative information could not be translated into concentration profiles. Modern SEM EDS systems however provide the option of spectrum imaging where a single pixel contains a total measurement spectrum. The measured spectrum for a single pixel has very poor count statistics making it difficult to make a conversion from intensity to concentration because of the poor signal to noise ratio. However if pixels can be grouped in a sensible way the count statistics and the

signal to noise ratio can be improved immensely by obtaining average spectra from such groups of pixels. This has resulted in advanced auto-phase procedures [2] where each pixel is automatically assigned to a given phase from criteria based on the spectrums of the individual pixel.

The pixel selection criterion is much simpler for making profiles across straight interfaces such as the interface between a coating and substrate. We just have to select all pixels in lines parallel with the interface. Still this criterion is not implemented in commercial SEM software packages.

Since we have easy access to the actual x-ray map pictures that contain intensity information in the form of grey pixel values of single pixels (varying form 0 to 255), it was decided to simply calculate composition profiles based on the grey pixel intensity. This also gives us the possibility of freely rotating the x-ray maps obtained in the SEM in order to align the interfaces precisely.

The x-ray map pictures are converted into spreadsheet data by converting the grey tone of each pixel into a number between 0 and 255, where 0 is black and 255 is white. In this way a large matrix of grey tone values is obtained. By summing up the values in strips of pixels parallel to the interface of interest and calculating the mean, a value for the average intensity can be obtained and plotted as shown in Fig. 1.

Different methods of converting the intensity profiles into composition profiles were investigated. A simple interpolation between the end points in the form of area composition measurements was found to be too simple since the interpolated values at the middle of the picture were not calculated correctly. Instead it was decided to apply a traditional *ZAF* matrix correction scheme to the average pixel intensities.

For simplicity the calculations were done in a *MathCad* spreadsheet even though the computation time is then longer than for a dedicated *ZAF* programme done in *C* or *Fortran*. The correction was performed according to the simplified *ZAF* correction scheme described in Goldstein et al. [3], and is shortly described in the following section.

Before the *ZAF*-correction scheme could be applied it was necessary to perform a background correction of the measured intensities. Instead of doing a mathematical modelling of the background it was decided to apply a simple experimental approach. Background removal was done by measuring the intensity response from elements that were not present in the sample, and subtracting this value from the measured intensities of elements that were present in the sample. Each elemental map in EDS x-ray mapping is collected by using an energy window around the characteristic x-ray line for each element of interest. Since the local intensity of the background varies along the energy scale, having the classic form due to bremsstrahlung, intensity corrections for each elemental analysis line must be made. The level of background intensity is thus approximated by collecting an x-ray map for an element that is not present in the sample but which is close in energy to the element of interest and then applying a smoothening filter to the measured intensity profile. If it was known that some elements were only present on one side of the interface then the measured intensity value for the side where they were not present was used as a zero point. This zero point value was then subtracted from all the measured intensity values for that element as background before proceeding with the calculations.

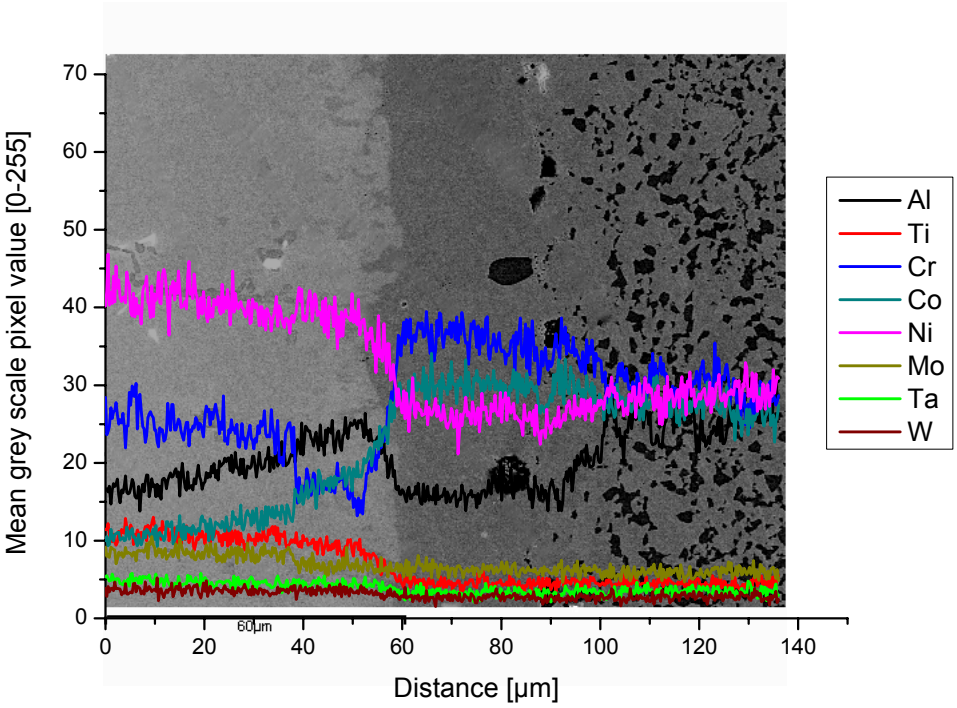

Fig. 1: Intensity profile across the interface of a MCrAlY coated IN738 superalloy.

ZAF correction scheme

The main equation used for the ZAF correction relates the concentration of elements in the unknown sample to that of a known standard according to:

$$\frac{C^*_{x,i}}{I^*_{x,i}} = Z_i A_i F_i \frac{C^{std}_i}{I^{std}_i} \qquad \textbf{eq. 1}$$

where $C^*_{x,i}$ is the concentration at distance *x* of element *i*, $I^*_{x,i}$ is the corresponding measured intensity in a sample (*), C^{std}_i and I^{std}_i are the concentration and intensity of element *i* in a known standard, and Z_i, A_i, F_i are correction factors originating from atomic number correction, absorption correction and fluorescence correction respectively for element *i*.

Atomic number correction

The atomic number correction depends on the two phenomena, electron backscattering R and electron retardation S that both depend upon the average atomic number of the sample to be investigated. Thus if there is a difference between the average atomic number of the sample and that of the used standard a correction is necessary.

The atomic number correction parameter can be expressed as follows:

$$Z_i = \frac{R^{std}_i \int_{E_c}^{E_0} \frac{Q}{S^{std}} dE}{R^*_i \int_{E_c}^{E_0} \frac{Q}{S^*} dE} \qquad \textbf{eq. 2}$$

where R^*_i is the backscattering correction factor for element *i* for the sample (*) and for the standard (std), S is the electron stopping power, Q is the ionization cross section, defined as the probability per unit path length of an electron with a given energy causing ionization of a particular inner electron shell of an atom in the target specimen, E_0 is the beam energy and E_c is the critical excitation energy for the characteristic x-ray line of interest.

The *R* factor represents the fraction of ionization remaining in a target after loss due to backscattering of beam electrons. The backscattering correction factors were calculated according to the fit of Yakowitz et al. [4] of the tabulated values of Duncumb and Reed [5] according to the following expressions with respect to overvoltage $U = E_0 / E_c$ and atomic number *Z*:

$$R_{ij} = R_1^{'} - R_2^{'} \ln(R_3^{'} Z_j + 25) \qquad \textbf{eq. 3}$$

where

$$R_1^{'} = 8.73\times10^{-3}U^3 - 0.1669U^2 + 0.9662U + 0.4523$$

$$R_2^{'} = 2.703\times10^{-3}U^3 - 5.182\times10^{-2}U^2 + 0.302U - 0.1836$$

$$R_3^{'} = (0.887U^3 - 3.44U^2 + 9.33U - 6.43)/U^3$$

The term *i* represents the element *i*, which is being measured and *j* represents each of the elements present in the sample or standard including element *i*. The last equation contained an error in the text by Goldstein et al. where 0.887 was printed as 8.887. The first value however fits with the calculations they do later in the same chapter.

The electron backscattering factor for either standard or sample can now be found according to:

$$R_i = \sum_j C_j R_{ij} \qquad \textbf{eq. 4}$$

The *S* factor is the continuous energy loss defined as:

$$S = -\frac{1}{\rho}\frac{dE}{dx} \qquad \textbf{eq. 5}$$

where ρ is the density which is normally strongly dependent on atomic number and *x* is distance.

The expression suggested by Thomas [6] for the stopping power was used whereby the integration in equation **2** can be avoided by taking the average energy *E* as $0.5(E_0 - E_c)$ leading to:

$$S_{ij} = (const)\frac{Z_j}{A_j(E_0 + E_c)}\ln\left[\frac{538(E_0 + E_c)}{J_j}\right] \qquad \textbf{eq. 6}$$

where *Z* is the atomic number, *A* the atomic weight and *J* is the mean ionization potential that can be calculated according to:

$$J = 9.76Z + 58.8Z^{-0.19}(\text{eV}) \qquad \textbf{eq. 7}$$

The constant in equation **6** need not be evaluated since it cancels out when the stopping power of sample and standard are compared.

To calculate S_i for a given sample or standard a weighted average of S_{ij} can now be used:

$$S_i = \sum_j C_j S_{ij} \qquad \textbf{eq. 8}$$

By assuming that the ionization cross section is constant, the original equation **2** now simplifies to:

$$Z_i = \frac{R_i^{std}}{R_i^*} \frac{S_i^*}{S_i^{std}} \qquad \textbf{eq. 9}$$

Absorption correction A:

The absorption correction was calculated according to the Philibert-Duncomb-Heinrich (PDH) equation described in the following:

$$\frac{1}{f(\chi)} = \left(1 + \frac{\chi}{\sigma}\right)\left(1 + \frac{h}{1+h}\frac{\chi}{\sigma}\right) \qquad \textbf{eq. 10}$$

where

$h = 1.2\frac{A}{Z^2}$, $\chi = \mu/\rho)_i^* \csc\psi$ and $\sigma = \frac{4.5\times10^5}{E_0^{1.65} - E_c^{1.65}}$,

A is the atomic weight and Z the atomic number of the element concerned, $\mu/\rho)_i^*$ is the mass absorption coefficient for radiation from element i in the sample (*) and ψ is the take-off angle.

For multi component samples h and $\mu/\rho)_i^*$ can be calculated according to:

$$h = \sum_j C_j h_j \qquad \textbf{eq. 11}$$

and

$$\mu/\rho)_i^* = \sum_j \mu/\rho)_i^j C_j \qquad \textbf{eq. 12}$$

where j represents the various elements present in the sample including element i, C_j is the weight fraction of each element in the specimen including element i and $\mu/\rho)_i^j$ is the mass absorption coefficient for radiation from element i in element j.

The absorption correction is now given as:

$$A_i = \frac{f(\chi)^{std}}{f(\chi)^*} \qquad \textbf{eq. 13}$$

Characteristic fluorescence correction F:

The fluorescence correction can be calculated from an equation of the following form:

$$F_i = \frac{\left(1+\sum_j \frac{I_{ij}^f}{I_i}\right)^{std}}{\left(1+\sum_j \frac{I_{ij}^f}{I_i}\right)^*} \qquad \textbf{eq. 14}$$

I_{ij}^f / I_i relates the intensity of radiation of element i produced by fluorescence of element j, I_{ij}^f to the electron generated intensity of radiation from element i, I_i.

For element i fluoresced by element j we have:

$$\frac{I_{ij}^f}{I_i} = C_j Y_0 Y_1 Y_2 Y_3 P_{ij} \qquad \textbf{eq. 15}$$

where

$$Y_0 = 0.5\frac{r_i - 1}{r_i}\omega_j \frac{A_i}{A_j}, \qquad Y_1 = \left[\frac{U_j - 1}{U_i - 1}\right]^{1.67}, \quad Y_2 = \frac{\mu/\rho)_j^i}{\mu/\rho)_j^*}, \quad Y_3 = \frac{\ln(1+u)}{u} + \frac{\ln(1+v)}{v}$$

with

$$u = \frac{\mu/\rho)_i^*}{\mu/\rho)_j^*}\csc\psi, \qquad v = \frac{3.3\times10^5}{(E_0^{1.65} - E_c^{1.65})\mu/\rho)_j^*},$$

with E_c evaluated for element i, r_i is the absorption edge jump-ratio for element i. For a K line $(r_i\text{-}1)/r_i$ is 0.88 and for an L line $(r_i\text{-}1)/r_i$ is 0.75. ω_j is the fluorescent yield for element j.

P_{ij} is a factor for the type of fluorescence occurring. If KK or LL fluorescence occurs, $P_{ij} = 1$. If LK or KL occurs, $P_{ij} = 4.76$ for LK and 0.24 for KL.

Results

Applying this method then allows us to obtain average composition profiles across the interface that was shown in Fig. 1. Calculated concentration profiles are shown in Fig. 2. The composition measurement and the average pixel intensities from the area marked Ref. 1 in the figure was used as standard in the *ZAF* calculations. The composition measurement from the area marked Ref. 2 was then used to check that the *ZAF* corrected values were correct by comparing the end points of the profiles with the results of the area measurement.

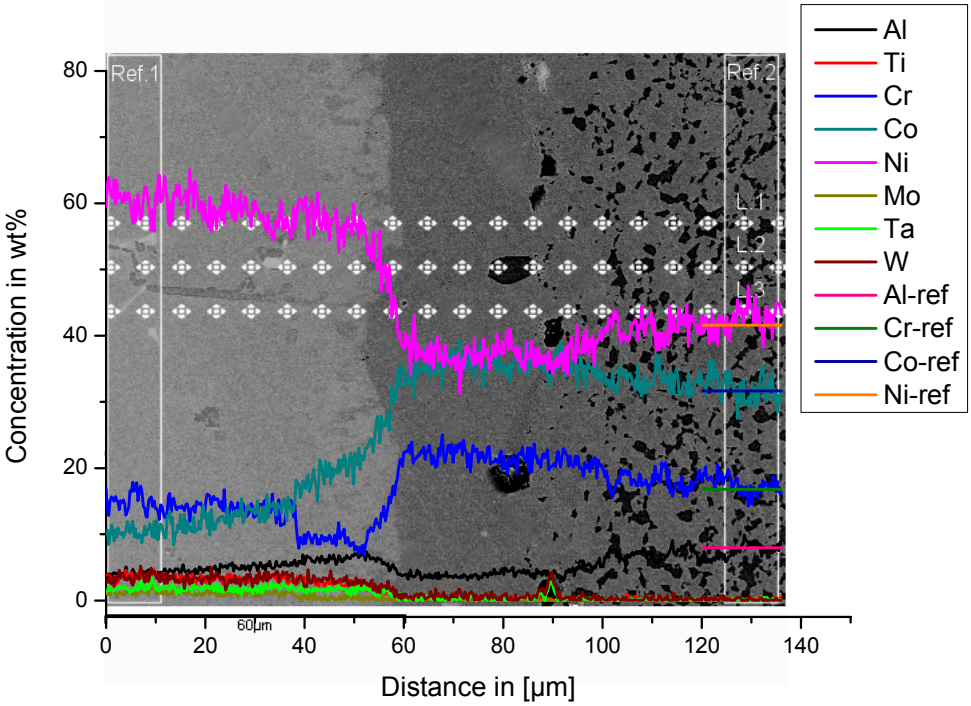

Fig. 2: Average composition profiles calculated from the intensity profiles shown in Fig. 1.

Application of the measurement method

When obtaining composition profiles in the SEM using the present approach it is important to be aware that the SEM settings will have a significant influence on the results obtained. Settings such as acceleration voltage, spot size and dwell time as always play a major role in the obtained results. Especially one should be cautious if peak overlaps are present among the

elements found. There is also a significant influence of data-collection time; longer collection times will improve the results as long as pixel over saturation is not allowed to occur.

The actual orientation of the specimen in the SEM chamber did not play a significant role, and therefore the specimen was oriented in such a way that the largest possible amount of data points can be extracted. In practice this meant that the interface was oriented either vertically or horizontally on the image screen when the x-ray maps were obtained.

References

[1] K.V. Dahl, J. Hald and A. Horsewell: Material submitted to *Journal of Microscopy*.
[2] J.J. Friel: Advanced Materials & Processes, 2004, **162** (12), 21-23.
[3] J.J. Goldstein, D.E. Newbury, P. Echlin, D.C. Joy, C. Fiori and E. Lifshin: Scanning Electron Microscopy and X-Ray Microanalysis. Plenum Press, New York.
[4] Listed as reference Yakowitz et al. (1973) in [3]; Yakowitz, H.; Myklebust, R. L.; Heinrich, K. H. J. (1973). National Bureau of Standards Tech. Note 796. 1973.
[5] Listed as reference Duncomb and Reed (1968) in [3]; P. Duncomb and S. J. B. Reed: in Quantitative electron microprobe analysis, National Bureau of Standards special publication 298, p. 133.
[6] Listed as reference Thomas (1964) in [3]; P. M. Thomas: U.K. Atomic Energy Auth Rept. AERE-R 4593.

Summary of papers concerning interdiffusion between IN738 and MCrAlY coating

Three different papers were written on the interdiffusion between IN738 and MCrAlY coating. The first paper I) *Grey-scale conversion x-ray mapping by EDS of multi-element and multi-phase layered microstructures*, describes a general approach for measuring average composition profiles in the scanning electron microscope. The following two papers make use of the approach developed in this paper; first for the estimation of metal temperature of service exposed components II) *Estimation of Metal Temperature of MCrAlY Coated IN738 Components Based on Interdiffusion Behaviour* and secondly for comparison with modelled results of thermodynamic and kinetic modelling using Thermo-Calc and DICTRA III) *Modelling of Interdiffusion between MCrAlY coating and IN738 superalloy*.

I) Grey-scale conversion x-ray mapping by EDS of multi-element and multi-phase layered microstructures

The paper describes the approach developed and used in the two following papers for measurement of average composition profiles in the SEM.

The measurement of composition profiles using the traditional point by point measurement method is made difficult by the many precipitate phases present at the IN738/ MCrAlY interface. Therefore a new approach was developed that allow for easy measurement of average profiles.

The method involves a) the collection of grey-scale elemental maps, b) the calculation of corrected mean pixel grey-scale values along strips of pixels parallel with the layered microstructure, and c) the conversion of the resulting grey-scale line profiles to composition line profiles perpendicular to the layered geometry.

The profiles can be obtained using a minimum of SEM time, especially compared to the normal point by point measurement method that has traditionally been used for this kind of system. For microstructural systems that contain a large amount of precipitates, using the information stored in the digital x-ray maps for measuring 1D line profiles across interfaces is far superior to measuring line profiles using point by point measurements.

This way of measuring composition profiles will be an important tool in obtaining a better knowledge about the interdiffusion behaviour between coatings and substrate alloys for gas turbine components.

II) *Estimation of Metal Temperature of MCrAlY Coated IN738 Components Based on Interdiffusion Behaviour*

The developed measurement approach was then used to quantify the interdiffusion taking place at the interface between the Co-36.5Ni-17.5Cr-8Al-0.5Y, MCrAlY coating and the underlying IN738 superalloy in a large matrix of specimens isothermally heat treated for up to 12,000 hours at temperatures 875°C, 925°C or 950°C. Microstructural investigations and calculated phase fraction diagrams using Thermo-Calc showed that a precipitate free zone formed between the coating and superalloy and grew with time.

The width of the precipitate free zone can be related to the aluminium and chromium profiles across the interface. It was chosen to use the measured Al x-ray maps and the resulting average Al intensity profiles as basis for measurement of the growth of the interdiffusion zone with time. A simple parabolic growth model was then set up for estimating the metal temperature near the coating/ substrate interface based on the growth kinetics of the precipitate free zone. Parameters for the model were extracted from measurements of the width of the growing precipitate free zone with time.

The use of the model was then illustrated on a service exposed, first stage gas turbine blade from a Danish gas turbine.

The developed model can be used with good accuracy in the temperature range where the coating is degraded and the estimated metal temperature can be used as input for models of coating life time.

III) *Modelling of Interdiffusion between MCrAlY coating and IN738 superalloy*

The average profiles measured using the method described in I) can be directly compared to the average profiles calculated in kinetic multi-element modelling software such as DICTRA.

The modelling was able to qualitatively describe phase transformations occurring at the interface as a result of the interdiffusion between coating and superalloy.

The simulated results predicted that the interdiffusion would result in the formation of a precipitate free zone, a γ′-rich layer next to the superalloy and precipitation of secondary carbides on the superalloy side of the interdiffusion zone. These features were confirmed by microstructural investigations of isothermally exposed specimens.

The width of the precipitate free zone formed between the coating and the superalloy were of the same size in the experiments and the simulations. A more sophisticated model able to take into account diffusion in the precipitate phases would however be needed to precisely describe the interdiffusion.

After long time exposure the coating can no longer be considered as semi-infinite. In the actual microstructure this means that the aluminium loss due to oxidation at the surface will also have influence on the interdiffusion. A complete model of the interdiffusion behaviour should therefore also take the oxidation mechanism into account.

Outlook

The developed measurement method provides excellent experimental data that can be used for validation of modelled results for the complex interdiffusion between superalloys and coatings.

One of the overall goals with the DICTRA modelling was to be able to extract parameters from the simulated results describing the growth of the precipitate free zone between superalloy and components. In this way simple models like that described in paper II) could be set up based on simulated results instead of rigorous and time-consuming investigations on isothermally heat treated laboratory specimens. It would then also be possible to use simulations to test whether a model set up from laboratory specimens would apply to a coating/ superalloy system with slightly modified compositions, as is often encountered in practical life.

The multi-element modelling done in DICTRA during the present project was able to qualitatively describe the phase transformations that were also found in the microstructural investigations. It was however found that the limitation that only one matrix phase can be handled in the calculations was very severe for the investigated Co-36.5Ni-17.5Cr-8Al-0.5Y/ IN738 system. The precise treatment of the diffusion for the present system would therefore demand a model able to handle multiple matrix phases and perhaps also diffusion parameters for disperse phases.

Appendix I

Grey-scale conversion x-ray mapping by EDS of multi-element and multi-phase layered microstructures

- Submitted to Journal of Microscopy 19/12/2005

Grey-scale conversion x-ray mapping by EDS of multi-element and multi-phase layered microstructures

K. V. Dahl, J. Hald & A. Horsewell

Materials Technology, Dept of Manufacturing Engineering and Management, Technical University of Denmark, DTU, Lyngby, Denmark

Corresponding author: K. V. Dahl, kvd@ipl.dtu.dk

Key words: EDS, x-ray mapping, line profiles, compositional imaging, spectrum imaging, grey-scale conversion, layered microstructures

Summary

A procedure for *grey-scale conversion* of EDS x-ray maps has been developed which is particularly useful for the plotting of line composition profiles across modified layered engineering surfaces. The method involves a) the collection of grey-scale elemental maps, b) the calculation of mean grey-scale levels along strips parallel to the layered microstructure and c) the conversion of grey-scale line profiles into composition line profiles. As an example of the grey-scale conversion method and its advantages for multi-element and multi-phase layered microstructures, the procedure has been applied to a layered microstructure that results from a plasma-sprayed metallic MCrAlY-coating onto a nickel-superalloy turbine blade. As a further demonstration of the accuracy and amount of compositional data that can be obtained with this procedure, measured compositional profiles have been obtained for several long-term isothermal heat treatments in which significant interdiffusion has taken place. The resulting composition profiles have greatly improved counting statistics compared to traditional point-by-point scans for the same SEM time and may be considered as a rapid alternative to EDS spectrum imaging. The composition profiles obtained may be conveniently compared with results of multi-component thermodynamic modelling of interdiffusion.

Introduction

The speed and accuracy of compositional analysis using energy dispersive spectroscopy (EDS) in the scanning electron microscope (SEM) has improved markedly over the last 10 years. Improvements in signal collection, signal processing and in particular, speed of

spectrum analysis has resulted in increased signal to noise ratios and consequently better analyses. Even so, the determination of composition profiles across compositionally modified engineering surfaces is still a very demanding process.

As an example, EDS analysis of compositional changes in multi-layered surface coatings that are applied to gas turbine blades is still rather complicated and time-consuming. A typical gas turbine blade may have an outer thermal barrier coating consisting of yttria stabilized zirconia followed by a metallic MCrAlY overlay coating or an Al-Pt diffusion coating for oxidation protection. This coating is diffusion bonded to a compositionally complex superalloy substrate material. The compositions of each of these layers and of the substrate have microstructures that have been developed over several decades and are specifically engineered to provide high temperature resistance and mechanical strength. The EDS analysis therefore often involves the analysis of more than 10 chemical elements across distinctly different layers. Further, many of the classic EDS analysis difficulties are present: Large differences in atomic number of the constituent elements, requiring detailed consideration of both excitation optimization and interaction volume; heavy elements in relatively light matrix volumes, and the inverse; inhomogeneities due to discrete precipitates and/or pores.

Both during processing and during high temperature service, significant interdiffusion will take place between the layered structures of a gas turbine blade and it is therefore important to be able to measure and accurately plot compositional profiles across the multilayered structure. Since there is also a need to compare the measured compositional profiles with results from diffusion modelling, the concentrations of all elements at all equivalent positions in all of the layers are of interest. This is because the diffusion behaviour of individual elements at any given position in the layers is dependent on the concentrations of all other elements as well as the concentration gradients at that position.

As a first approximation, interdiffusion between layered structures results in one-dimensional (1-D) changes in concentration gradients, since the major diffusion driving forces are perpendicular to the surface and internal interfaces. This is a first order approximation because phase separation e.g. precipitation can occur within each layer and result in diffusion fluxes that are non-perpendicular to interfaces. Diffusion modelling software such as DICTRA (Borgenstam et al. (2000)) approximates 1-D diffusion fluxes and therefore we need experimental methods that yield results compatible with 1-D modelling. From prepared

metallographic cross-sections there are the following traditional experimental procedures in the SEM that can be chosen.

a) EDS point measurements
b) EDS multiple point measurements
c) EDS line scans
d) EDS x-ray dot-maps

Each of these methods has both advantages and drawbacks. The traditional solution (a) is to simply make a number of *EDS point measurements* on a straight line from bulk material and out to the surface. The spatial resolution can, up to a limit determined by the interaction volume, then be improved by increasing the number of measurement points along the line. However, if the microstructure contains precipitates with another chemical composition than the matrix, sharp composition changes will occur where a measurement point coincides with a precipitate.

This effect can be suppressed by making *multiple rows of point measurements,* method b, whereby an average value is obtained. This can however be very time consuming and can require a considerable number of series of rows of multiple point measurements before a satisfactory result can be obtained.

Using a *line scan*, method c, the electron spot is scanned across a specimen and the intensity for a selected energy window (EDS) for each element is recorded. This method is quite fast but since the electron beam, compared to methods a) and b), spends less time in each point the accuracy is not as good as for point measurements and the count statistics are poorer. For this method it is also necessary to make repeated scans along several lines displaced relative to each other in order to obtain an average concentration profile which is not disturbed by microstructural inhomogeneities.

X-ray dot-mapping (d) is an old technique that was developed by Cosslett & Duncumb (1956). It has been a much-used technique ever since because of the ease with which the x-ray dot-maps can be interpreted and because of the valuable qualitative information on the distribution of chosen elements that they provide. The original analogue x-ray dot maps did not store any kind of quantitative information. A pixel in such a map would have one of two values; 0 or black if the element was not detected and 1 or white if an element was detected. With the development of *digital elemental mapping* or *grey-scale mapping* it became possible

to vary the brightness of each pixel in the x-ray dot-maps in relation to the measured intensity. A grey tone level between 0 and 255 is assigned to each pixel and can be directly related to the intensity measured for a given element.

Direct digital *compositional imaging* was developed by Newbury and co-workers in the late 80s and 90s (Newbury et al. (1990)). This technique uses either WDS (wavelength dispersive spectroscopy), EDS or a combination of both techniques to obtain compositional maps that provide quantitative information on the distribution of elements in a map. Using this methodology the electron beam is allowed to dwell for a chosen (short) time in each pixel; a spectrum is obtained and then corrections for background and matrix effects similar to the corrections made in a traditional point measurement are then performed for each pixel. This technique is however quite time consuming and the count statistics in each pixel are poor unless the electron beam is allowed to dwell for a long time in each pixel increasing the total time used to obtain such a map.

In recent years X-Ray *spectrum imaging* or *hyper spectral imaging* has become a practical mode for data collection as described by Mott & Friel (1999) and Friel (2004). Using this technique an entire X-ray spectrum is saved for each pixel position and is available for post-acquisition data analysis. Software tools to analyze these spectrum images are now commonly available with commercial EDS software systems. Typical features are maps for any elements, spectra from specific regions and automatic sorting into phases. The possibilities for pixel grouping and selection are really only limited by the possibilities of the software.

As previously noted, microstructural inhomogeneities have a significant influence on the x-ray mapping or line profiling strategy to be adopted. In multi-layered coatings such as those used to impart high temperature oxidation resistance to turbine blades, interdiffusion fluxes are acceptably approximated to be perpendicular to the layers of interest. This is the case even though some layers consist of a 3-D array of precipitates. Therefore, for the study of diffusion across planar interfaces it would be reasonable to group pixels in strips taken along an axis perpendicular to the interface(s) of interest. The result is a profile in which each point is derived from summing the spectra for all pixels that are the same distance from the interface.

Rather than extracting spectral imaging data in order to form an elemental map, the approach adopted in the current study has been to analyse the grey-level information stored directly in

the obtained digital x-ray elemental maps. The grey-scale data can be used as an expression for intensity. Specifically, g*rey-scale conversion x-ray mapping* can then be achieved using the procedure outlined below.

For cross-sectional metallographic specimens obtained from layered geometries, variations in grey level intensities can be obtained from large numbers of pixels in strips taken along an axis perpendicular to the layered interfaces. A mean grey-scale pixel value is obtained for each strip, for each element and used as an expression for intensities and finally converted to compositions using a standard procedure for quantitative elemental analysis. As a consequence, only variations in composition that are related to the layered geometry, such as interdiffusion or near-interface denuded zones, are measured. This provides elemental concentrations that may be directly compared to profiles determined by thermodynamic diffusion modelling software such as DICTRA.

The method therefore involves a) the collection of grey-scale elemental maps, b) the calculation of corrected mean pixel grey-scale values along strips of pixels parallel with the layered microstructure, and c) the conversion of the resulting grey-scale line profiles to composition line profiles perpendicular to the layered geometry.

Experimental procedures

The specimens chosen for composition profile analysis to demonstrate the efficacy of this technique are Ni-superalloy gas turbine blades which have been surface engineered to resist oxidation at high temperature. The substrate is an IN738 superalloy and the coating is a metallic MCrAlY overlay coating that is applied by low pressure plasma spraying. Compositions of powders used for coating and superalloy are shown in tables 1 and 2.

Table 1: Average composition of MCrAlY coating in wt%.

Co	Ni	Cr	Al	Y
balance	32	17.5	8	0.5

Table 2: Average composition of IN738 superalloy in wt%.

C	Al	Ti	Cr	Co	Ni	Nb	Mo	Ta	W
0.01	3.2	3.2	16.0	8.5	balance	0.9	1.8	1.8	2.6

After the MCrAlY coating had been applied to the substrate using plasma spraying the specimens received a standard two step heat treatment:

1) 1120ºC for 2 hours, then air cooled.
2) 845 ºC for 24 hours, then air cooled.

In the following, specimens that have received this initial heat treatment are referred to as being in the as-coated condition. Specimens were then further isothermally heat treated in air at 875ºC, 925ºC and 950ºC for up to 4000 hours in order to simulate in-service conditions during gas turbine operation.

Standard metallographic procedures were used to cut, mount and polish the specimens in cross-section. Specimens were ground and then diamond polished to 1 μm finish. The metallographically prepared specimens were then coated with approximately 50 nm evaporated carbon.

SEM observations and x-ray spectroscopy were carried out in a JEOL 5900 SEM operated under high vacuum conditions. The EDS system used was INCA 400 from Oxford Instruments using a Si detector crystal with 133 eV resolution measured at 5.9 keV.

Results and procedures

BSE-images were obtained as shown in figure 1 and 2. Atomic number contrast immediately indicates large layer to layer differences in average atomic number and density. At the top of the micrograph, corresponding to the exposed surface of the coating, an outer depletion zone can be seen which is depleted of the β-NiAl phase that acts as a reservoir phase for aluminium. The depletion has occurred because of the diffusion of aluminium to the surface in order to maintain an Al_2O_3 protective oxide layer. Underneath this depleted zone is the bulk coating consisting of a Co, Ni, Cr rich fcc matrix with a large volume fraction of β-NiAl precipitates (black particles). The size and shape of the β-particles changes with time due to coarsening and the β-NiAl phase is depleted both because of diffusion of aluminium out towards the surface and because of diffusion into the underlying substrate alloy that has a lower aluminium content than the coating. Between the coating and the substrate an interdiffusion zone is formed.

In the lower part of figure 1 the substrate Ni-superalloy is seen. The microstructure consists of a γ-matrix with coherent $Ni_3(Al, Ti)$ γ'-particles homogeneously distributed throughout the

microstructure. The volume fraction of γ'-particles in the bulk alloy is close to 0.4. The γ'-particles are extremely stable and the Ni-base superalloys obtain their excellent high temperature creep properties because of the presence of this phase. The large bright particles visible in the image are primary (Ti, Ta)C carbides that are formed during the initial heat treatment. Secondary $(Cr, Mo)_{23}C_6$ carbides that are formed during the second stage of the initial heat treatment are found precipitated along grain boundaries. With time, the primary carbides are dissolved whereby carbon is released and more secondary carbides are precipitated.

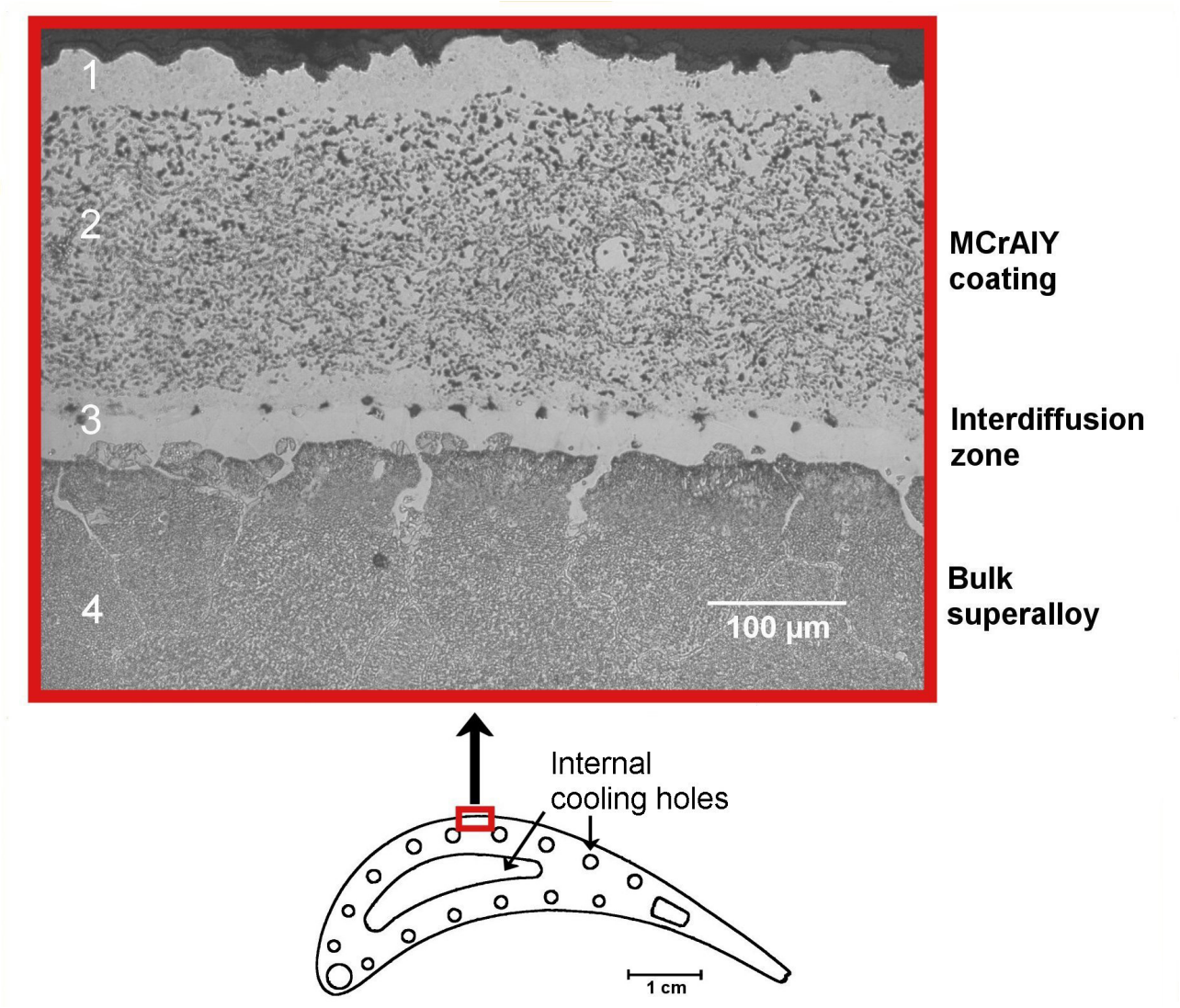

Figure 1: Light optical image of a cross-section of MCrAlY-coating on the Ni-superalloy substrate. The layered microstructure has undergone considerable changes due to interdiffusion after exposure at 950°C for 4000 hours. The following layers can be identified: 1) Outer depletion zone with loss of *β*-NiAl; 2) bulk MCrAlY coating with a large volume fraction of *β*-NiAl (black particles); 3) Interdiffusion zone between coating and substrate, at the interface are dark particles, pores, impurities and inclusions resulting from the coating procedure; 4) Substrate of Ni-superalloy showing *γ*/*γ*′ microstructure. The schematic at the bottom of the image shows the cross section of a turbine blade; the MCrAlY coating is applied to the outer surface of the blade to provide protection against oxidation.

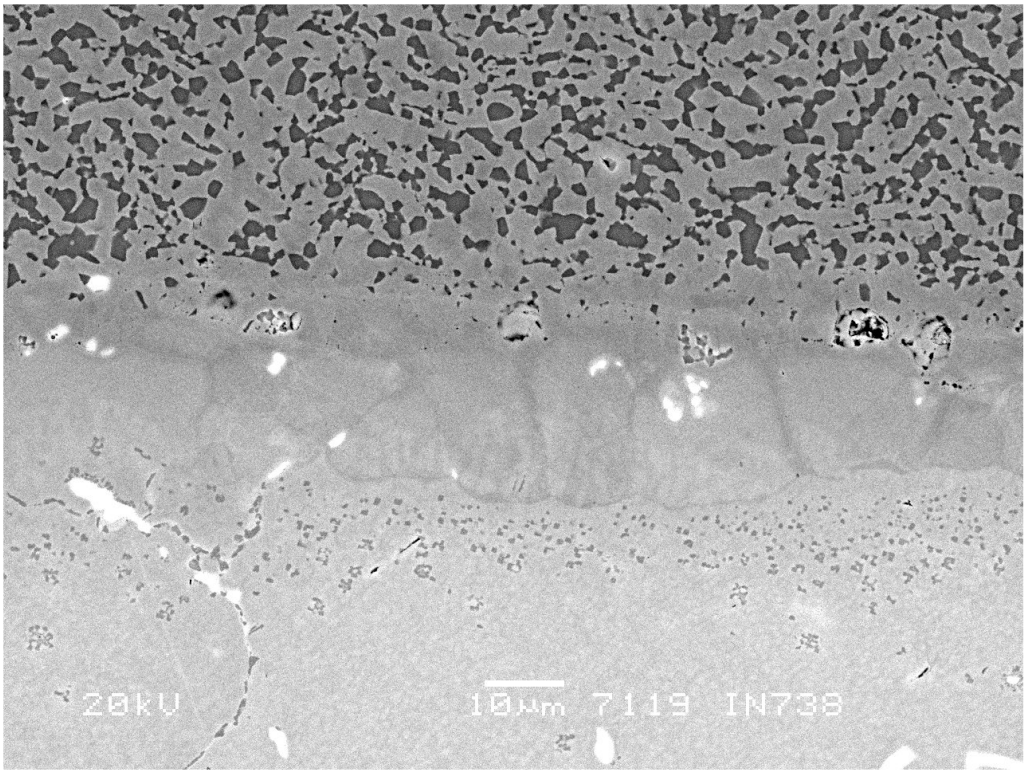

Figure 2: SEM image taken using contrast from backscattered electrons (BSE) of another cross-section showing a closer look at the interface for a specimen heat treated for 250 hours at 925ºC. The same zones observed in figure 1 are visible. It is immediately apparent from the many precipitates that making line profiles using point measurements is difficult for this system. In this micrograph, precipitation of discrete $M_{23}C_6$ particles at the interface is also clearly visible.

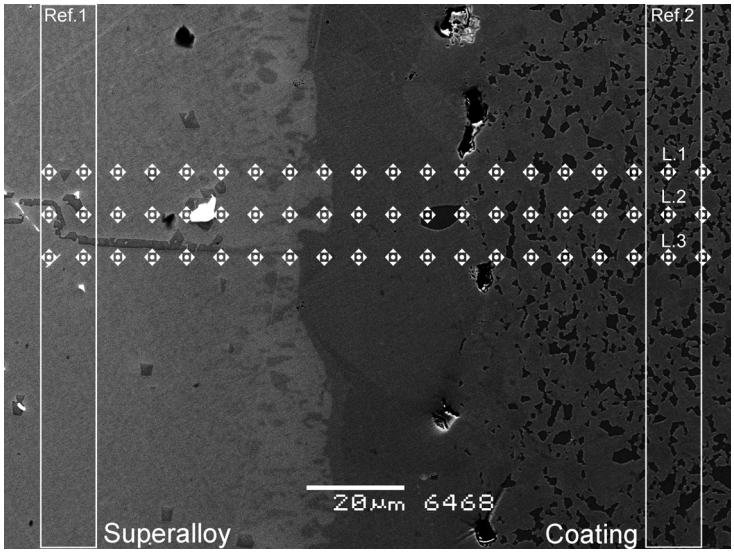

Figure 3: BSE image of the interdiffusion zone of the specimen isothermally heat treated at 950ºC for 4000 hours (image is rotated 90º, compared to figure 2). Reference measurements along area strips, marked Ref.1 and Ref.2 and point measurements along lines L.1 and L.2 and L.3 are marked in the image. The reference measurements were obtained using standard operating conditions as follows: Acceleration voltage of 15 keV; deadtime of ~20%.; count time of 1½ minutes per measurement.

Reference EDS measurements

Reference EDS measurements were obtained in rectangular areas in both bulk superalloy and bulk coating as indicated on figure 3 and are given in table 3. The reference measurements were placed in such a distance from the interface that it could be assumed that the measured compositions were unaffected by the interdiffusion.

Table 3: Reference EDS measurements.

Spectrum	Al	Ti	Cr	Co	Ni	Mo	Ta	W	Total
Ref. 1	4.0	3.6	15.1	10.3	60.4	1.2	1.9	3.5	100.0
Ref. 2	8.0	0.5	16.8	31.7	41.6	0.3	0.3	0.8	100.0

Elemental x-ray mapping

Next, elemental grey-scale maps were acquired for all elements identified from the reference EDS measurements for the complete area shown in figure 3.

Operating conditions for mapping were chosen to ensure that pixel over-saturation did not occur. This was done by observing the development of the maps as they built up in intensity and then stopping the acquisition after the first complete frame in which a small number of the pixels visibly reach the maximum grey-scale value of 255 for one of the elements. The acceleration voltage used for the current specimens was 15 kV. The maps obtained had a pixel resolution of 512x416 pixels.

Elemental maps for Al, Ti, Cr, Co, Ni, Mo, Ta and W were obtained. Examples of the obtained grey-scale maps for major elements are shown in figure 4.

Calculation of mean grey-scale values

Mean grey-scale pixel values were then calculated for strips of pixels oriented parallel to the interface for each elemental map. The element maps each contain 512 pixels along the horizontal side and 416 pixels along the vertical side. This effectively gives us 512 mean grey scale pixel values across the images, each calculated from 416 pixel values. Using the distance from the left edge of the images as independent variable in pixels and converting it to μm, mean intensity profiles like that shown in figure 5 can be plotted.

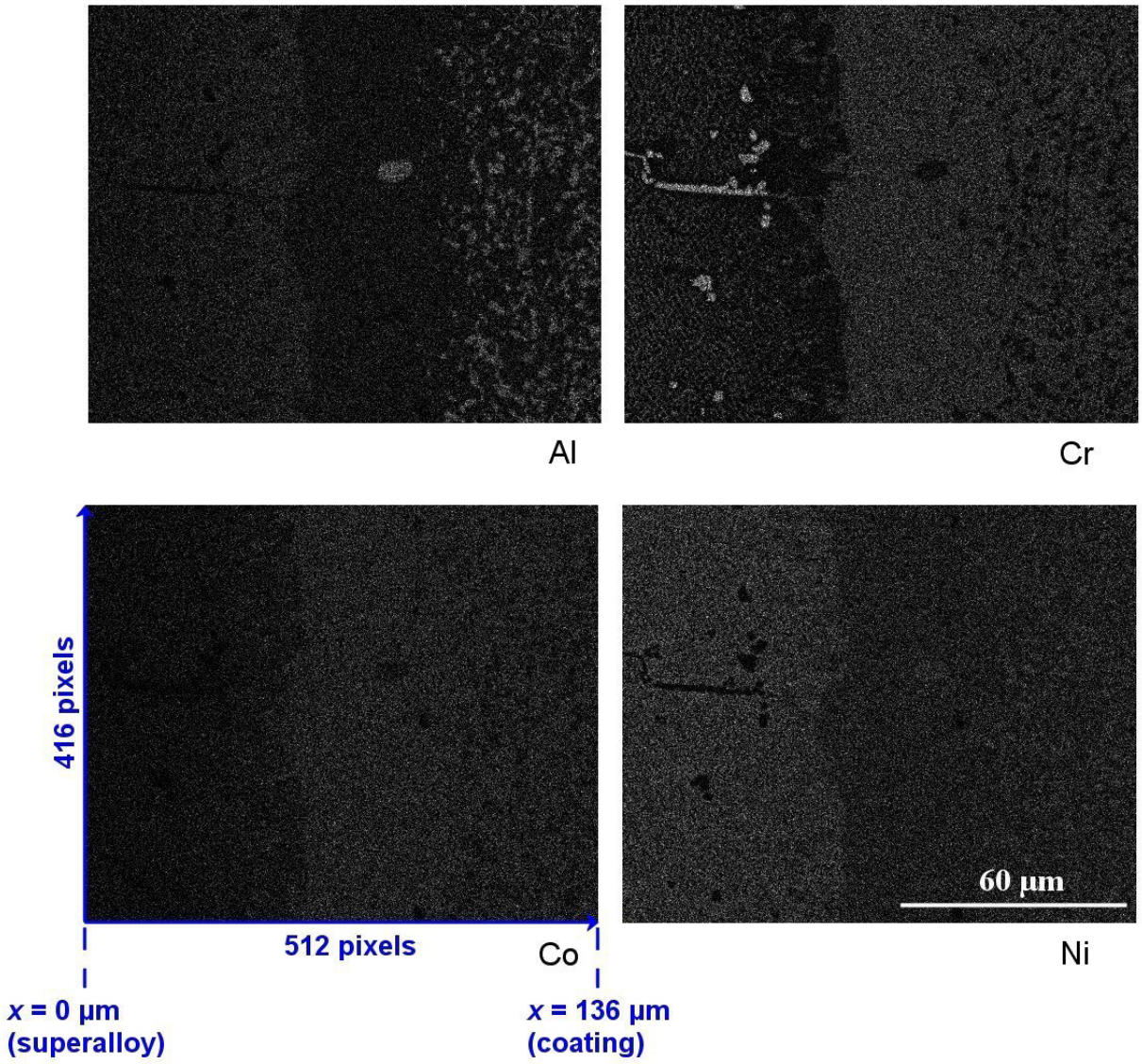

Figure 4: X-ray maps of major elements for the area shown in figure 3. The coating is located to the right in the images and bulk superalloy to the left. The aluminium rich *β*-NiAl particles are clearly seen in the coating in the Al-map, while the Cr-map shows Cr-rich $M_{23}C_6$ carbides in the substrate.

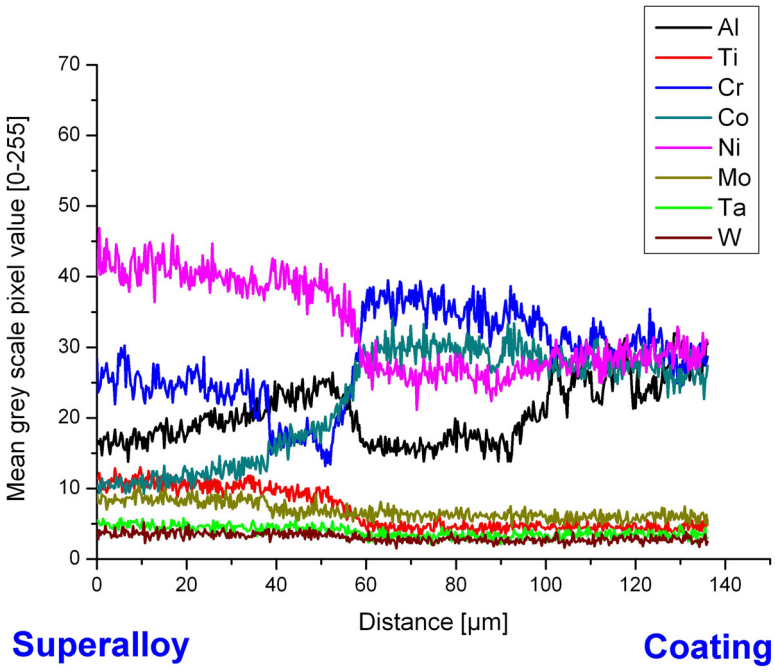

Figure 5: Mean grey-scale intensity profiles for the specimen heat treated for 4000 hours at 950°C. The profiles are obtained by calculating the mean grey-scale pixel value for pixels in strips oriented parallel to the interface.

Conversion of grey-scale intensities to elemental compositions

The measured mean intensities were then converted to compositions. This was done by applying a simple ZAF-correction scheme that corrects the measured intensities for atomic number effects, Z, absorption, A, and fluorescence, F, according to the following equation:

$$\frac{C^*_{x,i}}{I^*_{x,i}} = Z_i A_i F_i \frac{C^{std}_i}{I^{std}_i}$$

where $C^*_{x,i}$ is the concentration at distance x of element i, $I^*_{x,i}$ is the corresponding measured intensity in a sample (*), C^{std}_i and I^{std}_i are the concentration and intensity of element i in a known standard, and Z_i, A_i, F_i are correction factors originating from atomic number correction, absorption correction and fluorescence correction respectively for element i.

The equations describing Z, A and F were adopted from Goldstein et al. (1992).

A reference area measurement in the bulk material such as Ref.1 shown in figure 3 and listed in table 3 was used as the known standard in the calculations. The intensities of the standard

were taken as the mean grey-scale pixel value for the same area and calculated from the obtained elemental maps.

Background correction

Since grey-scale intensity maps contain a contribution from background intensity, background removal was done by measuring the intensity response from elements that were not present in the sample, and subtracting this value from the measured intensities of elements that were present in the sample. Then the ZAF correction was applied to each elemental map. This 'old-school' approach is what used to be done before software routines achieved automatic background correction.

Each elemental map in EDS x-ray mapping is collected by using an energy window around the characteristic x-ray line for the element of interest. Since the local intensity of the background varies along the x-ray energy scale, having the classic form due to bremsstrahlung, an intensity correction for each elemental analysis line must be made. In order to achieve this, the level of background intensity is approximated by collecting an x-ray map for an element that is not present in the sample but which is close in energy to the element of interest. If it was known that some elements were only present on one side of the interface then the measured intensity value for the side where they were not present was used as a zero point. This zero point value was then subtracted from all the measured intensity values for that element as background before proceeding with the calculations.

For the present example AgLα was used to remove background from the measured AlKα line, FeKα was used to correct the measured intensities for Co, Cr and Ni, and since it was known that the coating did not contain Mo, Ta, W and Ti the intensity measurements far to the right, in the coating, of these elements were used as background values.

The resulting normalised composition profiles for an as-coated specimen and the specimen heat treated for 4000 hours at 950ºC are shown in figure 6 and figure 7. A reference measurement like Ref. 2 (figure 3) in the coating was used to test the accuracy of the composition profiles. That the profiles end up at the same compositions as measured from the reference measurement, indicates that the ZAF correction scheme was correctly applied.

Comparison with conventional measurement methods

For comparison results obtained by conventional point by point measurements for the locations L.1, L.2 and L.3 in figure 3 are included and shown in figure 8. It is immediately apparent that the result obtained in figure 7 yields much more information than the result in figure 8, even though the SEM time used is longer for the point by point measurements. The x-ray maps used for the grey-scale conversion were obtained in approximately 40 minutes, while the L.1, L.2 and L.3 took more than 30 minutes each, with 1½ minutes for each point measurement.

A method more appropriate for direct comparison is to collect EDS area measurements while the electron beam is being scanned backwards and forwards along strips parallel to the interface – the same technique that was used for collecting the reference spectra, Ref. 1 and Ref. 2 in figure 3, but now for narrower strips as shown in the small image in figure 9. The result of this method is compared to that of grey scale conversion in figure 9. In this case 47 area measurements were done across the image, corresponding to a total SEM time of 70 minutes with 1½ minutes for each measurement. The result of the two measurement methods are very similar, but the reference method has a somewhat poorer resolution indicating that more and smaller strips should be used in order to catch the sharp interfaces and obtain the same result as for the grey scale conversion method. Especially for Cr it would be necessary to use more and smaller strips in order to obtain the same information as obtained by the grey scale conversion method.

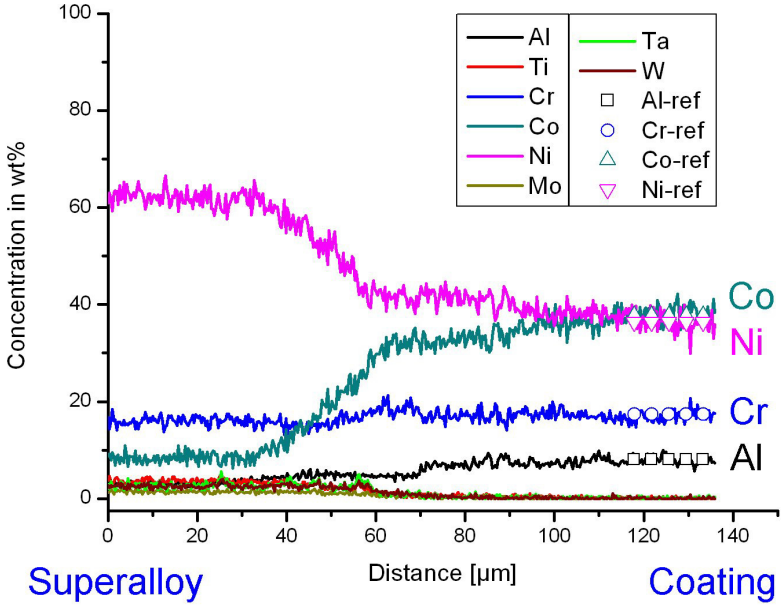

Figure 6: Average composition profiles for as-coated specimen. The profiles are calculated from the mean intensity profiles by applying a simple background correction and ZAF correction to each mean grey-scale pixel value.

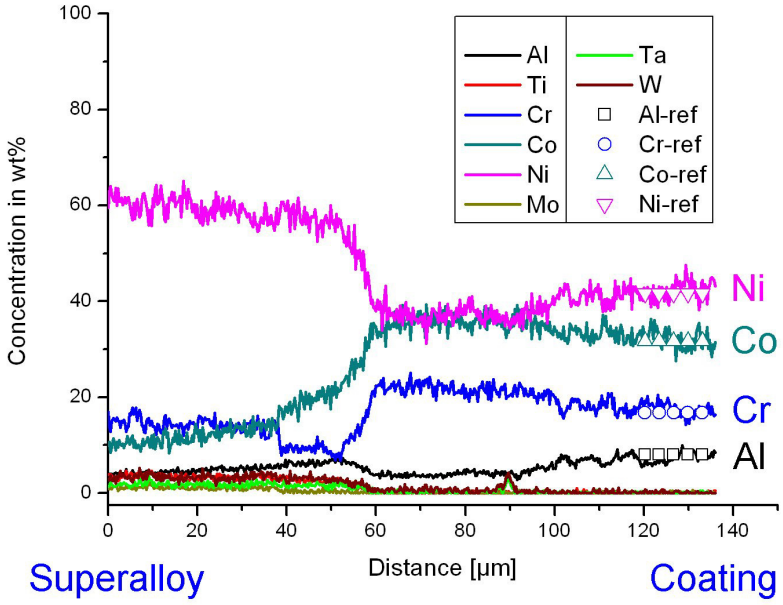

Figure 7: Composition profiles for specimen heat treated for 4000 hours at 950ºC. When comparing to the profiles for the as-coated specimen shown in figure 6, a significant change has occurred due to interdiffusion and the thickness of the interdiffusion zone between superalloy and coating can be evaluated on the basis of the profiles.

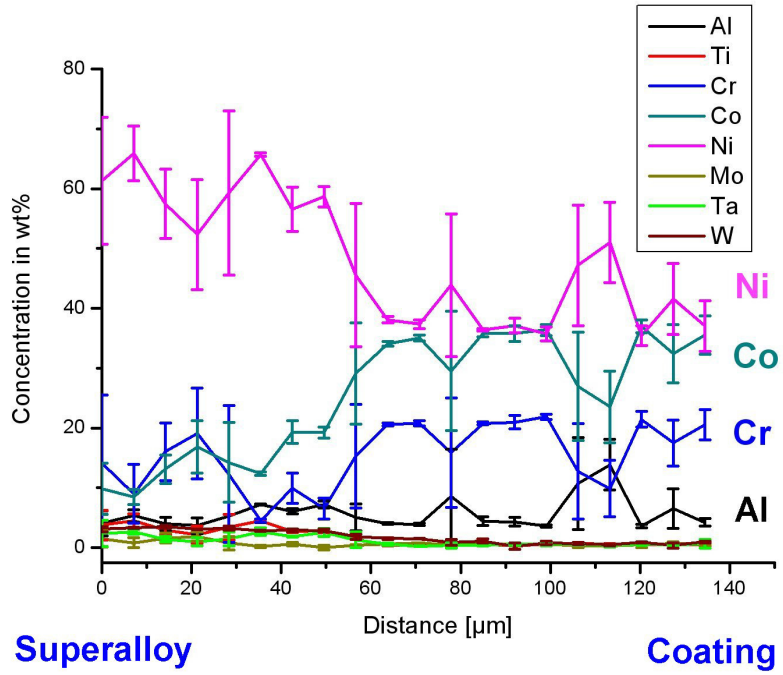

Figure 8: Conventional multiple point measurement for the specimen heat treated at 950°C for 4000 hours (same area as for figure 6); each point is an average of 3 measurement points from the L.1, L.2 and L.3 measurements shown in figure 5. The large standard deviations are a result of the many precipitates present in the different layers. In the centre, the standard deviations are fairly small because the interdiffusion zone is almost free of precipitates while the coating to the left contains a large volume fraction of *β*-particles and the superalloy to the right contains both carbides and γ´-particles.

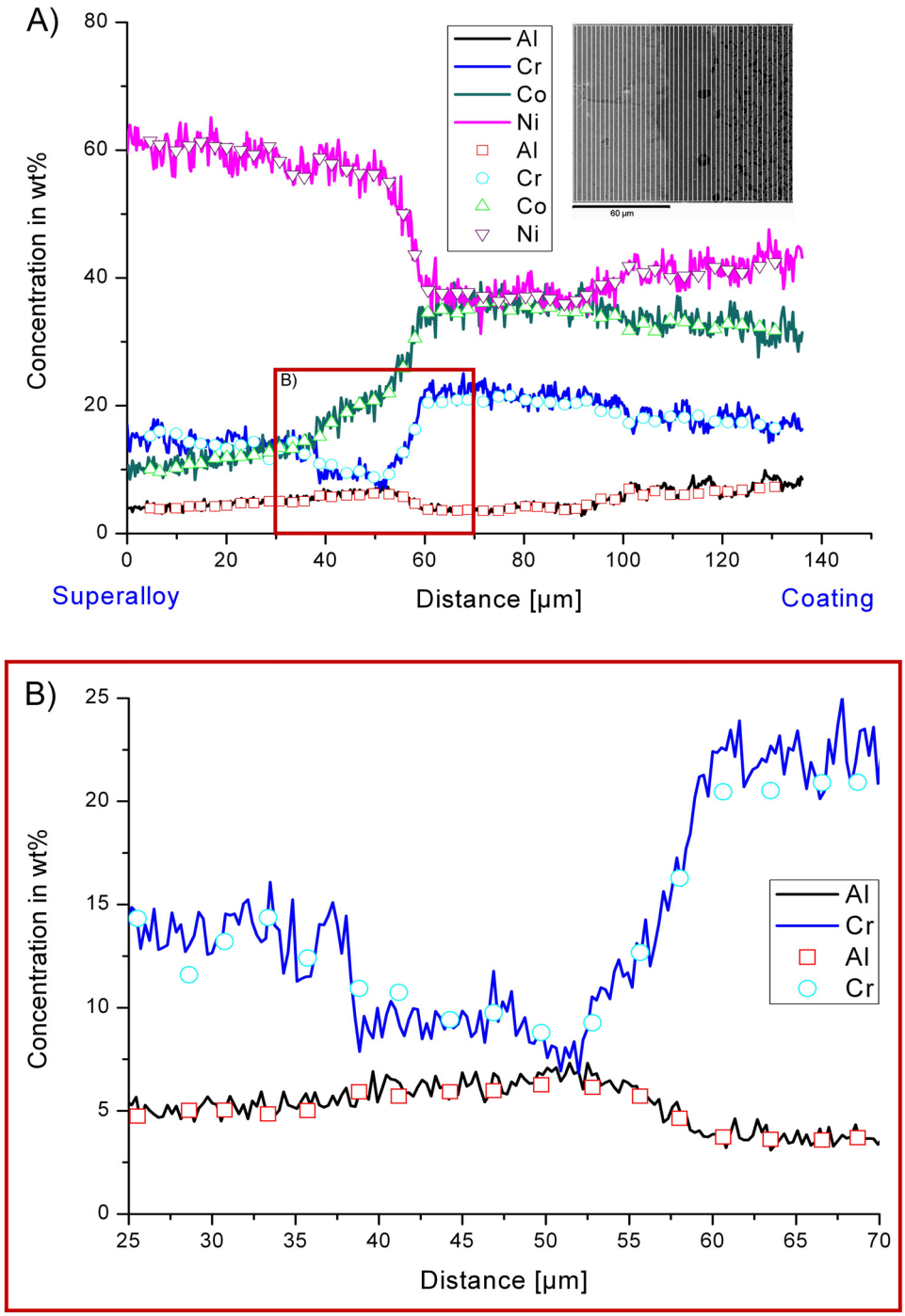

Figure 9: A) Comparison between grey scale conversion method and a traditional method where area measurements are done for the thin strips shown in the little image. The profiles obtained using the grey scale conversion method, plotted as lines, took approximately 40 minutes to acquire, while the reference measurements, plotted as dots, were performed in approximately 70 minutes. B) In the enlarged area it is visible that the sharp interfaces in the Cr profile are better defined by using the grey scale conversion method.

Plotting composition profiles based on the data in the x-ray maps allows us to closely follow the diffusion behaviour of major elements with time such as is shown for the temperature series at 875ºC in figure 10, while keeping a good resolution allowing us to observe the position of the sharp interfaces.

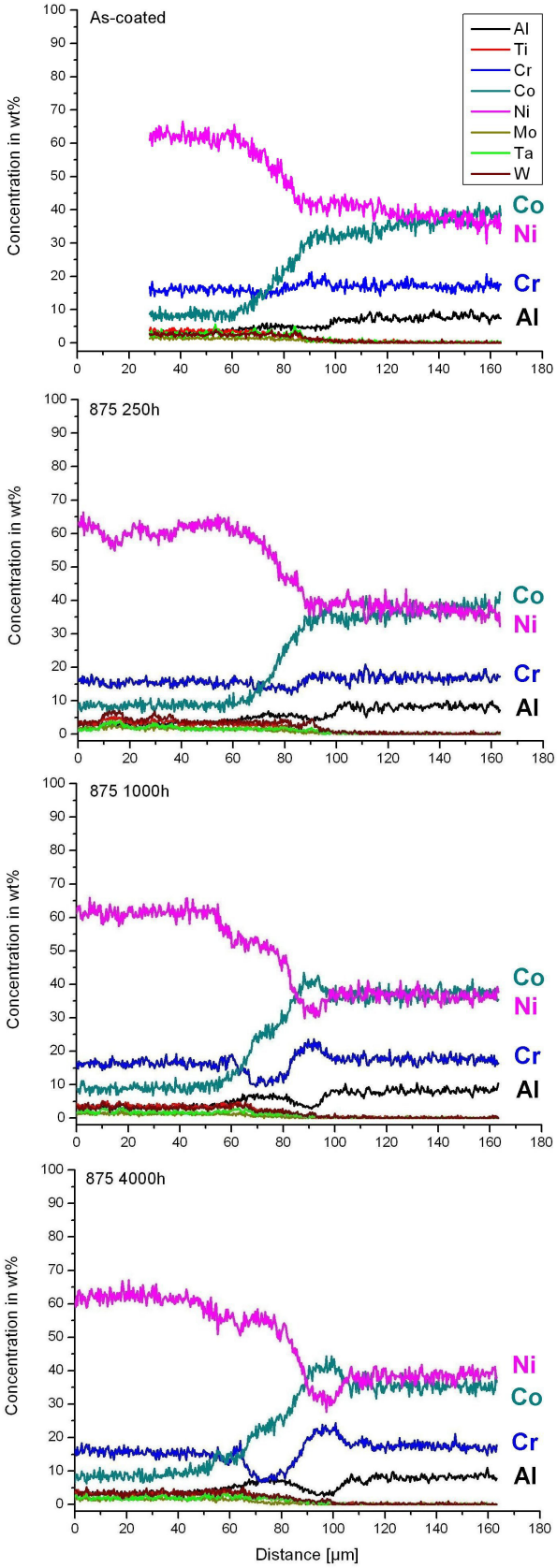

Figure 10: Change in composition profiles with time for the temperature series at 875ºC. Plotting the profiles by using the average grey-scale pixel value and then converting to concentrations allows us to follow the changes caused by interdiffusion in a way that would not be possible using standard EDS point measurements.

Accuracy of the grey-scale conversion method

The accuracy of the grey-scale conversion method was tested by making a measurement inside the superalloy and calculating the standard deviation for each element for the 512 data points across the x-ray map. The measurement result with calculated standard deviations is shown in table 4. The results show us that while there is some uncertainty in the absolute average values, the results are more than satisfactory for following the composition change across the interface for the major elements.

Table 4: Measurement results and calculated standard deviations for a *grey-scale conversion* measurement done inside the bulk superalloy.

Element	Al	Ti	Cr	Co	Ni	Mo	Ta	W
Mean±σ	3.2±0.4	3.7±0.5	16.4±0.9	9±1	61±2	1.3±0.3	1.8±0.4	3.2±0.6

Discussion

When investigating complex, multi-element and multi-phase layered microstructures such as the coating / superalloy system used as an example in the preceding sections, it is important to have a method to accurately determine average composition profiles across the interface(s), preferably also without using excessive SEM time. The current approach of grey scale conversion x-ray mapping allows us to plot average composition profiles from digital element maps, which can be collected very quickly using modern SEM EDS equipment. It also allows us to obtain true average composition profiles even though the microstructure contains large volume fractions of discrete particles, in this case carbides, γ'- and β-particles. Since it was not possible to group pixels along lines in the available SEM EDS software, this was done using specific image analysis software. In this way the *grey-scale conversion* method presented in this article is not dependent on the SEM software used to obtain the digital image maps. The SEM time used is also significantly shorter than for point by point measurements and line scans if satisfactory count statistics are to be obtained.

Table 5: Average times for obtaining profiles.

	SEM time per measurement / [minutes]	Typical SEM time (total) / [minutes]
Line scan (100) scans)	1½-8 *	400
Point by point average (20 points)	~ 1½	30
Point by point average (3x20 points)	~ 1½	90
Compositional imaging**	350-18000	~3000
Area strips (50 strips)	~ 1½	~ 75
Spectrum imaging***	~ 40	~ 40
Grey-scale conversion mapping	~ 40	~ 40

Table 5. Notes:

*** Goodhew et al. (2001)**

**** Typical times listed in Goldstein et al. (1992) are 0.1-5 s dwell time per pixel. For 512x416 pixels this gives the values listed in the table.**

*****The time given for spectrum imaging is the time it takes to collect the data, whether the data manipulation can be performed directly in the SEM software depends on the options for pixel grouping in the specific program. If it is not possible to group the pixels in vertical (or horizontal) lines, *grey-scale conversion* can simply be used on elemental maps exported from the spectrum imaging software.**

Another consideration besides the time used to obtain profiles is of course the accuracy of the results. It is clear from figures 7 and 8, that the result obtained using *grey-scale conversion* is a considerable improvement compared to conventional point by point measurement methods. The same is expected to be the case in comparison with conventional line scans unless an extremely large number of line scans is performed. Compositional imaging could potentially offer a better accuracy but the SEM time associated with producing a high accuracy compositional image would be unacceptable for the purpose of producing line profiles. Using a number of area strips as was shown in figure 9 gives approximately the same result for only slightly longer SEM time but this method requires prior knowledge of the scale of microstructural and compositional variations to choose the appropriate width of each strip, whereas this is not the case for the grey scale conversion method.

For spectrum imaging systems the post processing possibilities are already numerous. Directly implementing a pixel selection criteria that allows the choice of pixels in strips along lines parallel to an interface of interest would make it unnecessary to export the pictures and do a grey-scale conversion. If this has not been implemented, exporting the actual grey-scale elemental maps and doing an external grey-scale conversion is a good and time saving

alternative to making pixel by pixel measurements. For inhomogeneous microstructures such as systems containing a large amount of precipitates, as in the example given of the interface between MCrAlY coatings and superalloys for gas turbine components, the method is especially well suited.

In the following, the power and usefulness of grey scale conversion mapping is illustrated by a comparison to the results of thermodynamic modelling of interdiffusion between the multilayered structures. The measured average composition profiles can be compared with results from modelling software and used to estimate the accuracy of the model. If the modelling result is able to adequately describe the measured development in composition profiles then it can be used to for instance predict formation of phases at the interface, or to estimate regression of β-phase, Al-reservoir phase, due to interdiffusion and used for an overall lifetime model for the coating/ substrate system. It is important to state that using the grey scale conversion method does not remove the influence of discrete particles on the measured profiles but only suppresses this effect, thereby allowing us to measure average profiles that are close to the one-dimensional profiles obtained via modelling. When applying the measurement method it should be considered that measuring on a two phase area with a distribution of small particles, 1-3 μm in diameter, will give a different averaged result than for a two phase area with much larger particles, containing the same phase with the same volume fraction. For the latter case it would be much more appropriate to measure composition and volume fraction of each phase.

The interdiffusion in the MCrAlY/IN738 system was modelled using the software DICTRA. The model is a so-called dispersed phase model where all diffusion is assumed to take place in a continuous matrix phase and particles such as β-particles or γ'-particles are considered as obstacles for the diffusion.

Figure 11 shows a comparison of the modelled and the measured profiles. The behaviour of Al and Cr is particularly interesting because these elements are extremely important for the protective characteristics of the coating against oxidation in the aggressive environment in the gas turbine. The modelled results show the correct trends for the diffusion behaviour of both elements. Without the experimental data that was obtained using the grey-scale conversion method it would not be possible to critically assess the quality of the modelling.

The detailed modelling of the interdiffusion behaviour will be the subject of a future paper.

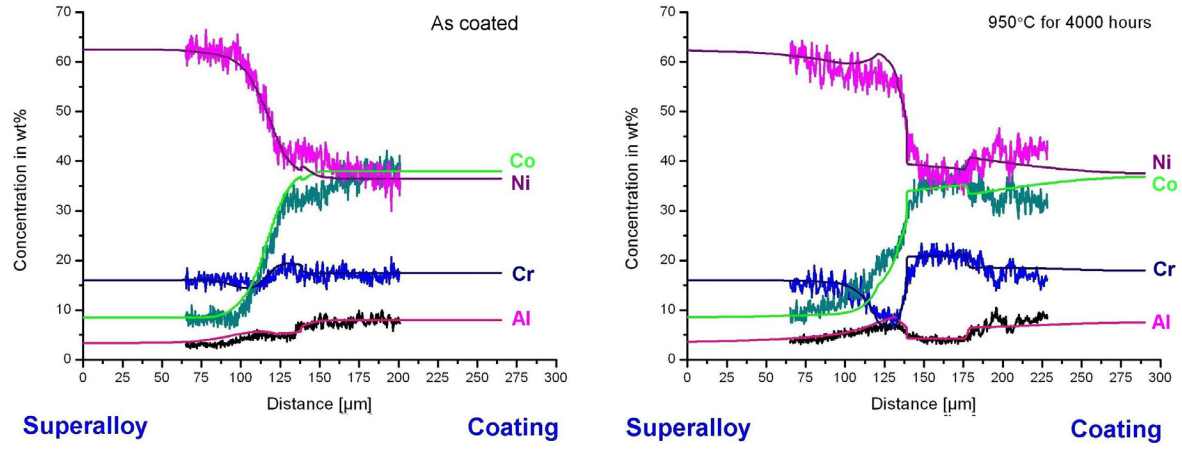

Figure 11: Result of modelling using DICTRA. The modelled profiles are the straight lines that end up at the initial values for coating and superalloy at the end-points. The experimental profiles provide an excellent tool for critically assessing the quality of the modelled results.

Conclusion

Grey scale conversion of x-ray mapping and the calculation of average composition profiles for elements of interest in a multi-element system is an excellent way of observing interdiffusion behaviour for complicated layered structures in the SEM. By taking the average grey-scale intensity value of strips of pixels in which the strips are oriented parallel to the interface it is possible to suppress the influence of inhomogeneities. It is then possible to obtain true average curves that can be directly compared to results of thermodynamic modelling.

The profiles can be obtained using a minimum of SEM time, especially compared to the normal point by point measurement method that has traditionally been used for this kind of system. For microstructural systems that contain a large amount of small precipitates, using the information stored in the digital x-ray maps for measuring 1-D line profiles across interfaces is far superior to measuring line profiles using point by point measurements.

This way of measuring composition profiles will be an important tool in obtaining a better knowledge about the interdiffusion behaviour between coatings and substrate alloys for gas turbine components.

Acknowledgements

The present research was carried out under the research consortium IMPRESS. The authors wish to acknowledge the financial support from Energy E2 A/S and the Danish Research Agency (Grant no. 26-03-0275).

The present project is part of the European COST 538 action: *High Temperature Plant Lifetime Extension*.

References

Borgenstam A., Engstrom A., Hoglund L., Agren J. (2000) DICTRA, a tool for simulation of diffusional transformations, Journal of Phase Equilibria, 21, 3, 269-280.

Cosslett, V.E. and Duncumb, P. (1956) Micro-analysis by a flying-spot X-ray method, Nature, 177, 1172-1173.

Friel, J.J. (2004) Compositional imaging. Advanced Materials & Processes, December 2004, 21-23.

Goldstein, J.I., Newbury, D.E., Echlin, P., Joy, D.C., Fiori, C. And Lifshin, E. (1992). Scanning Electron Microscopy and X-Ray Microanalysis. Plenum Press, New York .

Goodhew P.J., Humphries, F.J. and Beanland R. (2001), Electron Microscopy and Analysis - 3rd Edition. Taylor & Francis, London.

Mott, R.B. and Friel, J.J. (1999) Saving the photons: mapping X-rays by position-tagged spectrometry. Journal of Microscopy. Vol 193, 2-14.

Newbury D.E., Fiori C.E., Marinenko R.B., Myklebust R.L., Swyt C.R., Bright D.S. (1990) Compositional Mapping with the Electron Probe Microanalyzer: Part I, Analytical Chemistry, vol. 62, No. 22 (1990), 1159A-1166A.

Newbury D.E., Fiori C.E., Marinenko R.B., Myklebust R.L., Swyt C.R., Bright D.S. (1990) Compositional Mapping with the Electron Probe Microanalyzer: Part II, Analytical Chemistry, vol. 62, No. 24 (1990), 1245A-1254A.

Appendix II

Estimation of Metal Temperature of MCrAlY Coated IN738 Components Based on Interdiffusion Behaviour

Accepted by:

Energy Materials: Materials Science & Engineering for Energy Systems
26/01/2006

Estimation of metal temperature of MCrAlY coated IN738 components based on interdiffusion behaviour

K. V. Dahl* and J. Hald

Interdiffusion at the interface between a Co–36·5Ni–17·5Cr–8Al–0·5Y, MCrAlY coating and the underlying IN738 superalloy was studied in a large matrix of specimens isothermally heat treated up to 12 000 h at temperatures 875, 925 or 950°C. Microstructural investigations and calculated phase fraction diagrams show that a precipitate free zone forms between the coating and superalloy and grows with time. The width of the growing zone was estimated on the basis of average intensity profiles obtained from experimental X-ray maps measured using energy dispersive spectroscopy (EDS) in a scanning electron microscope (SEM). A simple parabolic growth model was set up for estimating the metal temperature near the coating/substrate interface based on the growth kinetics of the precipitate free zone. Parameters for the model were extracted from measurements of the width of the growing precipitate free zone with time. The developed model was used to estimate metal temperatures for a service exposed, first stage gas turbine blade.

Keywords: MCrAlY, Superalloy, Interdiffusion, Metal temperature

Introduction

Hot section components for gas turbines such as turbine blades are coated to protect the substrate material from the aggressive environment in the turbine. Degradation of the coating happens because of both oxidation at the surface and interdiffusion between coating and the underlying substrate material.

Modern turbine blades are typically manufactured from a nickel base superalloy and one or several coatings are applied. A much used metallic coating is the MCrAlY (M=Ni,Co) type containing high amounts of chromium and aluminium. During high temperature service, the chromium and aluminium provide protection against hot corrosion and oxidation by forming stable oxides at the surface. The lifetime of the coating therefore depends on the availability of these two elements, which will be removed from the coating by the oxidation process. Because of concentration differences between substrate and coating, aluminium and chromium can also be removed from the coating by diffusion into the substrate. Several authors have reported that this effect has a significant influence on the lifetime of coatings especially at high temperatures.[1–7]

Both the rate of oxidation at the surface and the rate of diffusion into the substrate depend heavily on temperature. The metal temperature of the coating is therefore one of the most important input parameters for models used to predict the coating lifetime. Because of the complex design of hot section components such as turbine blades (aerodynamic shape and internal cooling systems), large temperature differences are found for different locations in the blade. This makes direct measurement of the metal temperature near to impossible for most cases and instead sophisticated methods for estimating the temperature from the microstructure of service exposed components have been developed.

For nickel based superalloys the metal temperature can be estimated from the coarsening of the strengthening γ' phase inside the bulk superalloy.[8,9] If the component is internally cooled, this temperature may however be lower than that seen by the coating.[10]

The MCrAlY coating temperature can for instance be estimated from depletion of the β-Al reservoir phase at the surface,[10] from the growth of the interdiffusion zone between coating and substrate Ni or Co based superalloy,[10–12] or from complex phase transformations taking place in the coatings.[13]

The present work investigates the growth of the interdiffusion zone between a low Cr MCrAlY coating and the underlying IN738 superalloy in a number of specimens isothermally heat treated up to 12 000 h. The results are used to calibrate a simple model of the growth of the interdiffusion zone. Instead of using the traditional method of performing several manual measurements, the width of the interdiffusion zone is measured from average intensity/composition profiles across the interface. These profiles are produced from

Materials Technology, Department of Manufacturing Engineering and Management, Technical University of Denmark, DTU, Lyngby, Denmark

*Corresponding author, email kvd@ipl.dtu.dk

Received 12 January 2006; accepted 26 January 2006
DOI 10.1179/174892306X99723

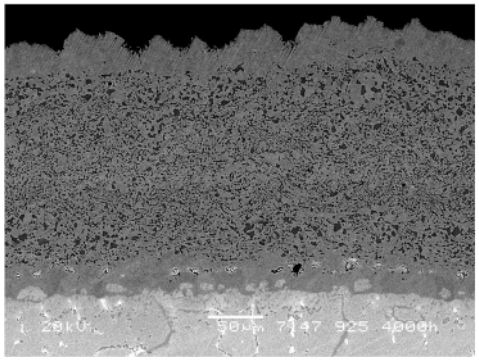

1 Image (SEM BSE) showing MCrAlY coating on specimen heat treated at 925°C for 4000 h: Al rich β phase is depleted at outer surface because of diffusion of Al to Al_2O_3 oxide scale; at interface between coating and bulk alloy β phase is depleted because of diffusion of Al into substrate

X-ray elemental maps obtained by energy dispersive spectroscopy (EDS) in the scanning electron microscope (SEM) by a method described in an earlier publication.[14]

The developed model is used to estimate metal temperatures of a service exposed MCrAlY/IN738 turbine blade.

Experimental

MCrAlY coated IN738 specimens were isothermally heat treated for up to 12 000 h at three different temperatures in order to simulate the environment in the gas turbine during service.

The compositions of the IN738 specimens and the MCrAlY coating are shown in Tables 1 and 2. The MCrAlY coating was applied by low pressure plasma spraying after which, the specimens received a standard two step heat treatment:

(i) 1120°C for 2 h then air cooled with an average cooling rate of 35°C min to 650°C.
(ii) 845°C for 24 h then air cooled with an average cooling rate of 20°C min to 650°C.

In the following the as coated condition refers to specimens having received this initial heat treatment.

After the initial heat treatment, specimens were isothermally heat treated in air at 925 or 950°C for 250, 500, 1000, 2000, 4000, 8000 and 12 000 h or at 875°C for 250, 1000, 2000, 4000 and 8000 h.

Standard metallographic procedures were used to cut, mount and polish the specimens in cross-section. Specimens were ground and then diamond polished to 1 μm finish. The metallographic specimens were then coated with ~50 nm evaporated carbon for observation in a JEOL 5900 SEM equipped with an INCA 400 EDS system from Oxford Instruments.

The interface between coating and superalloy was studied in cross-section under both polished and etched condition using backscatter contrast.

Cross-sections of the first stage MCrAlY coated IN738 blade exposed for 22 000 h in a gas turbine at Svanemoellevaerket in Denmark were prepared and examined in SEM in the same way as the isothermally heat treated specimens.

The service exposed turbine blade was coated with a slightly different coating richer in chromium than the isothermally heat treated specimens. The average specified composition of this coating is shown in **3**.

Table 1 Average composition of MCrAlY coating, wt-%

Ni	Cr	Al	Y	Co
36·5	17·5	8	0·5	Bal.

Table 2 Average composition of IN738 superalloy, wt-%

Cr	Co	Al	Ti	W	Ta	Mo	C	Zr	B	Nb	Ni
16·0	8·5	3·4	3·4	2·6	1·75	1·75	0·11	0·05	0·01	0·85	Bal.

Microstructural observations of isothermally heat treated specimens

Figure 1 shows a SEM backscatter image of the MCrAlY coating and the IN738 superalloy. The MCrAlY coating consists of a Co, Ni, Cr rich matrix phase with discrete β-NiAl particles dispersed throughout the coating.

The polycrystalline IN738 superalloy has a typical γ/γ' microstructure with the γ'-$Ni_3(Al,Ti)$ particles distributed homogeneously in the Ni rich fcc γ matrix. Throughout the alloy Ti and Ta rich primary carbides are found which appear white in the presented backscatter images because of their high mean atomic number. Secondary chromium carbides formed during the second step of the initial heat treatment are found discretely in grain boundaries.

At the outer surface of the coating a zone depleted of β-NiAl can be found where the diffusion of aluminium from bulk coating to the surface has resulted in dissolution of the β particles. When all β particles have disappeared the coating has been depleted of aluminium and is close to end of life, because it will no longer be able to sustain the protective Al_2O_3 layer at the surface.

Figure 2 illustrates the complicated microstructural changes with time at the interface between coating and superalloy for specimens isothermally heat treated at 925°C for 250, 4000 and 12 000 h. Diffusion across the interface results in a depletion of aluminium from the coating and at the same time causes several microstructural changes. On the coating side of the interface coarsening of β particles is clearly visible and loss of aluminium into the substrate results in formation of a β depleted γ zone that grows with time. After short exposure times this zone contains small precipitates, most likely γ' particles (Fig. 3), but after longer exposure times the precipitates can no longer be seen in the SEM. At the original interface between coating and substrate, Kirkendall voids are formed. The Cr rich α and σ-(Cr_xCo_y) phases reported by other authors.[13,15] were not observed in the present specimens, probably because of relatively low Cr content of the present MCrAlY coating.

On the substrate side of the interface, an increase in aluminium owing to diffusion from the coating and enrichment of Ti and Ta owing to the dissolution of

Table 3 Composition of MCrAlY coating from service exposed blade, wt-%

Ni	Cr	Al	Y	Si	P	Co
36	25	7	0·1	0·7	0·3	Bal.

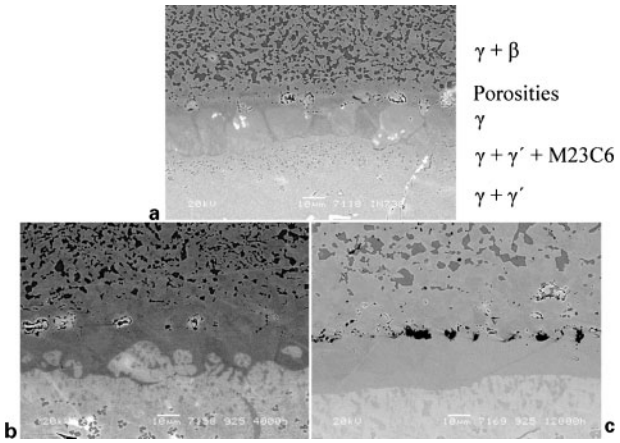

2 Images (SEM BSE) of interface between coating and substrate for specimens heat treated at 925°C for *a* 250, *b* 4000 and *c* 12 000 h: β phase in coating coarsens with time and interdiffusion zone between coating and substrate grows

primary carbides results in the formation of a continuous zone of γ' phase, similar to observations by Di Martino and Thomson.[16] Furthermore, the dissolution of primary carbides results in precipitation of Cr rich, $M_{23}C_6$ carbides, as seen in Fig. 4, where the Ti and Ta rich primary carbides are surrounded by $M_{23}C_6$ carbides. The $M_{23}C_6$ carbide precipitation can also be observed on Cr X-ray maps as shown in Fig. 5. A similar phenomenon has previously been observed by Singheiser *et al.*[4]

Composition and intensity profiles across interface

Composition profiles across the interface were measured using a method that converts intensity information from grey scale elemental maps (EDS X-ray maps) to

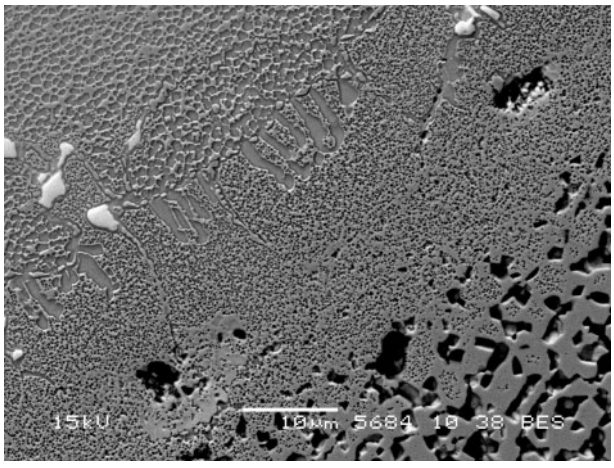

3 Shadow image (SEM BSE) of specimen heat treated at 875°C for 250 h: in lower right part of image, etching has removed large β phase particles in coating that therefore appear dark; in top left of image γ/γ' microstructure with primary Ta–Ti carbides (white) is visible and at interface towards superalloy continuous γ' layer is starting to form; small precipitates that are most likely γ' can be observed in zone between β phase rich coating and unaffected superalloy

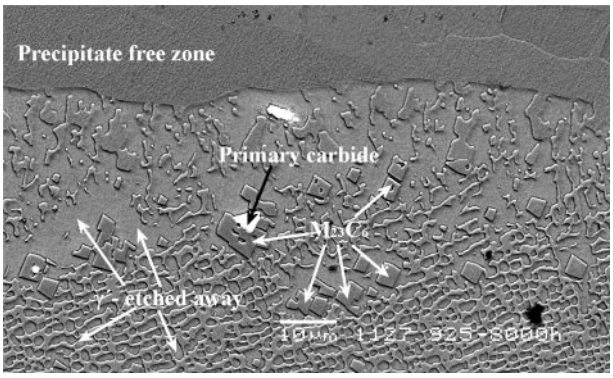

4 Image (SEM BSE) of etched specimen heat treated at 925°C for 8000 h: after long heat treatment times primary Ti–Ta rich carbides (white) near interdiffusion zone start to dissolve and are surrounded by chromium rich $M_{23}C_6$ carbides

composition profiles.[14] The profiles represent average composition profiles across the interface calculated based on the two-dimensional (2D) information stored in X-ray elemental maps. These profiles provide direct information about the interdiffusion behaviour at the interface and about the width of the interdiffusion zone.

Figure 6 shows measured composition profiles for the as coated specimen and for specimens heat treated at 875, 925 and 950°C for 4000 h. The profiles show that significant interdiffusion takes place at the interface and that especially the profiles for chromium and aluminium clearly change with time. An interdiffusion zone high in chromium and low in aluminium is formed between the coating and the substrate (precipitate free zone), and a chromium depleted zone richer in aluminium is formed at the interface towards the substrate and results in the formation of a continuous γ' layer.

Under the assumption of local equilibrium, the measured composition profiles can be converted into phase fraction diagrams using the calculation software Thermo-Calc.[17] The calculations were done considering the elements Al, Ti, Cr, Co, Ni, Mo, Ta and W and the phases fcc, bcc, γ', β and σ. The thermodynamic database Ni DATA Version 4 from Thermotec, Ltd[18] was used for the calculations. Carbon was not included in the calculations, because the carbon profile can not be measured using EDS equipment, instead the software predicted the presence of Cr rich σ phase at the location where Cr rich $M_{23}C_6$ carbides were found according to Fig. 5. The presence of σ phase in the calculated diagrams must therefore be interpreted with caution, because in the actual microstructure, $M_{23}C_6$ carbides

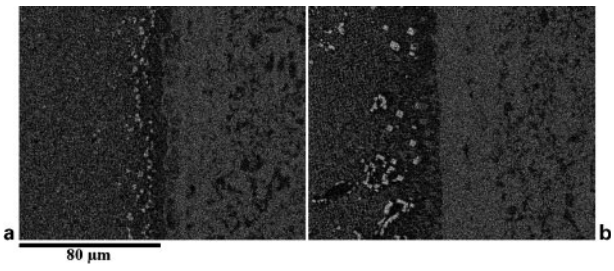

a 8000 h at 875°C; *b* 8000 h at 925°C

5 X-ray maps (EDS) showing Cr rich $M_{23}C_6$ carbides on substrate side of interface

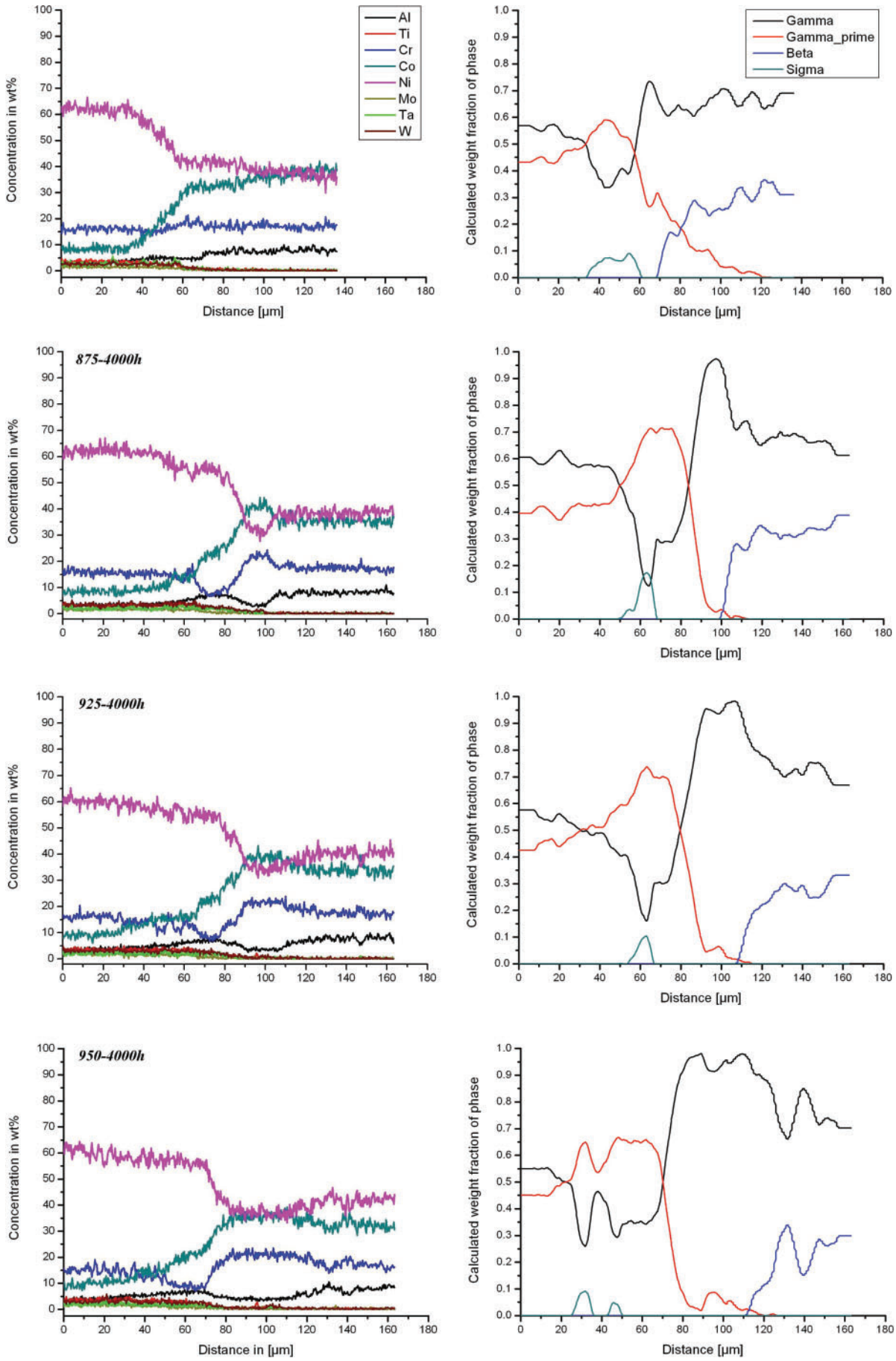

6 Left column – average composition profiles across interface measured using method described in Ref. 14: profiles after initial heat treatment and after 4000 h at 875, 925 and 950°C are presented; IN738 superalloy is located to left and MCrAlY coating to right; right column – phase fraction diagrams calculated from measured profiles

may have precipitated instead of or together with σ phase.

The increased γ' volume fraction at the superalloy side of the interface is clearly visible in the calculated diagrams. The precipitate free zone has not yet been formed in the as coated specimen but is observed for all the three specimens heat treated for 4000 h.

The observed behaviour is similar for all three temperatures, except that the diffusion of course occurs faster at high temperatures.

The width of the interdiffusion layer is traditionally measured using either a light optical microscope (LOM) or a SEM. Both techniques normally require etching of the specimen. However, backscatter contrast can be used in the SEM if the atomic number contrast is large enough between the layers of interest, and then etching is unnecessary. The traditional methods then require a large number of measurements in order to be representative for the system and obtain satisfactory count statistics.[12]

In the present approach the width of the interdiffusion zone is measured on the basis of the composition profiles. For simplicity intensity profiles directly measured in the SEM can also be used, which speeds up the evaluation procedure, because extra calculations (background subtractions, matrix corrections, etc.)[14] to convert intensity profiles into composition profiles are avoided.

For the present MCrAlY/IN738 system, composition profiles and calculated phase fractions presented in Fig. 6 show together with microstructure evaluation that the width of the precipitate free zone can be related to the aluminium and chromium profiles. It was therefore chosen to use measured Al X-ray maps and resulting average Al intensity profiles as basis for measurement of the growth of the interdiffusion zone with time. An example of a measured X-ray map and the corresponding average intensity profile calculated from grey scale pixel values in the X-ray map is shown in Fig. 7. The average intensity profile is obtained by calculating mean grey level intensities for pixels in strips parallel to the interface of interest. A mean grey scale pixel value is thus obtained for each strip and an average profile across the interface can be plotted. The X-ray maps obtained in the SEM have a pixel resolution of 512×416 pixels. This means that the average intensity profile has 512 data points across the interface and each of these data points is an average of 416 data points (pixels). In this way, influence of single particles is suppressed and only average variations in intensity and thus composition that are related to the layered geometry, such as interdiffusion or near interface denuded zones, are measured.

In the intensity profiles for aluminium the γ' rich zone is visible as a large peak next to the substrate. Next to this peak follows the low aluminium zone almost free of precipitates, in the following simply referred to as the precipitate free zone. Another peak is then reached at the start of the β rich zone in the coating.

The precipitate free zone is expected to grow following a simple parabolic growth law, but it is not immediately clear how the width of this zone can be coupled to the intensity profiles and therefore the three different methods of quantifying the width from the measured profiles were tried. Because the measured

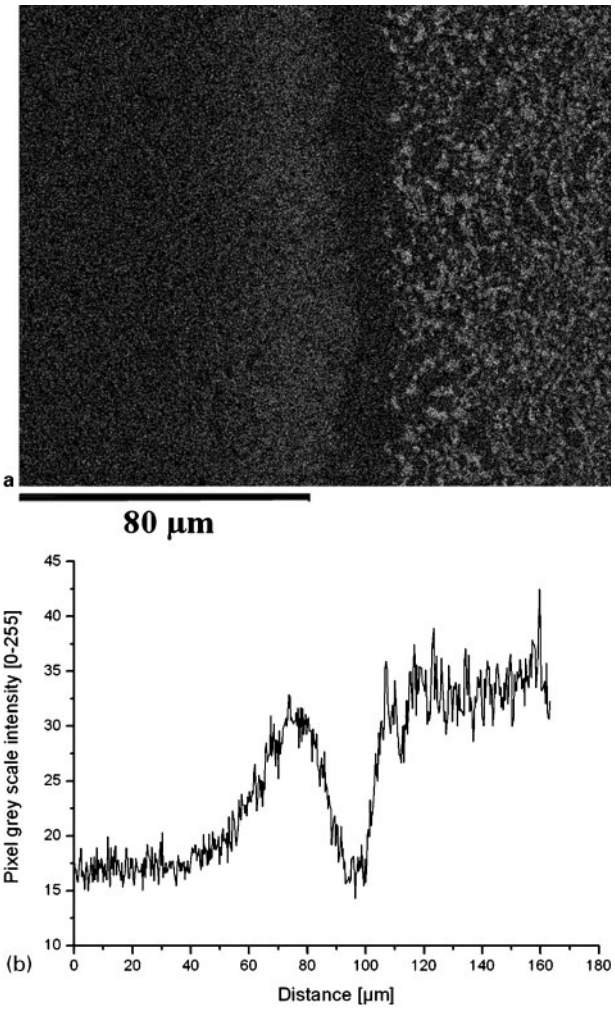

7 *a* aluminium EDS X-ray map for specimen heat treated at 875°C for 4000 h: IN738 substrate is located at left side of image; *b* mean grey scale intensity profile for aluminium calculated from mean grey scale pixel value in X-ray map of strips parallel to interface (vertical strips)

intensity profile contains some noise, a filtering algorithm (Savitzky–Golay filtering algorithm[19]) was first used to smooth the profiles. The three different methods are illustrated in Fig. 8. The first method, which is the most direct measurement of the actual width of the precipitate free zone, was very difficult to apply to profiles for short heat times and also for longer heat treatment times for the low temperature (875°C), because no plateau has formed at the minima between the two peaks. The second method was too inaccurate, because the distance between the maximum and minimum intensity values vary locally within each isothermally heat treated specimen. This gave large variations in values measured at different locations within the same isothermally heat treated specimens. Measuring the distance between the first γ' peak and the first β peak (method 3) was found to give results with good reproducibility.

Measured X-ray maps with resulting intensity profiles for the specimen in the as coated condition and for the specimens heat treated for 4000 h are shown in Fig. 9. The effect of temperature on the growth of the interdiffusion zone is clearly visible.

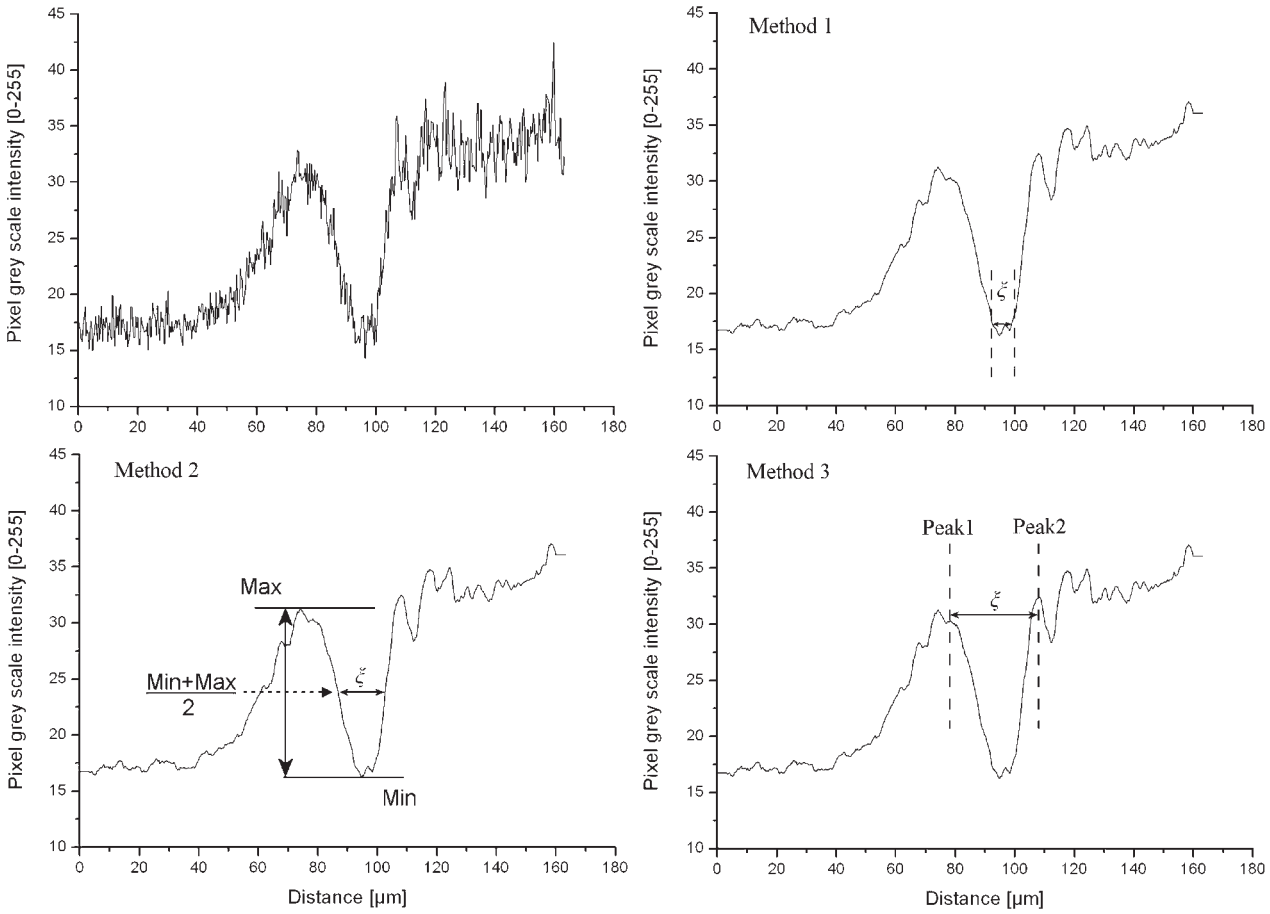

8 Same Al intensity profile shown in Fig. 7 after filter was applied to reduce noise: three different measurement methods are illustrated

The accuracy of the measurement method was investigated by obtaining X-ray maps at several locations in the isothermally heat treated specimens. Six measurements were done at different locations in the three specimens heat treated for 4000 h at the three temperatures. Table 4 shows the result of the measurements and the calculated standard deviations.

Measuring the distance between these two peaks is thus an easy method that also produces measurement results with good accuracy. One important point should however be mentioned. The distance measured between the two peaks is not the same as the width of the precipitate free zone and therefore a correction is needed in order to estimate the actual width of the precipitate free zone.

In the as coated condition the deep valley between the two peaks is just starting to form, indicating that the precipitate free layer has not yet formed. This can also be observed from the calculated phase fraction diagram and the actual microstructure. In the calculated phase fraction diagrams for the three specimens heat treated for 4000 h, the ''precipitate free zone'' is visible as the middle section of the diagrams where the calculated γ phase fraction is close to 1·0. The distance between the peaks in the as coated condition was measured as 18·4 μm, and it was then assumed that the increasing distance with time between the peaks was due to the growth of the precipitate free zone only. For this assumption to hold, the slopes of the intensity profile

Table 4 Measured widths using measurement method 3 in Fig. 8 for specimens isothermally heat treated for 4000 h

No		1	2	3	4	5	6	Mean $\pm \sigma$
Width, μm	875°C	29·9	29·6	27·6	28·6	28·6	27·7	28·7 $\pm$ 0·9
	925°C	39·3	43·9	41·0	42·6	40·7	42·0	42 $\pm$ 2
	950°C	54·3	55·0	57·2	57·9	57·7	56·6	56 $\pm$ 2

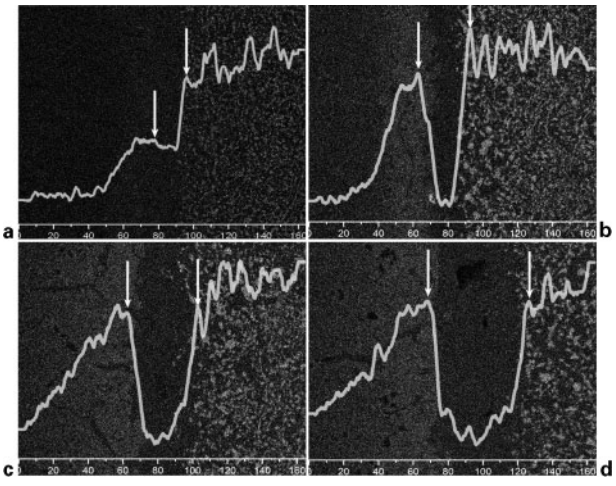

a as coated specimen; *b* specimen heat treated for 4000 h at 875°C, b specimen heat treated for 4000 h at 925°C; d specimen heat treated for 4000 h at 950°C

9 Measured X-ray maps and resulting average intensity profiles

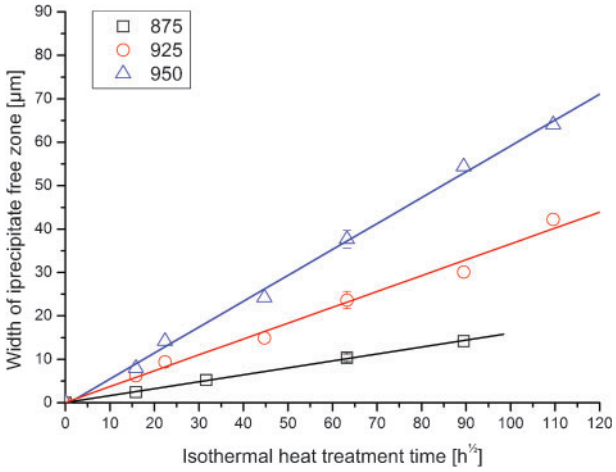

10 Measured width for precipitate free zone for all available isothermally heat treated specimens

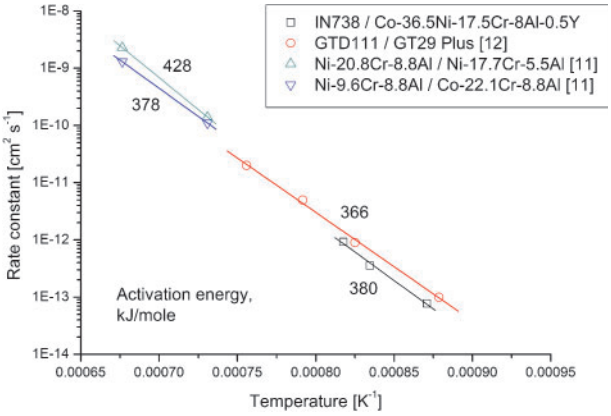

11 Rate constants for isothermally heat treated IN738/Co–36·5Ni–17·5Cr–8Al–0·5Y specimens investigated in present study and for other investigations from literature

on each side of the observed minimum should remain fairly constant, after the minimum intensity has been reached and the precipitate free zone thus has been formed. This seems to be the case.

The width of the growing precipitate free zone in the evaluated specimens was therefore estimated as the measured width minus the initial width of 18·4 μm. It could be argued that the initial width to be subtracted should be the one measured, at the moment when the precipitate free zone is first formed (when the intensity value between the peaks first reaches its minimum). This exact width is however unknown but is judged to lie within the experimental error of the width measured for the as coated specimen.

Model for estimation of service temperature

Measurements of the precipitate free zone for all the isothermally heat treated specimens were then used to set up a model for estimating the metal temperature of gas turbine hot components with compositions similar to the investigated IN738/MCrAlY specimens.

The model used was almost similar to that employed by Ellison *et al.*[12] for the growth of γ–β zones below the original interface between coating and substrate.

In order to employ the model, it is assumed that the growth of the precipitate free zone is diffusion controlled and that the coating/substrate system can be considered as a semi-infinite diffusion couple. It is also assumed that the same phases are present throughout the temperature range and that the phase fractions are fairly similar.

The growth of the precipitate free zone can then be described using a parabolic growth law according to

$$\xi^2 = k_p t$$

where ξ is the width of the growing zone at time t and k_p is the parabolic growth constant in $cm^2\ s^{-1}$.

The growth constant is described by an Arrhenius expression according to

$$k_p = k_p^0 \exp\left(\frac{-Q}{RT}\right) \Rightarrow \ln k_p = \ln k_p^0 - \frac{Q}{RT}$$

rearranging and isolating the temperature T yields

$$T = \frac{Q}{R}\left[\ln k_p^0 - \ln k_p\right]^{-1}$$

this final expression is then used to set up a calibration curve that can be used to estimate the metal temperature of service exposed components.

The results of the measurements are shown in Fig. 10.

By applying a linear fit to each temperature series a value for the rate constant k_p for the growth of the precipitate free zone at each temperature can be calculated. Plotting $-\ln k_p$ *v.* $1/T$ and fitting a straight line provides Q/R as the slope of the line and $-$ as the intercept with the y-axis. The activation energy is thus calculated as 380 kJ mol^{-1} (R=8·3145 J K^{-1} mol^{-1}) and is calculated as 14·54 $cm^2\ s^{-1}$.

The activation energy is of the same order as that reported by Ellison *et al.*[12] (366 kJ mol^{-1}) for the growth of the γ–β zone for a CoCrAlY/GTD 111 system. Figure 11 shows an Arrhenius plot of the temperature dependence of rate constants for the growth of the interdiffusion zone for the current investigation and for the investigations performed by Ellison *et al.*[12] and Levine[11].

The calculated values were then inserted into the calibration expression for the temperature and used to plot calibration curves such as that shown in Fig. 12 for a service time of 8000 h.

Use of model on service exposed blade

The developed model was used to estimate metal temperatures of the first stage MCrAlY coated IN738 blade exposed for 22 000 h in a gas turbine at Svanemoellevaerket in Denmark. The blade was sectioned at 70% blade span (measured from the root section) where visual inspection indicated that the coating was in the worst condition.

The applied MCrAlY coating had a composition with higher Cr than the isothermally heat treated specimens used for construction of the model. However, the Al intensity profiles obtained in the SEM was found to behave in a way similar to the isothermally heat treated specimens and therefore it was assumed that the developed model could be applied with reasonable accuracy. This assumption is most probably good at

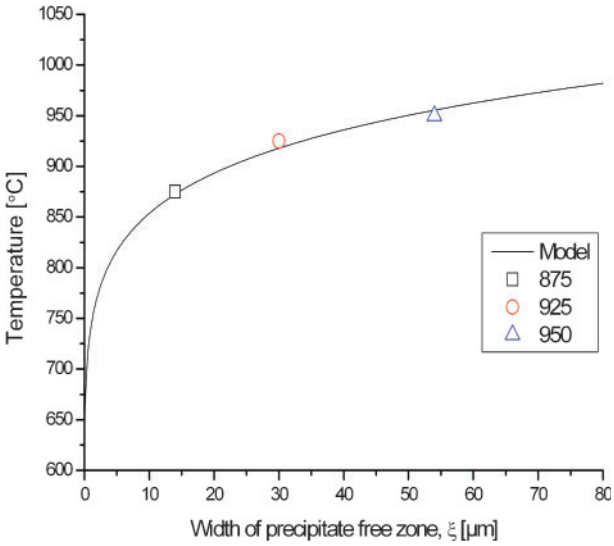

12 Temperature calibration curve for 8000 h, calculated from data extracted from isothermally heat treated specimens: three experimental points for 8000 h are plotted to illustrate fit of model

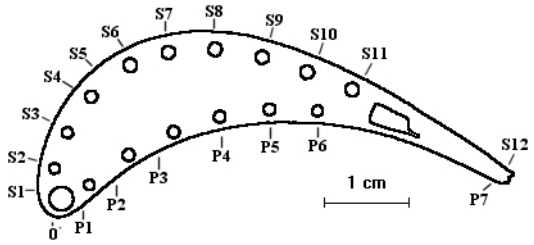

13 Location of measurement points along suction and pressure sides of service exposed turbine blade

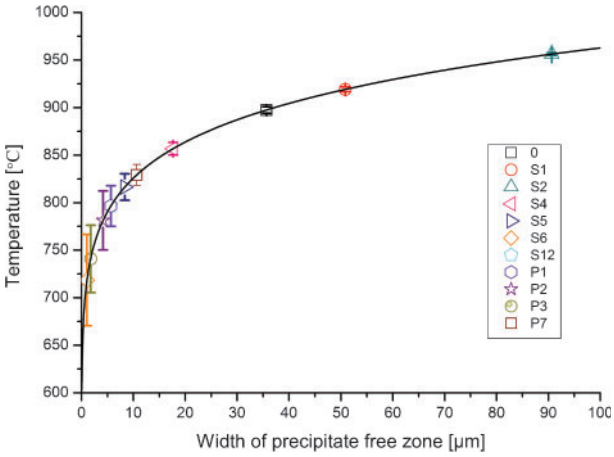

14 Plot of calibration curve for 22 000 h and estimated metal temperatures for chosen locations shown in Fig. 13

high temperatures, whereas the increased Cr content will result in formation of more σ phase at lower temperatures (below ~850°C).

Al intensity profiles at the interface between coating and superalloy were obtained at the locations shown in Fig. 13. The width of the precipitate free zone at different locations was measured and compared with a calculated calibration curve for 22 000 h. The measured widths between peaks and estimated metal temperatures

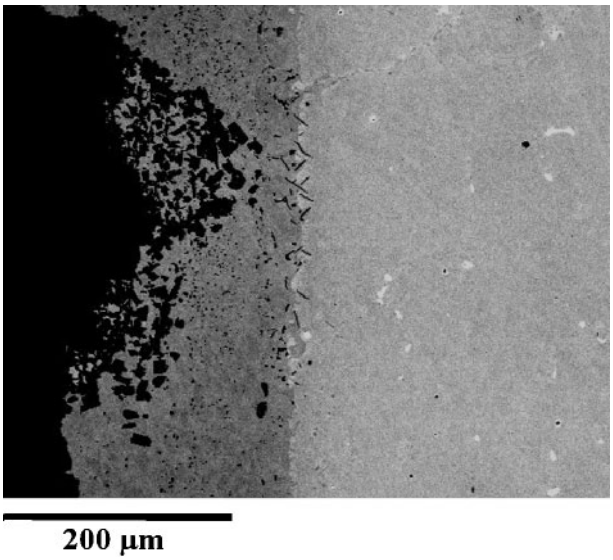

15 Local hot spot; coating has been totally depleted of β phase and most of coating has been eaten away: internal oxidation can be seen at interface towards bulk superalloy

are listed in **5**. The resulting temperature calibration curve with experimental points plotted is shown in Fig. 14.

The estimated temperatures increase along the suction side; from leading edge to the measurement point S2. At position S3, the coating was found to be exhausted, because there were no β particles left and therefore no visible intensity change to be found in the grey scale intensity plot. This measurement position was very near to a localised breakdown of the coating shown in Fig. 15 that has resulted in Al depletion of the nearby coating on both sides of the defect, which of course introduces 2D diffusion effects. The β phase depletion can therefore no longer be approximated by one-dimensional (1D)

Table 5 Measured widths and estimated metal temperatures: standard deviation is based on ±2 μm standard deviation found for measurements in Table 4

Location	Measured width between peaks, μm	Estimated temperature $\pm\sigma$, °C
0	54	897±4
S1	69	919±3
S2	109	956±2
S3	Exhausted	N/A
S4	36	857±7
S5	27	816±14
S6	19	698±>50
S7	Cold	Cold
S8	Cold	Cold
S9	Cold	Cold
S10	Cold	Cold
S11	19	698±>50
S12	24	796±21
P1	24	796±21
P2	23	787±27
P3	20	738±>50
P4	20	738±>50
P5	20	738±>50
P6	22	775±37
P7	29	829±11

interdiffusion between coating and substrate. At S4 the coating is intact and the temperature has fallen compared with S2 and continues to fall towards S6. Through the middle section (S7–S10) no significant layer growth could be measured and the coating was in good condition. At the trailing edge the temperature increases again, but the estimated temperature is low compared with the leading edge of the blade.

Along the pressure side the estimated temperature falls off rapidly from the leading edge and along the blade. Nearer to the trailing edge the estimated temperature increases (P6 and P7) and the estimated temperature ends up being higher than on the suction side of the blade.

At locations where estimated temperatures were lower than ~850°C a new Cr rich phase, not found in the isothermally heat treated specimens was observed in the service exposed blade. The phase is observed as particles in the coating and has a brighter intensity than the surrounding matrix and the β particles. It was not observed at S4 (estimated temperature of 857°C) but was found at both S5 and P7 (estimated temperatures of 816 and 829°C) and at all locations with lower estimated temperature. The volume fraction of this phase was found to increase with decreasing temperature. Figure 16 shows measured composition profiles for the location S5 and calculated phase fractions shown on top of the actual microstructure at S5. Energy dispersive spectroscopy measurements of the composition of the new phase fit with the σ-(Cr_xCo_y) phase and this is also predicted by the Thermo-Calc software. A σ peak in the calculated phase fraction diagrams coincides perfectly with the increased volume fraction of the phase visible in the underlying backscatter image. On the superalloy side some σ phase is also predicted but is not seen in the microstructure at S5, most probably because Cr rich $M_{23}C_6$ carbides that could not be included in the calculations precipitate instead. At the colder locations S7–S10, both $M_{23}C_6$ carbides and precipitates with the same composition as the coating σ phase precipitate with a plate like morphology in the superalloy near the coating.

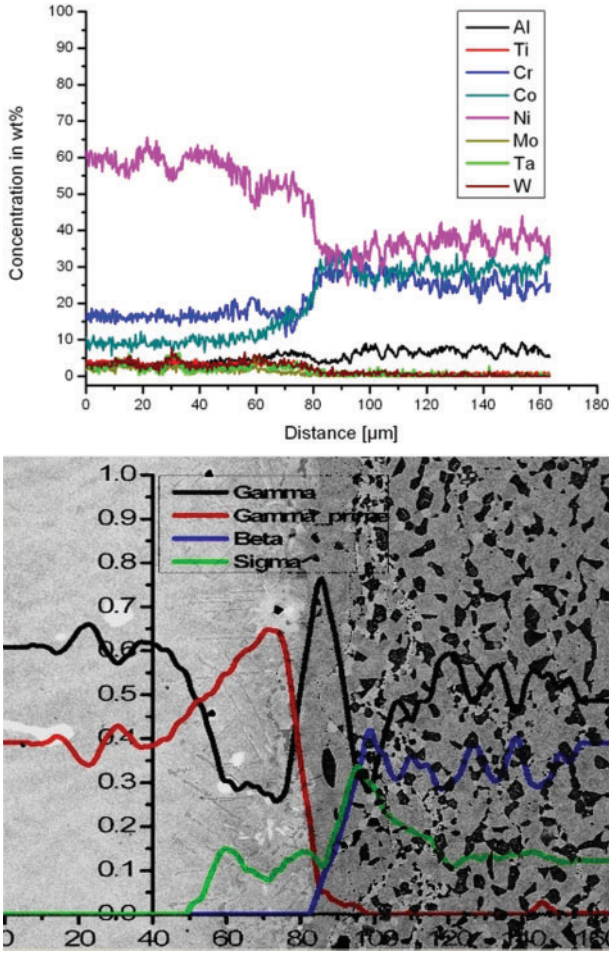

16 Composition profiles measured at S5 and calculated phase fractions superimposed on SEM BSE image of actual microstructure: plate like precipitates seen on superalloy side of interdiffusion zone are $M_{23}C_6$ carbides; at lower temperatures, σ phase also precipitates at this location with same morphology but with brighter intensity in BSE image

Discussion of model and limits to its application

As seen from the above example, the developed model and measurement method can be used to estimate the metal temperature at the interface between MCrAlY coating and IN738 substrate along the blade geometry. Because the life time of the coating is estimated to be ~25 000 h by the manufacturer, while the substrate material has an estimated life time of ~100 000 h, it is of great importance to have a method for estimation of the metal temperature close to the coating. In this way the current model has an advantage compared with for instance using coarsening of the γ' phase for temperature estimation.

The special measurement method used for setting up the current model has the advantage that it only requires one measurement for each location instead of numerous measurements traditionally used. The method therefore requires less interaction from the operator, which should increase reproducibility when different operators or laboratories carry out the investigations. Also, the intensity profiles are obtained from specimens in the polished condition and therefore uncertainties related to etching effects are avoided.

At high temperatures where the coating is severely degraded the model has good accuracy. The accuracy is poorer at low temperatures and also for short times, which is illustrated by the standard deviations plotted in Fig. 14. For coating life estimation this loss of accuracy for low temperatures does not seem too severe, since hardly no effects of interdiffusion are visible for locations with an estimated temperature below ~750°C. The life time of the coating will instead be limited by coating condition at hot spots along the blade geometry where the model has good accuracy. The estimated metal temperature can therefore be used as input parameter in overall models of coating life like that described by Chan *et al.*[5]

For other purposes like thermomechanical modelling where it is also interesting to know the exact temperature in the lower temperature range, the temperature estimate is less accurate but can still be used to compare different locations in components.

The loss of accuracy with lower temperature is however not unique for this model but applies to all models based on diffusion controlled phenomena.

It should be mentioned that the authors can only discuss the accuracy of the model in terms of reproducibility and not the absolute precision of the obtained results, because the actual metal temperature is of course the unknown that the authors aim to obtain. The rigorous calibration procedure from laboratory specimens should however ensure that the precision is also good.

There are a few further limitations for the developed model that should be mentioned. The most severe being that it can only be used on material systems close in composition to that of the isothermally heat treated specimens. The coating on the service exposed blade investigated in the present work had a slightly different composition (more Cr) compared with the coating applied to the isothermally heat treated specimens, but it was found that the behaviour for the service exposed blade at high temperatures was similar to the behaviour observed in the isothermally heat treated specimens. At temperatures below an estimated temperature of 850°C, it was found that σ phase started to precipitate. This will of course change the overall behaviour of the system and therefore the accuracy of the model must be expected to become poorer with increasing volume fraction of σ phase.

The influence of the precipitation of σ phase or other phases on the diffusion behaviour at the interface and therefore on the applicability of the simple model developed can be estimated on the basis of finite difference diffusion modelling software such as DICTRA.[20] This will be the subject of a future publication.

From the example shown it is also apparent that it is not possible to estimate the metal temperature at hot spots or points of local degradation where the β phase has been totally depleted, because there will be no Al peak to measure against in the intensity plots. Measurement will also be difficult at locations where the temperature has been so low that no significant interdiffusion has occurred such as the positions S7–S10 for the investigated turbine blade.

Conclusion

Interdiffusion at the interface between a Co–36·5Ni–17·5Cr–8Al–0·5Y, MCrAlY coating and the underlying IN738 superalloy was studied in a large matrix of specimens isothermally heat treated up to 12 000 h at temperatures 875, 925 or 950°C. Microstructural investigations and calculated phase fraction diagrams show that a precipitate free zone forms between the coating and superalloy and grows with time. The width of the growing zone was estimated on the basis of average intensity profiles obtained from experimental X-ray maps measured using EDS in a SEM. Three different methods for measuring the width of the precipitate free zone from the intensity profiles were investigated. The interdiffusion at the interface results in the formation of distinct peaks in the aluminium intensity profiles and measuring the distance between these peaks gave the most reproducible results.

A simple parabolic growth model was set up to estimate the metal temperature near the coating/substrate interface based on the growth kinetics of the precipitate free zone. Parameters for the model were extracted from measurements of the width of the growing precipitate free zone with time.

The developed model was used to estimate metal temperatures for a service exposed, first stage gas turbine blade. The coating on this blade had a higher Cr content than isothermally heat treated specimens, but the high temperature behaviour was found to be similar to that of isothermally heat treated specimens.

It was shown that the developed model can be used with good accuracy in the temperature range where the coating is degraded and thus that the estimated metal temperature can be used as input for models of coating life time.

Acknowledgements

The present research was carried out under the research consortium IMPRESS and is also a part of the European COST 538 action – High Temperature Plant Lifetime Extension.

The authors wish to acknowledge the financial support from Energy E2 A/S and the Danish Research Agency (grant no. 26-03-0275), and also wish to thank ERA Technology for providing heat treated specimens making this investigation possible.

References

1. J. A. Nesbitt and R. W. Heckel: *Thin Solid Films*, 1984, **119**, (3), 281–290.
2. L. Peichl and G. Johner: *J. Vac. Sci. Technol. A*, 1986, **4A**, (6), 2583–2592.
3. J. E. Morral and M. S. Thompson: *Surf. Coat. Technol.*, 1990, **43**, (1), 371–380.
4. L. Singheiser, H. W. Gruenling and K. Schneider: *Surf. Coat. Technol.*, 1990, **42**, (2), 101–117.
5. K. S. Chan, N. S. Cheruvu and G. R. Leverant: *Trans. ASME*, 1999, **121**, 484–488.
6. D. F. Susan and A. R. Marder.: *Acta Mater.*, 2001, **49**, 1153–1163.
7. R. Anton, J. Birkner, N. Czech and W. Stamm: *Mater. Sci. Forum*, 2001, **369–372**, (2), 719–726.
8. D. J. Chellman and A. J. Ardell: *Acta Metall.*, 1974, **22**, 577–588.
9. R. A. Stevens and P. E. J. Flewitt: *Mater. Sci. Eng.*, 1979, **37**, 237–247.
10. V. Srinivasan, N. S. Cheruvu, T. J. Carr and C. M. O'Brien: *Mater. Manuf. Process.*, 1995, **10**, 955–969.
11. S. R. Levine: *Metall. Trans. A*, 1978, **9A**, 1237–1250.
12. K. A. Ellison, J. A. Daleo and D. H. Boone: Proc. 6th Liège Conf., (ed. J. Lecomte-Beckers, F. Schubert and P. J. Ennis), 1523–1534; 1998, Liege, Universite de Liege.
13. K. A. Ellison, J. A. Daleo and K. Hussain: Proc. 10th Int. Symp. on 'Superalloys', (ed. K. A. Green *et al.*), 759–768; 2004, Warrendale, PA, TMS.
14. K. V. Dahl, J. Hald and A. Horsewell: submitted to *J. Microsc.*.
15. K. A. Ellison, J. A. Daleo and D. H. Boone: Proc. Conf. on 'Life assessment of hot section gas turbine components', (ed. R. Townsend *et al.*), 311–326; 1999, Edinburgh, UK, Heriot Watt University.
16. I. D. Martino and R. C. Thomson: Proc. 6th Int. Charles Parsons Turbine Conf., (ed. A. Strang *et al.*), 900–912; 2003, Dublin, Trinity College.
17. B. Sundman, B. Jansson and J. O. Andersson: *Calphad*, 1985, **9**, (2), 153–190.
18. N. Saunders: Proc. 8th Int. Symp. on 'Superalloys', (ed. R. D. Kissinger *et al.*), 101–110; 1996, Warrendale, PA, TMS.
19. A. Savitzky and M. J. E. Golay: *Anal. Chem.*, 1964, **36**, 1627–1639.
20. A. Borgenstam, A. Engstrom, L. Hoglund and J. Agren: *J. Phase Equilib.*, 2000, **21**, (3), 269–280.

Appendix III

Modelling of Interdiffusion between MCrAlY coating and IN738 superalloy

- In Manuscript

Modelling of Interdiffusion between MCrAlY coating and IN738 superalloy

K. V. Dahl and J. Hald

Materials Technology, Dept of Manufacturing Engineering and Management,
Technical University of Denmark, DTU, Lyngby, Denmark.

Abstract

Interdiffusion at the interface between a Co-36.5Ni-17.5Cr-8Al-0.5Y, MCrAlY coating and the underlying IN738 superalloy was studied in a large matrix of specimens isothermally heat treated for up to 12,000 hours at temperatures 875°C, 925°C or 950°C. Modelled results using the finite difference software DICTRA was compared with experimental average composition profiles measured across the interface. The simulated results were able to qualitatively predict the phase-transformations occurring at the interface. The microstructural studies showed that a layer of continuous γ´ was formed on the superalloy side of the interface. This was found in the simulated results as a very high fraction of γ´. In order to treat this correctly a model able to employ more than one matrix phase would be needed. For the present simulations an approximate solution was reached by assuming that diffusion in the γ´-phase is slow compared to diffusion in the γ-matrix.

Introduction

In the gas turbine, hot section components such as blades and vanes are protected against the aggressive high temperature environment by one or several coatings. Two of the major degradation mechanisms are oxidation and hot corrosion. The MCrAlY (M= Ni,Co) type coating provides good protection against these phenomena by forming stable aluminium and chromium oxides at the outer surface. As long as the coating contains enough aluminium and chromium to form these oxides, the structural part of the blade (the underlying superalloy) remains intact. When e.g. the amount of aluminium in the coating becomes low (after long service time) the coating has to be stripped of and a new coating applied.

The life time of the coating therefore depends on the availability of the oxide forming elements. The formation of protective oxides is however not the only mechanism, removing aluminium and chromium from the coating. At the interface between the coating and underlying superalloy, compositional differences can lead to significant loss of the active elements through interdiffusion.

The behaviour at the interface is complex and will depend on the compositions of the specific coating/ superalloy system chosen for the component. Typically phase transformations occur in both coating and superalloy as a result of the interdiffusion. Thermodynamic and kinetic modelling software may help in understanding these transformations and at the same time provide a tool for predicting the behaviour of specific coating/ superalloy combinations. Using the finite difference software DICTRA [1] to solve the diffusion equations, combined with multicomponent diffusion mobility and thermodynamic databases allows us to predict phase fractions and interface behaviour of the many different elements present in commercial superalloys and metallic coatings.

In order to test the accuracy of the modelled results, detailed experimental data needs to be available for comparison. In previous work [2], the interdiffusion behaviour between a Co-36.5Ni-17.5Cr-8Al-0.5Y, MCrAlY coating and the underlying IN738 superalloy was studied. The experimental work revealed that the following phases were present at the interface: γ, β, γ', *MC* and $M_{23}C_6$. Normally when using EDS or WDS methods for composition profiling in multiphase systems there will be a large scatter in the measurements depending on the position of the electron microprobe and whether it "hits" in the γ-matrix or in one of the precipitate-phases, β, γ', *MC* or $M_{23}C_6$. In contrast the compositions calculated by DICTRA will be an average of all the phase compositions. An experimental approach developed in previous work [3] allows for the measurement of true average composition profiles across the interface that can be directly compared to calculated results.

In the previous work a precipitate free zone was found between MCrAlY coating and IN738 substrate and was assumed to grow following a parabolic growth law. This was a simple assumption and even though the fit to the experimental data was good, it was thought by the authors that the simple growth law did not fully describe the processes taking place at the

interface. In the present work the DICTRA software is used to test the basic assumption of parabolic growth and to illustrate the complexity of the interface behaviour.

Material

Microstructural investigations were done for a matrix of isothermally heat treated MCrAlY/ IN738 specimens [2]. Average composition profiles were measured using an approach that is described in [3].

Average compositions of the IN738 specimens and the MCrAlY coating are shown in tables 1 and 2. The MCrAlY coating was applied by low pressure plasma spraying after which, the specimens received a standard two step heat treatment:

1) 1120ºC for 2 hours then air cooled with an average cooling rate of 35ºC/min to 650ºC.
2) 845 ºC for 24 hours then air cooled with an average cooling rate of 20ºC/min to 650ºC.

In the following the as-coated condition refers to specimens having received this initial heat treatment.

Table 1: Average composition of MCrAlY coating.

MCrAlY	Ni	Cr	Al	Y	Co
Mass%	36.5	17.5	8	0.5	bal

Table 2: Average composition of superalloy IN738

IN738	Cr	Co	Al	Ti	W	Ta	Mo	C	Zr	B	Nb	Ni
Mass%	16.0	8.5	3.4	3.4	2.6	1.75	1.75	0.11	0.04	0.01	0.85	bal

Specimens were then isothermally heat treated in air at 925ºC or 950ºC for 250, 500, 1,000, 2,000, 4,000, 8,000 and 12,000 hours or at 875 ºC for 500, 1,000, 2,000, 4,000 and 8,000 hours.

Standard metallographic procedures were used to cut, mount and polish the specimens in cross-section. Specimens were ground and then diamond polished to 1 μm finish. The metallographic specimens were then coated with approximately 50 nm evaporated carbon for observation in a JEOL 5900 scanning electron microscope (SEM) equipped with an INCA 400 EDS system from Oxford Instruments.

The interface between coating and superalloy was studied in cross-section both in polished and etched condition using backscatter contrast.

Microstructural observations

In previous work [2], it was found that diffusion of aluminium from coating into the IN738 substrate resulted in the formation of a precipitate free layer in the interdiffusion zone and the formation of a γ'-rich layer on the superalloy side of the interface.

During the first, high temperature step of the initial heat treatment an interdiffusion zone between the coating and the substrate is formed as aluminium is transported into the substrate. During the second step of the initial heat treatment, fine γ'-particles precipitate in the interdiffusion zone and with time further transport of aluminium into the substrate results in the formation of a precipitate free zone. The previous investigations indicated that this precipitate free zone grew according to a parabolic growth law and this was used to develop a simple model for estimating the metal temperature of components from the width of the zone.

Fig. 1 shows the microstructure at the interface in a specimen isothermally heat treated at 925°C for 250 hours. The precipitate free zone is visible between the bulk coating and a zone with increased volume fraction of γ' on the superalloy side.

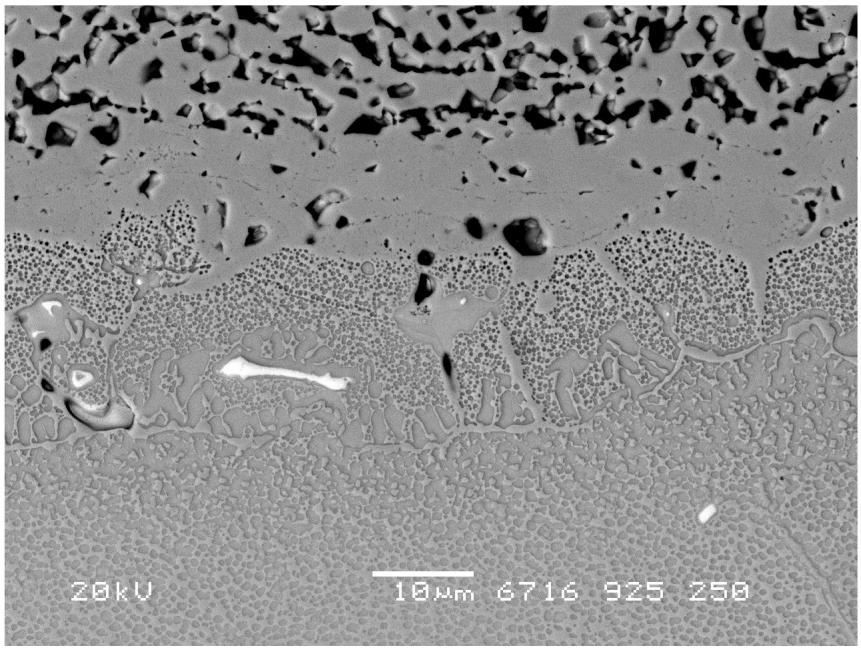

Fig. 1: Interface between coating and substrate for a specimen heat treated for 250 hours at 925°C. The precipitate free zone is visible

For comparison with modelled results average composition profiles across the interface were obtained for all the isothermally heat treated specimens. Fig. 2 shows measured composition profiles for specimens heat treated at 875°C. The behaviour at 925 and 950°C is similar to the behaviour observed at 875°C, except that the precipitate free zone grows faster as a result of the higher temperature.

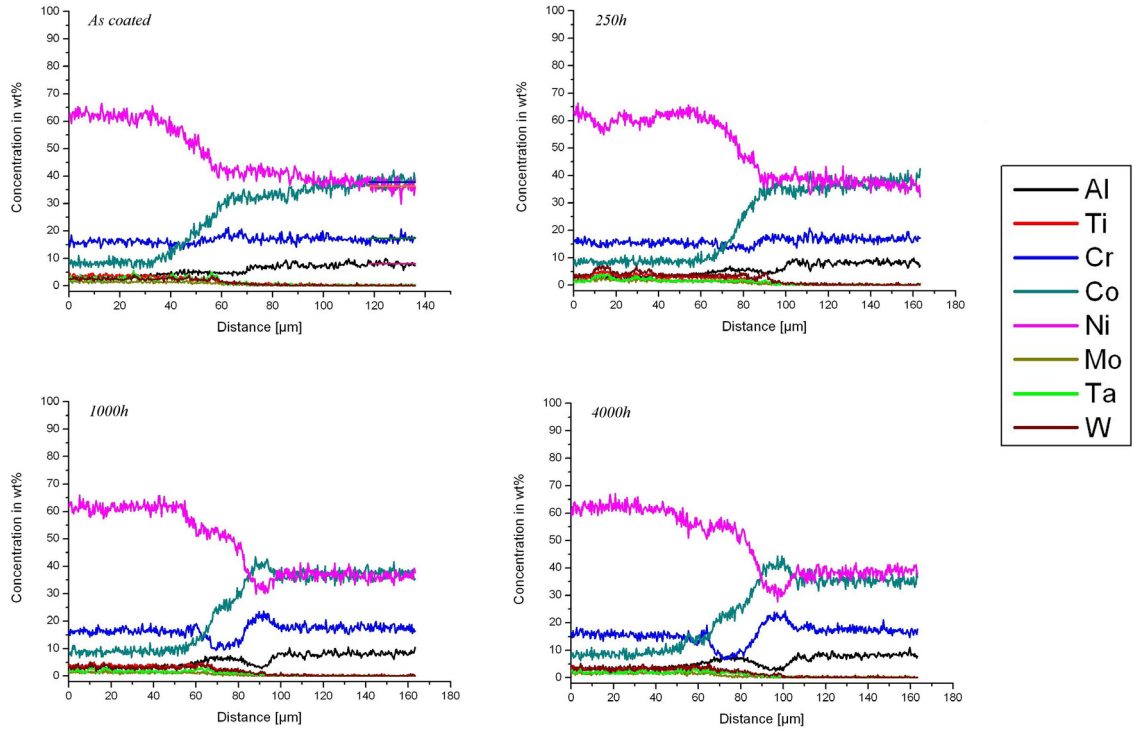

Fig. 2: Measured composition profiles for the as-coated specimen and specimens heat treated at 875°C for 250, 1,000 or 4,000 hours.

From the experimental composition profiles, phase fraction diagrams were calculated using Thermo-Calc. This was done by first applying a smoothening procedure to the measured profiles and then calculating equilibrium phase fractions for each data-point using the Thermo-Calc software. Thermodynamic data was obtained from the nickel-alloy database Ni-data v. 4 by Thermotech Ltd. [4].

Phase-fraction diagrams calculated from the composition profiles in Fig. 2 are shown in Fig. 3. Since the profile for carbon was unknown (can not be measured using EDS), carbon was not included in these calculations. Therefore Cr-rich σ-phase is predicted to appear at the location where Cr-rich $M_{23}C_6$ carbides are found in the actual microstructure (see Fig. 4). The calculated phase fraction diagrams nicely illustrate the formation of the precipitate free zone.

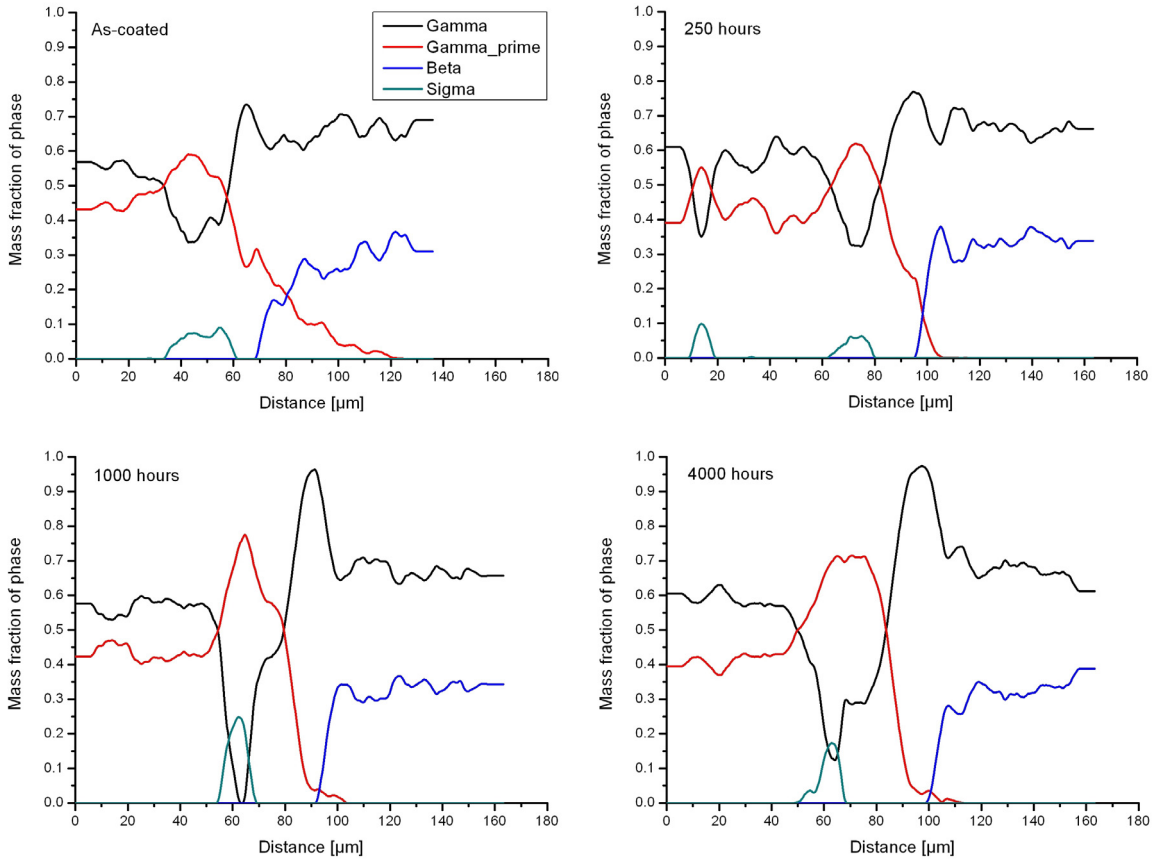

Fig. 3: Phase fraction diagrams calculated from the composition profiles presented in Fig. 2.

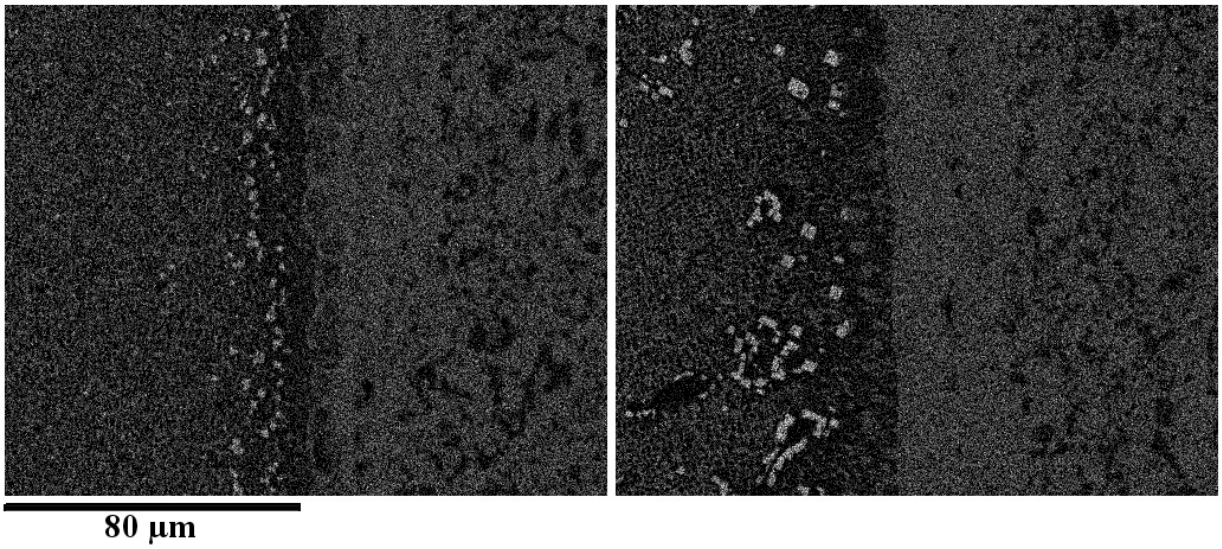

Fig. 4: Cr EDS x-ray maps showing Cr-rich $M_{23}C_6$ carbides on the substrate side of the interface; Left: 8,000h at 875°C. Right: 8,000h at 925°C. [2]

Modelling

Modelling was performed using the DICTRA software from Thermo-Calc AB.

DICTRA employs a finite difference approach to solve flux and conservation equations between node-points. Temperature and concentration dependent diffusion coefficients are obtained from multicomponent thermodynamic factors and diffusion mobilities. Thermodynamic factors are calculated within each time step in the Thermo-Calc software that also calculates phase fractions in each node point based on the chemical composition in the node-point. The phase fractions are therefore calculated under the assumption of local equilibrium. Thermodynamic data was obtained from the nickel-alloy database Ni-data by Thermotech [4]. Kinetic mobilities were obtained from work by Campbell et al. [5].

In the DICTRA software the atomic mobility coefficient, M_B of an element B is described by an expression derived from absolute-reaction rate theory:

$$M_B = M_B^{\circ} \exp\left(\frac{-Q_B}{RT}\right)\frac{1}{RT}$$

where the mobility coefficient is divided up into an activation enthalpy Q_B and a frequency factor M_B°. Both the activation enthalpy and the frequency factor will in general depend upon composition, temperature and pressure. The composition dependency is represented with a linear combination of the values at each endpoint in composition space and a Redlich-Kister expansion, in spirit with the Calphad approach [6]:

$$\Phi_B = \sum_i x_i \Phi_B^i + \sum_i \sum_{J>i} x_i x_j \left[\sum_{r=0}^{m} {}^r\Phi_B^{i,j}(x_i - x_j)^r\right]$$

where Φ_B represents the composition dependent parameter, Φ_B^i is the value of Φ_B for pure i, ${}^r\Phi_B^{i,j}$ are binary interaction parameters where the comma separates different species interacting with each other, and x_i is the mole fraction of element i. [7]

The atomic mobility coefficient can be related to the tracer diffusion coefficient by

$$D_B^* = RTM_B$$

The chemical diffusivity is given by a more complex expression where the concentration of one element has been chosen to be dependent on the others. The reduced chemical diffusivity is given by [8]

$$D_{kj}^n = \sum_i (\delta_{ik} - x_k) x_i M_i \left(\frac{\partial \mu_i}{\partial x_i} - \frac{\partial \mu_i}{\partial x_n} \right)$$

where *n*, *k* and *j* are the dependent, the diffusing and the gradient element, respectively, δ_{ik} is the Kronecker delta ($\delta_{ik} = 1$ if *i*=*k* and $\delta_{ik} = 0$ otherwise), x_k is the mole fraction of element *k* and μ_i is the chemical potential of element *i*.

Initial concentration profiles were entered using an error function expression as shown below:

$$c_1 + \frac{(c_2 - c_1)}{2} \left[1 + erf\left(\frac{x - x_i}{s} \right) \right]$$

where c_1 and c_2 are the initial concentrations on different sides of the interface, x is the position on the x-axis, x_i is the position of the interface (typically in the centre of the calculation region) and s is a constant used to adjust the smoothness of the transition between the two concentrations in the vicinity of the interface.

The average specified compositions from Table 1 and Table 2 were entered as start values. The actual composition of the specimens may deviate somewhat from the average specified composition. The purpose with the current work is however to use DICTRA as a predictive tool for the behaviour of coated gas turbine components and for such components typically only the specified compositions are available.

Diffusion calculations were done considering the elements *Al*, *Ti*, *Cr*, *Co*, *Ni*, *Mo*, *Ta, W and C*. Phases considered in the calculation were γ-fcc, γ', β, σ, bcc, MC and $M_{23}C_6$.

There is one consideration that should be mentioned concerning the inclusion of carbon in the calculations. During the initial high temperature heat treatment the $M_{23}C_6$ Cr-rich carbides are not thermodynamically stable and carbon is instead found in Ti-Ta rich primary carbides.

These primary carbides are not thermodynamically stable at the three isothermal heat treatment temperatures (875, 925 and 950ºC), and in the calculations carbon will therefore immediately be "free" to form $M_{23}C_6$ carbides. In the actual microstructure, the primary carbides are only very slowly dissolved, thus limiting the amount of "free" carbon available to form $M_{23}C_6$ carbides.

The simulation

The initial heat treatment was incorporated as part of the interdiffusion calculation as shown in Fig. 5. After the initial heat treatment the isothermal heat treatments at 875, 925 and 950ºC were simulated.

The time step was chosen to fit the experimental details; a short time step was used for the initial high temperature treatment and during simulation of the cooling procedures, while a larger time step could be used when the temperature was held constant during the final isothermal heat treatments.

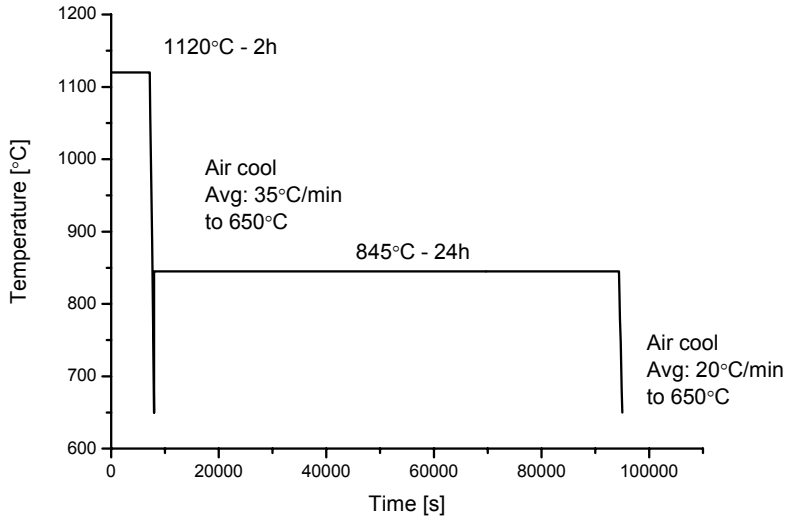

Fig. 5: Initial heat treatment after the plasma spraying.

In the calculations the total region was 650 μm wide with the interface between coating and superalloy located at x = 150 μm. The coating region was assumed to be 150 μm wide, which is half the thickness of the original coating. This was entered as a first approximation since aluminium will not only be depleted by interdiffusion but also by oxidation at the surface. Using 150 μm as the size of the region in the calculations therefore corresponds to assuming that depletion of aluminium occurs at the same rate for the two mechanisms.

The standard DICTRA model developed by Engström et al. [**9**] is a so-called disperse phase model that only takes into consideration diffusion in the matrix phase while particles are handled as non-diffusion phases. The model therefore assumes that the γ-phase is a continuous phase and that diffusion only takes place in this phase. The other phases present are implemented as dispersed phases that act as point sinks or sources for solute atoms as the fraction of the phases grow or shrink in response to the simulated composition in specific node-points.

This means that all other phases than the continuous matrix phase are considered as obstacles for the diffusion in the calculations. This is implemented by multiplying the diffusion parameters for the pure matrix phase with a resistance parameter also called a labyrinth factor that is a function of the volume-fraction of particles.

Concerning the diffusion, the system is thus approximated as a two-phase system consisting of matrix and particles. All particles are assumed to have the same influence on the diffusion, neglecting differences due to different crystal structures of different particles etc. For the present case we have β-particles on the coating side of the interface and γ'-particles on the substrate side of the interface. These different particles may in reality have a different influence on the diffusion but in the calculations they are assumed to slow down the diffusion in the exact same way, only depending on volume fraction. This treatment also means that for instance the influence of coarsening of particles is not taken into consideration in the calculations.
These limitations may seem severe, one of the purposes of the current work was however to find a tool to predict the behaviour at the interface without using excessive computation time so that the model would be directly applicable to practical cases from the industry. With more complicated models it would probably be necessary to do calculations with a reduced system (fewer elements) in order to keep the simulations within a reasonable time-frame, which means it may be hard to apply the models directly to service exposed components where the complex phase-transformations and precipitations taking place are an effect of all the elements present.

A common choice for the labyrinth factor is simplified versions of the bounds derived by Hashin and Shtrikman [10]. Hashin and Shtrikman used variational methods to derive upper and lower bounds for the effective magnetic permeability of macroscopically homogenous

and isotropic multiphase materials. The bounds are also applicable to diffusion and have been used by Engström et al. [11] and Gómez-Acebo et al. [12].

Under the assumption that $D_\gamma > D_{particles}$ the following expression for upper and lower bounds for the effective diffusivity can be applied:

$$D_{eff}^{upper} = D_\gamma + \frac{f_{particles}}{\frac{1}{D_{particles} - D_\gamma} + \frac{f_\gamma}{3D_\gamma}}$$

$$D_{eff}^{lower} = D_{particles} + \frac{f_\gamma}{\frac{1}{D_\gamma - D_{particles}} + \frac{f_{particles}}{3D_{particles}}}$$

When $D_\gamma >> D_{particles}$ and $f_\gamma > f_{particles}$ then the upper bound can be simplified to:

$$D_{eff}^{upper} = D_\gamma \left(\frac{2f_\gamma}{3 - f_\gamma} \right)$$

This last expression was used by Gomez-Acebo et al. [12] in their calculations and is equivalent to the expression derived by Raleigh [13] for the influence of spherical particles.

In the present calculations the volume-fraction of γ' reaches a very high value at the interface between coating and superalloy because of diffusion of aluminium into the substrate. During the initial heat treatment the presence of σ-phase, β-phase and the high volume fraction of γ' causes the volume fraction of γ-fcc to go to almost zero at the interface. If the *Raleigh* expression is used, the labyrinth factor will then be close to zero, causing the diffusion to stop entirely, which is not consistent with the experimental data.

Therefore a different expression for the labyrinth factor had to be used. In the actual microstructure, when the γ-fraction goes to zero, the effective diffusion at the interface will depend on the diffusion parameters of the γ'-phase. These parameters are not accessible in the DICTRA disperse phase model, where only diffusion in the γ-fcc is treated; it does however seem safe to assume that diffusion in the γ'-phase will be significantly slower than diffusion in γ-fcc, because of the ordered crystal structure of γ'.

Therefore as a first approximation a labyrinth factor was used where it was assumed that when the volume fraction of γ-fcc approached zero, the diffusivity would be approximately an order of magnitude slower than in the γ-fcc ($D_{particles} = 0.1 D_{\gamma}$). Inserting this expression into the above equations, leads to the following expressions, where the term in brackets can be used as labyrinth factor in the calculations:

$$D_{eff}^{upper} = D_{\gamma}\left(1 + \frac{3 - 3f_{\gamma}}{f_{\gamma} - \frac{10}{3}}\right)$$

$$D_{eff}^{lower} = D_{\gamma}\left(0.1 + \frac{0.9 f_{\gamma}}{4 - 3f_{\gamma}}\right)$$

In the present calculations the expression for the upper bound is used. It must however be emphasized that the used expression is an upper bound for a two-phase system where the diffusivity in the particle-phases is one tenth of the diffusivity in the matrix phase, it is not an upper bound for diffusion in the actual system. In order to employ the correct expressions for the system a model that could directly take the diffusion inside the precipitate phases into account would be needed.

Results of simulations

Modelling was performed for the initial heat treatment and it was found that at the start of the simulation the thermodynamics predicted the formation of γ′ in the interface almost immediately, which results in a large volume fraction of γ′ to be predicted in a single node-point. This was inconsistent with the available experimental data, and therefore γ′ was suspended from the calculations during the high temperature part of the initial heat treatment (the first two hours at 1120ºC). In the actual interface microstructure it will take some time for the γ′ to nucleate and grow and the only way to implement this in the calculation is not to allow the γ' to form immediately. During the following cooling, γ' was then taken into the calculation and allowed to form.

Fig. 6 presents modelled and measured composition profiles after the initial two-step heat treatment (as-coated condition), for 4,000 hours at 875, 925 and 950ºC. A good fit is obtained and the correct behaviour is observed for all elements.

In the DICTRA software, the calculated profiles can be directly converted into phase fraction diagrams. From the experimental composition profiles, phase fraction profiles can be calculated in Thermo-Calc by performing equilibrium calculations for the composition in each data-point along the profiles as was shown in Fig. 4. This allows for comparison of phase-fractions calculated from the experimental profiles and phase-fractions calculated from the DICTRA profiles. This is presented in Fig. 7, where the solid lines are calculated from the experimental data while the dotted lines are phase fractions predicted by DICTRA.

Overall, there is a nice consistency between simulated and the experimental results. The modelled results are able to predict the formation of the precipitate free layer between coating and substrate, formation of the zone enriched in γ', and also the increased volume fraction of secondary carbides seen in Fig. 4. Qualitatively the modelled results are therefore able to predict the interface behaviour in terms of correct trends in both composition profiles and phase-fraction diagrams.

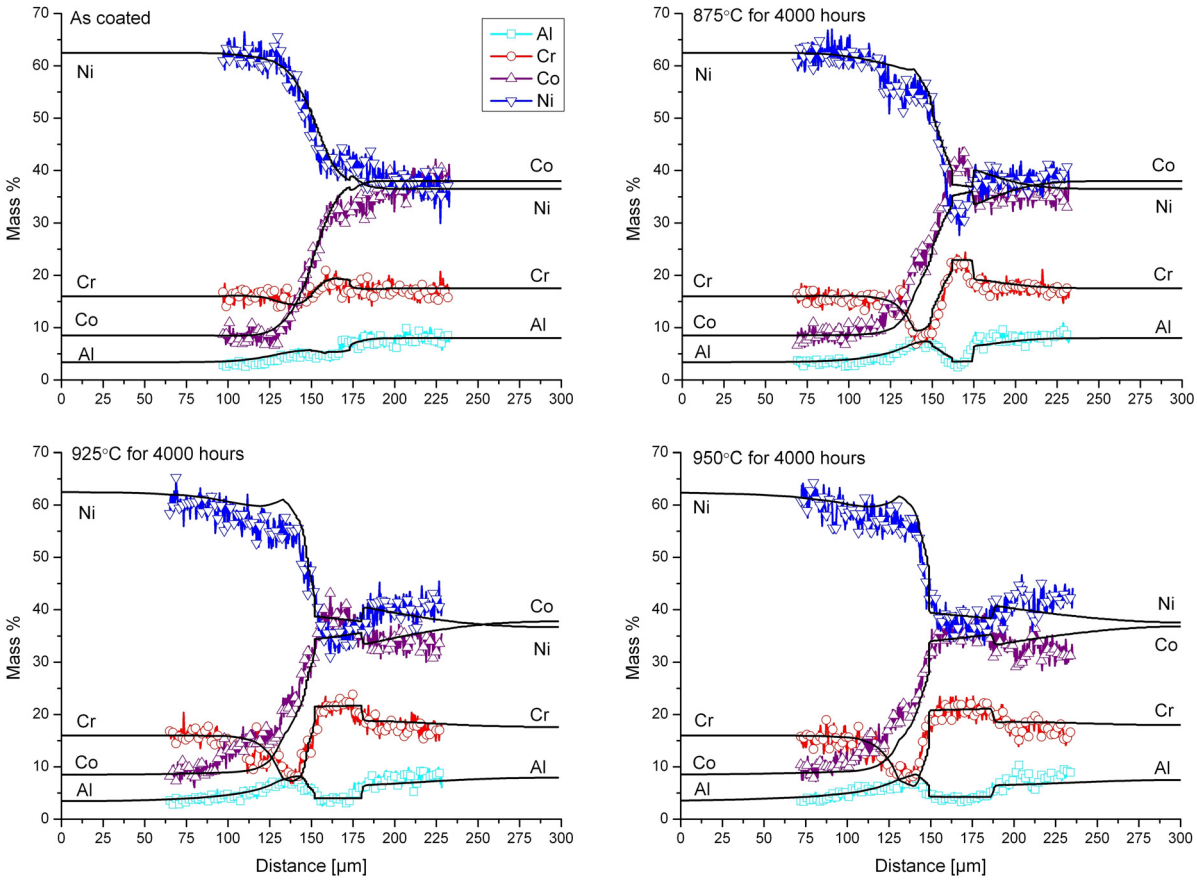

Fig. 6: Measured and modelled composition profiles for major elements across the interface.

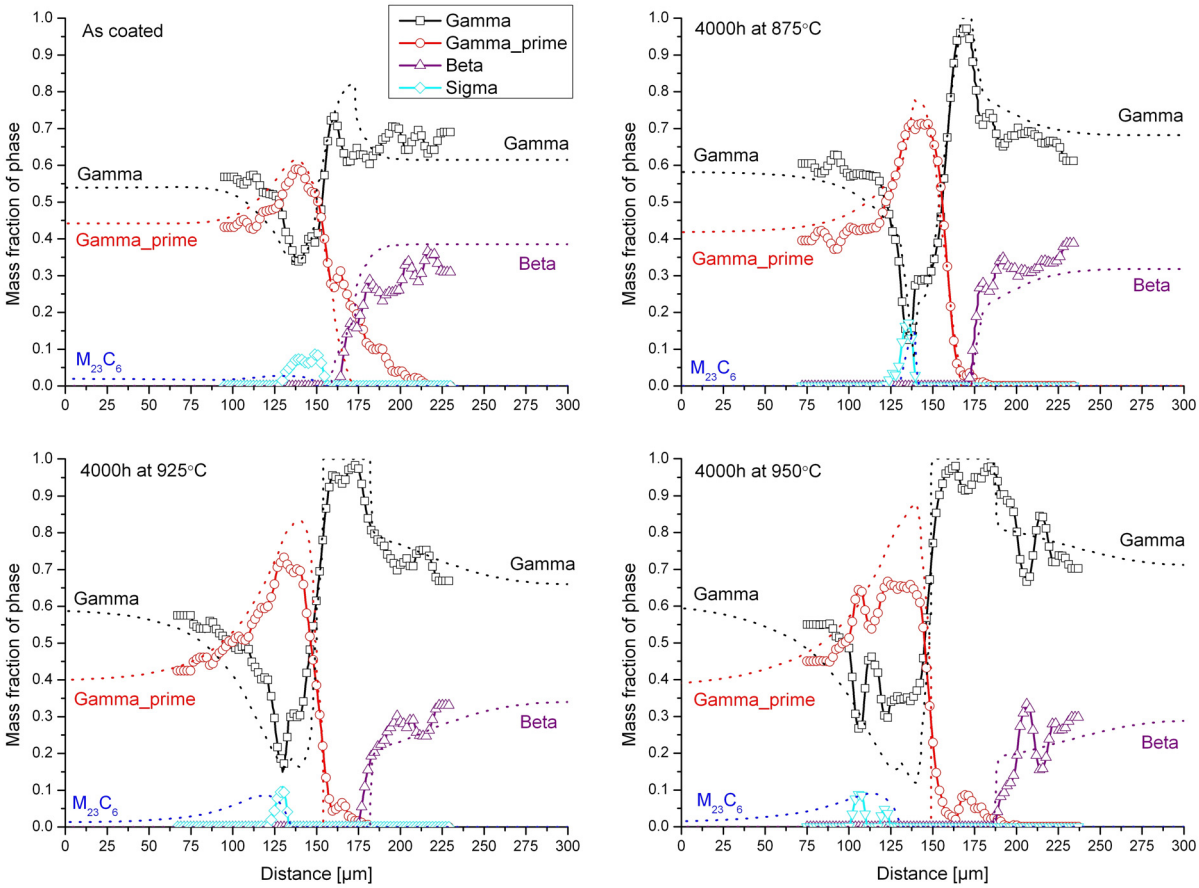

Fig. 7: Phase fraction diagrams; solid lines are calculated from the measured composition profiles and dotted lines are calculated from the modelled composition profiles.

The width of the precipitate free zone was measured experimentally in previous work [2] and can now be compared with values obtained from the modelling using DICTRA. The experimental values were measured from composition/ intensity profiles. The modelled width was measured as the distance between the node-points where the γ'-fraction goes to zero and where the β-fraction goes to zero. The experimental and modelled layer widths are shown in Fig. 8.

The simulated results were strongly dependent on the maximum time step used in the simulations; therefore the simulations had to be run with a low maximum time-step, and the final simulation of each temperature series have taken approximately a week of effective calculation time to finish. The reason for the time step dependency is that within each diffusion step an over-saturation of the matrix phase occurs and if the over-saturation is allowed to become too large (large time step) it will affect the simulated results.

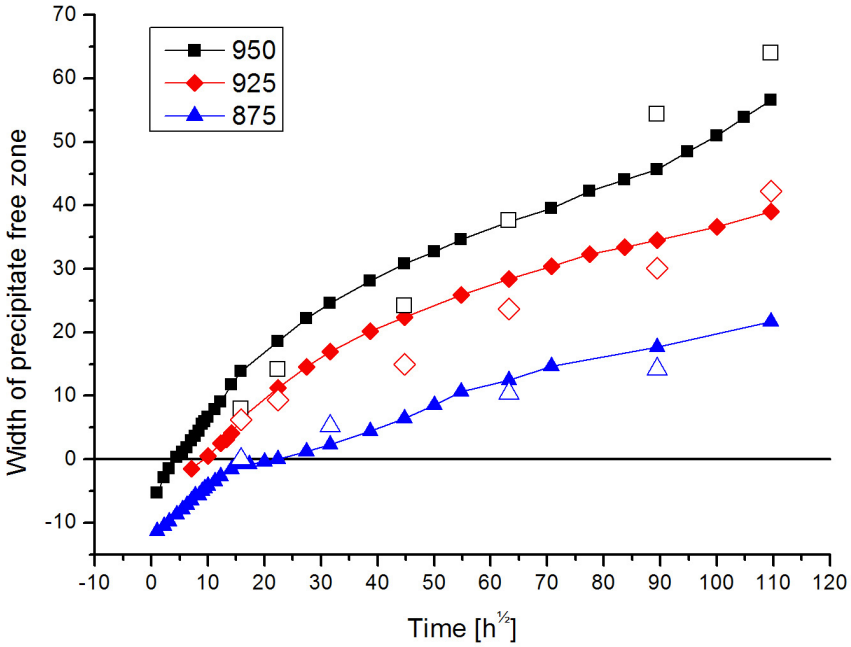

Fig. 8: Measured and modelled widths of the precipitate free zone formed between coating and superalloy.

The fit to the experimentally measured layer widths is quite good, which is in fact a bit surprising since the result is obtained without any input of the true diffusion parameters for the γ′-phase that reaches a high volume fraction at the interface. The reason for the nice fit is probably that diffusion in the γ′-phase is very slow compared to γ-fcc and therefore it works as an effective block for diffusion both in the actual microstructure and in the simulations.

Initially a fast growth of the precipitate free zone is predicted, followed by a slower growth rate where the limiting parameter is diffusion across the γ'-layer at the interface. In order to simulate this accurately it will be necessary to implement the true diffusion parameters of γ' into the calculations. For the present simulations the growth rate in this region is directly given by the choice of labyrinth factor and therefore the choice of diffusion parameters for the γ'-phase.

For the long heat treatment times at 950ºC the growth rate of the precipitate free zone is predicted to increase again. The coating can no longer be considered as semi-infinite, resulting in a faster retraction of the β-phase. This is clearly visible in Fig. 9 where the movement of the "interfaces" is plotted and in the plot of β-phase retraction shown in Fig. 10.

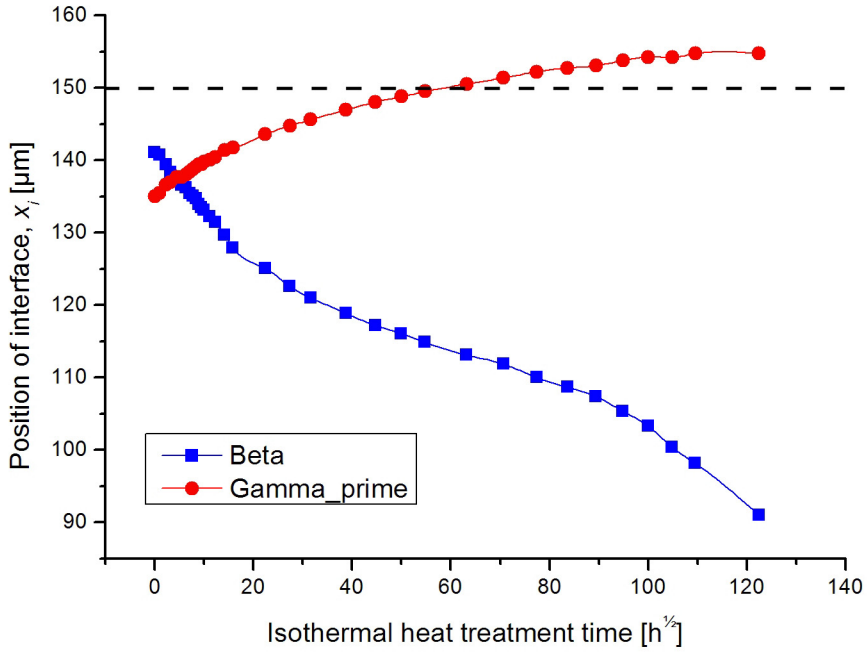

Fig. 9: Positions in the geometry where the β and the γ′-particles start to appear for the simulation at 950ºC. The surface is located at x=0 and the original position of the interface between coating and superalloy (before the initial heat treatments) is indicated by the dashed line at x=150.

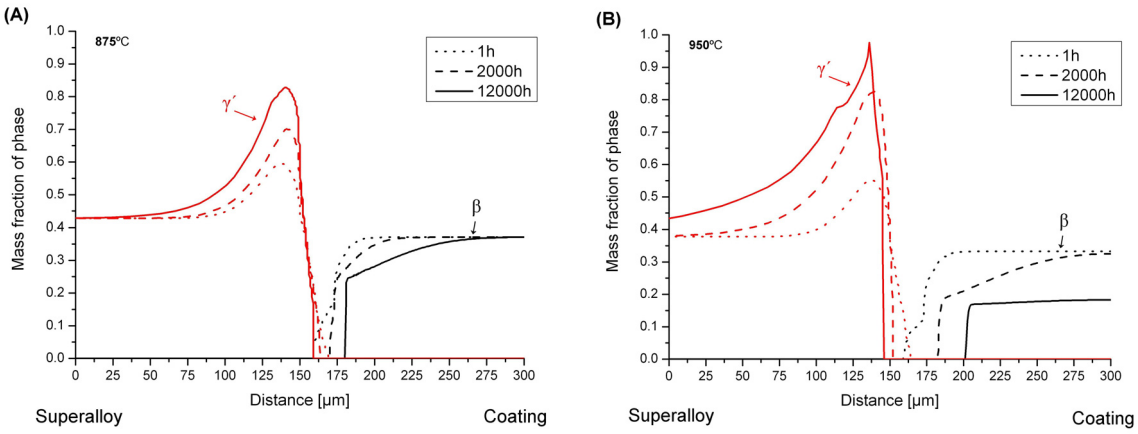

Fig. 10: Simulated *β*- and γ′-phase behaviour at 875 (A) and 950ºC (B); profiles are plotted for 1, 2,000 and 12,000 hours of isothermal heat treatment.

Microstructural study of the specimen heat treated for 12,000 hours at 950ºC revealed that the coating had been almost totally depleted of *β*-phase. It may therefore be speculated that the nice fit of the simple parabolic growth law observed in previous work by the authors may be a result of an increased *β*-retraction after long heat treatment times because of the overall depletion of *β*-phase in the coating. If this is true, parabolic growth may not be observed for thicker coatings.

The DICTRA model assumes that the γ-fcc phase is the continuous matrix phase at all locations but the microstructure investigations indicate that the γ′-phase becomes the continuous phase at the interface as can be seen in Fig. 11. In order to model this correctly a model allowing for more than one matrix phase to be present in the calculations would have to be used, but this is left for future work.

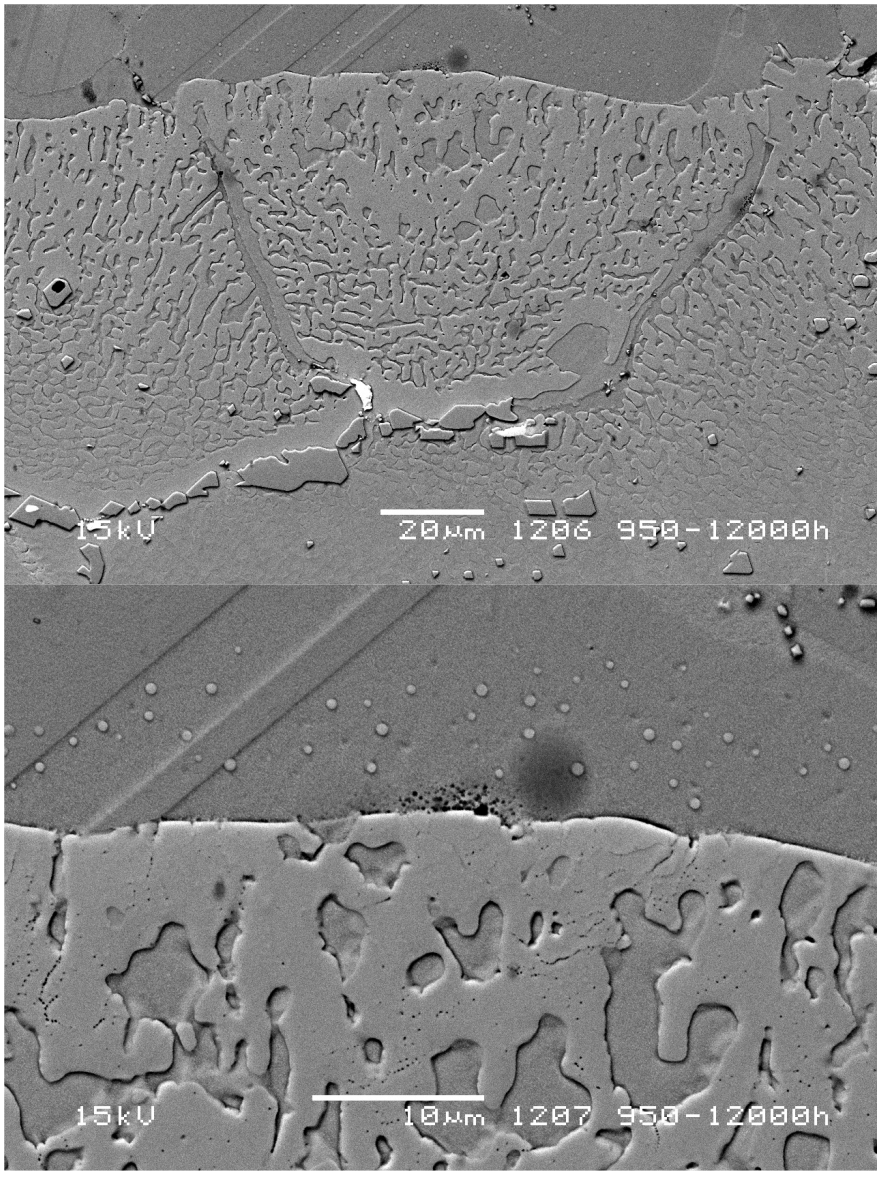

Fig. 11: SEM BSE images at different magnifications of the γ′-enriched zone at the interface after isothermal heat treatment at 950ºC for 12,000 hours. The precipitate free zone is visible at the top of the micrographs. The large bulky particles in the upper image are $M_{23}C_6$ carbides; the Ti-Ta rich primary carbides that appear white in the image have almost been totally dissolved.

Discussion

Normally the DICTRA disperse phase model can only be used when the volume fractions of the dispersed phases are low compared to the matrix phase. In this specific case it goes well, since diffusion in the γ'-phase is low compared to diffusion in the matrix γ-fcc. The γ' therefore works as an effective block for diffusion both in the actual microstructure and in the calculations.

The modelled results are able to qualitatively describe the complex transformations occurring at the interface and to predict both the presence of the increased γ'- and $M_{23}C_6$ fractions at the interface. The growth of a precipitate free zone between the coating and the IN738 superalloy is also correctly predicted.

The width of the growing precipitate free layer is of the same approximate size as that measured experimentally. In order to draw absolute conclusions from the simulated results it would however be necessary to employ a model able to take into account diffusion in the precipitate phases.

In the calculations it was assumed that the coating region was of a finite thickness (150 μm) and that the β-depletion in this region only occurred because of interdiffusion with the underlying substrate superalloy. In the actual system the depletion may occur both due to interdiffusion and due to oxidation from the surface. Since the growth rate of the precipitate free zone was found to increase for the long simulation times at 950ºC, the boundary condition becomes critical and it is therefore necessary to implement the depletion caused by oxidation.

Conclusion

The complex interface behaviour between a Co-36.5Ni-17.5Cr-8Al-0.5Y, MCrAlY coating and the underlying IN738 superalloy was modelled using the finite difference software DICTRA.

The modelling was able to qualitatively describe phase transformations occurring at the interface as a result of the interdiffusion between coating and superalloy. Simulations predicted that the interdiffusion resulted in the formation of a precipitate free zone, a γ'-rich

layer next to the superalloy and precipitation of secondary carbides on the superalloy side of the interdiffusion zone. These features were confirmed by microstructural investigations of isothermally exposed specimens.

The width of the precipitate free zone formed between the coating and the superalloy were of the same size in the experiments and the simulations. A more sophisticated model able to take into account diffusion in the precipitate phases would be needed to precisely describe the interdiffusion.

Acknowledgements

The present research was carried out under the research consortium IMPRESS and is also a part of the European COST 538 action: *High Temperature Plant Lifetime Extension*.

The authors wish to acknowledge the financial support from Energy E2 A/S and the Danish Research Agency (Grant no. 26-03-0275), and also wish to thank ERA Technology for providing heat treated specimens making this investigation possible.

Useful discussions with Henrik Larsson from the Department of Materials Science and Engineering at the Royal Institute of Technology in Stockholm are gratefully acknowledged.

References

[1] A. Borgenstam, A. Engström, L. Höglund and J. Ågren: *Journal of Phase Equilibria*, 2000, **21**, 3, 269-280.
[2] K. V. Dahl and J. Hald: Accepted by *Energy Materials,* 26/01/2006.
[3] K. V. Dahl, J. Hald and A. Horsewell: Material submitted to *Journal of Microscopy*.
[4] N. Saunders, *SUPERALLOYS 1996 - Procedings of the Eight International Symposium on Superalloys*, Champion, Pennsylvania, 1996, 101-110. Edited by R. D. Kissinger et al.
[5] W. J. Boettinger, U. R. Kattner and C. E. Campbell: *Acta Materialia*, 2002, **50**, 775-792.
[6] J. Ågren: *Current Opinion in Solid State & Materials Science*, 1996, **1**, 355-360.
[7] DICTRA User´s guide Version 23 by Thermo-Calc software: http://www.thermocalc.se/Download/Man_ex_Dictra.html
[8] B. Jönsson: *ISIJ International*, 1995, 35 (11), 1415-1421.
[9] A. Engström, L. Höglund and J. Ågren: *Metallurgical and Materials Transactions A*, 1994, **25A**, 1127-1134.
[10] Z. Hashin and S. Shtrikman: *Journal of Applied Physics*, 1962, **33**, 10, 3125-3131.
[11] A. Engström: *Scandinavian Jorunal of Metallurgy*, 1995, **24**, 12-20.
[12] T. Gómez-Acebo, B. Navarcorena and F. Castro: *Journal of Phase Equilibria and Diffusion*, 2004, **25**, 3, 237-251.
[13] L. Raleigh: *Philosophical Magazine,* 1892, **34**, 481-502.

Appendix IV

Negative creep in nickel base superalloys

Conference paper presented at:

BALTICA VI

Life Management and Maintenance for Power Plants

Helsinki-Stockholm-Helsinki
8-10 June, 2004

Negative creep in nickel base superalloys

Kristian V. Dahl, TU Denmark, Lyngby
John Hald, Elsam/Energy E2/TU Denmark, Lyngby

Abstract

Negative creep describes the time dependent contraction of a material as opposed to the elongation seen for a material experiencing normal creep behavior. Negative creep occurs because of solid state transformations that results in lattice contractions.

For most applications negative creep will have no practical implications but under certain conditions it may become critical. For bolts and fasteners, which are highly constrained during service, negative creep may lead to dramatically increased stresses and eventually to failure.

The article was inspired by a recent failure of Nimonic 80A bolts in German gas turbines. As a result of this failure similar bolts from Danish gas turbines of the same type were investigated and it was found that the bolts had experienced negative creep during service.

1. Introduction

At elevated temperatures metallic materials may undergo solid-state reactions as a result of microstructural instability. These reactions are frequently accompanied by density changes, e.g. precipitation from solid-state can promote an expansion or contraction in alloys. In some cases, length changes may be observed at zero applied stress or an alloy may exhibit a contraction in spite of an applied tensile stress. The term “negative creep” is used to describe a time-dependent contraction of a material rather than the extension normally seen during creep tests.

If a microstructural transformation occurs during a creep test then the observed creep curve will be a sum of two contributions, one from normal creep and one from length changes due to the transformation. Figure 1 shows a series of schematic diagrams of different material behaviour during creep tests and stress relaxation tests for a material that contracts during the testing because of a microstructural transformation.

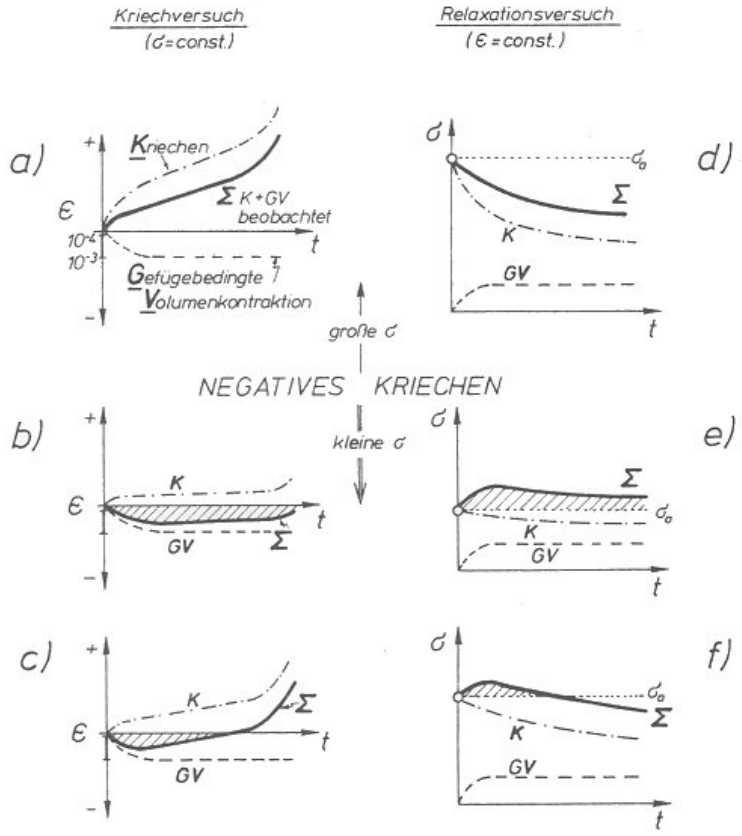

Figure 1. Schematic drawings of negative creep behaviour (hatched areas). Normal creep behaviour (K) and volume contraction due to a solid-state transformation (GV) for normal creep tests (a to c) and for stress relaxation tests (d to f). [1]

At high stresses normal creep behaviour (K) will dominate and the contribution from the microstructural transformation (GV) will be concealed within the sum curve (∑) (pictures a) and d) in Figure 1). At low stresses the contribution from the microstructural transformation may dominate and negative creep behaviour may be observed (pictures b) and e) in Figure 1). During creep tests a solid-state transformation may result in sample contraction in spite of the applied tensile stress and during stress relaxation tests there will be an increase in stresses in order to maintain the imposed constant strain. Pictures c) and d) in Figure 1 show a mixed behaviour, where negative creep is observed after short times, while normal creep behaviour dominates after long times.

A quantitative treatment of the negative creep phenomenon is complicated because of the interaction between the two opposing processes. The plastic strain may accelerate the progress of the solid state reaction, while the resistance to plastic flow is dependent on the structural changes produced by the metallurgical reaction. [1]

For most applications the density changes introduced by a microstructural transformation will have no practical implications but under certain conditions it may become critical. For bolts and fasteners a situation close to that of the constant strain stress-relaxation tests can arise during service.

Negative creep can occur in many different alloys. The first observations of negative creep were done by Fountain and Korchinsky [2] in 1959 during their work on iron-molybdenum and iron-tungsten alloys. In later work negative creep behaviour has been found for several different Ni-based superalloys and can be connected with solid state transformations such as the precipitation of carbides or order-disorder transformations. For superalloys that often contain numerous different alloying elements, long time exposure at elevated temperatures results in microstructural evolution and it has in fact been found that negative creep behaviour is more the rule than the exception. Kloos, Granacher and Bartsch found negative creep behaviour for the alloys IN713C, IN738LC and IN939 [3] (see Figure 2), and similar behaviour was found for Waspaloy [1]. The most comprehensive investigations on negative creep have been done for the alloy Nimonic 80A [4, 5, 6, 7, 8, 9], where lattice contraction occurs due to an ordering transformation.

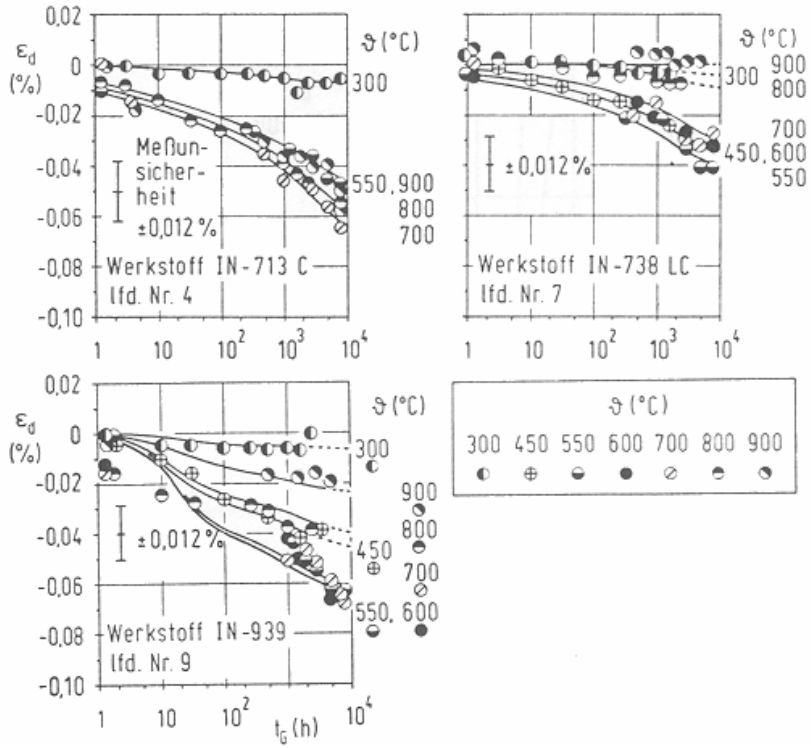

Figure 2. Density dependent strain due to structure induced density changes, measured in annealing tests [3].

2. Nimonic 80A

Nimonic 80A is a widely used superalloy, e.g. for bolting material, and is widely treated in the literature. Nimonic 80A was introduced as a turbine blade alloy already in 1944 and was adopted as a bolting material for steam turbines in the mid 1960s for operating metal temperatures of 370–570ºC. The nominal composition of Nimonic 80A is shown in Table 1.

Table 1. Composition of Nimonic 80A (weight percent).

C	**Si**	**Cu**	**Fe**	**Mn**	**Cr**	**Ti**	**Al**	**Co**	**Mo**	**B**	**Zr**	**Ni**
0.04	1.0	0.2	1.0	1.0	18.0	1.8	1.0	2.0	0.3	0.0015	0.04	bal
0.10	max	max	max	max	21.0	2.7	1.8	max	max	0.005	0.10	

Failures of Nimonic 80A steam turbine bolts have been relatively infrequent. Approximately 0.4% of the bolts in service have failed much earlier than the expected stress rupture life [9]. Nimonic 80A does not normally experience creep in the temperature regime up to 600ºC and when failed bolts were investigated it was found that instead of normal creep extension the bolts had contracted during service.

Stress relaxation testing and subsequent metallurgical investigation [4, 5] revealed that this unusual behaviour was due to an ordering transformation. Formation of the Ni_2Cr ordered phase resulted in a general lattice contraction and gave rise to negative creep.

Out of ~10,000 steam turbine bolts manufactured by Parsons Power Generation Systems 75 failures have been recorded and 34 of these were found to be a result of overload when ordering increased the stress levels in the bolts. For these bolts an initial overtightening combined with the lattice contraction caused the failure [6]. Usually the failure occurs as a brittle intergranular fracture [7].

2.1 Ordering of Ni-Cr matrix phase in Ni-based superalloys

Superalloys are normally strengthened by precipitation of the ordered γ′-phase (Ni_3Al) which has a very high resistance against coarsening, but at very long exposure times and rather low temperatures ordering of the otherwise disordered γ FCC matrix (Ni and Cr) can also take place.

The degree of ordering has a maximum when the Ni:Cr ratio of a given material corresponds to the stoichiometric composition of the ordered phase (Ni_2Cr). When the composition deviates from the ideal ratio (2:1) the kinetics of the ordering reaction become sluggish (formation is delayed) and ordering only appears after several thousands of hours of aging [10].

The unit cell of the Ni_2Cr phase is orthorhombic. The orientation relationship between the ordered phase and the fcc matrix is shown in Figure 3.

The presence of the ordered phase in a given sample can be established by electron diffraction in a transmission electron microscope. The superlattice reflections marked 1 and 2 in Figure 4 clearly indicates the presence of the Ni_2Cr ordered phase.

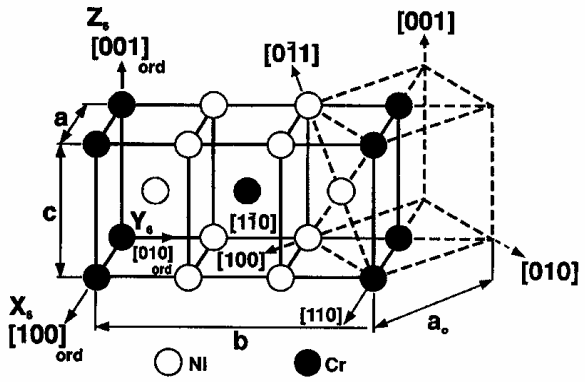

Figure 3. Ordered structure of Ni_2Cr. The broken lines refer to the original fcc unit cell [1].

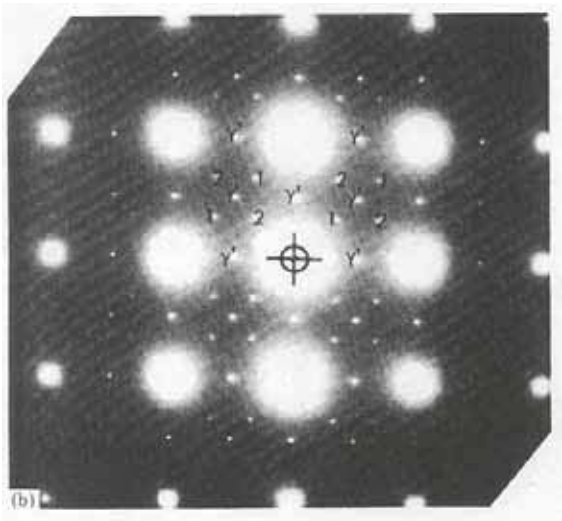

Figure 4. Diffraction pattern from Nimonic 80A thin foil containing the ordered Ni_2Cr phase [4].

For the Nimonic 80A alloy the ordering transformation introduces a general lattice contraction of approximately 0.1%, which can produce an increase in stress [4] and therefore can result in negative creep. Figures 5 and 6 show the stress relaxation behaviour of Nimonic 80A during a constant-strain stress relaxation test at different temperatures.

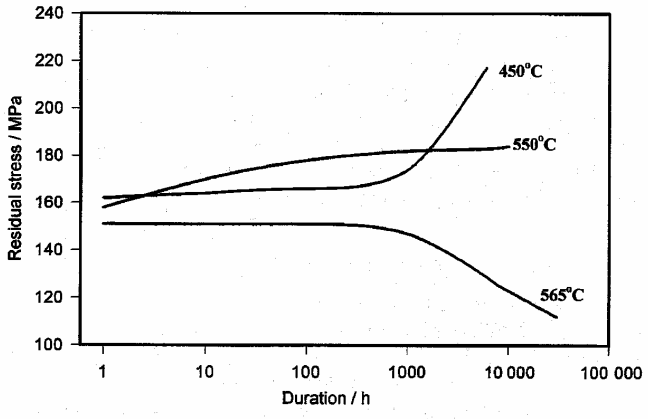

Figure 5. Stress Relaxation of Nimonic 80A at a constant strain of 0.1% [11].

At temperatures above 550ºC Nimonic 80A exhibits normal stress relaxation behaviour in that the stress decreases with increasing test duration (Figure 5 and 6). Below 550ºC the contraction due to the ordering transformation becomes the dominant factor, and negative creep behaviour is observed.

The ordering transformation does not occur immediately due to sluggish kinetics because of deviation of the Ni-Cr matrix composition from the ideal 2:1 Ni:Cr ratio. The larger the deviation the more sluggish the kinetics become. This has been shown by Marucco in investigations on Ni-Cr-Fe alloys with varying composition [12].

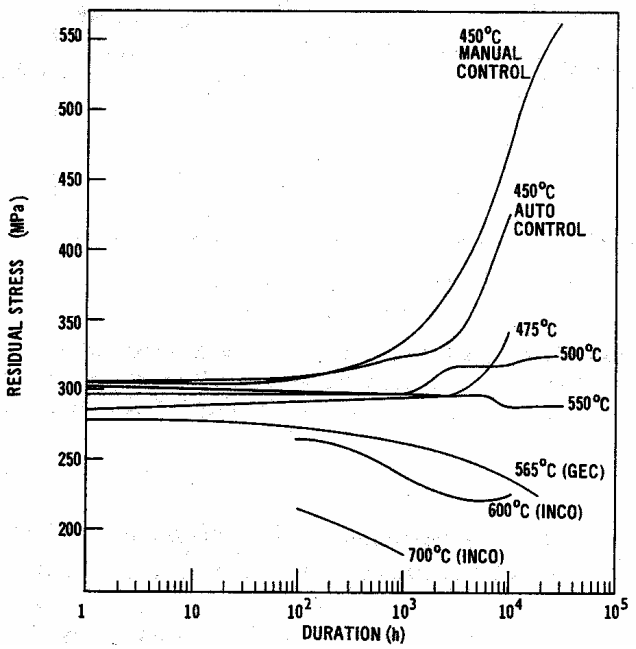

Figure 6. Stress relaxation of Nimonic 80A at a constant strain of 0.15% [4].

Total lattice contractions of up to 0.16% have been reported for a service time of 50,000 h [6].

The ordering transformation has also been reported to result in an embrittlement of the bolting material. In failed bolts a lower charpy impact value and a higher microhardness value compared to virgin stock have been found [7]. However there is some doubt whether this effect is caused by the ordering transformation or by segregation of phosphorous to grain boundaries. [13]

3. Analysis of bolt specimens

In German gas turbines two failures of Nimonic 80A bolts used for fixation of IN939 heat shields in the hot gas ducts of the turbines have recently been reported. The failure mechanism appeared to be creep and the failure occurred at a notch right below the bolt heads.

Three bolts originating from Danish gas turbines of similar type in Hilleroed and Svanemoellen were studied at the Materials department (IPL-MPT) at the Technical University of Denmark in order to establish if these bolts had indications of creep failure. Figure 7 shows the setup used in the gas turbines.

The estimated temperature of the bolt heads is 500−550°C. The lower part of the bolts is expected to be cooler than the bolt heads due to the flow of cooling air coming from the bottom.

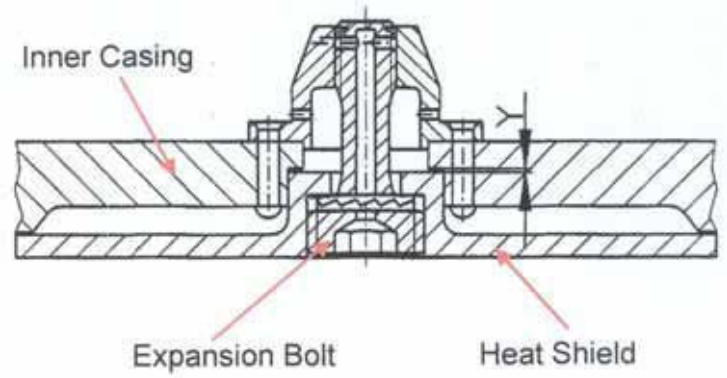

Figure 7. Geometry of the heat shield and bolt-setup.

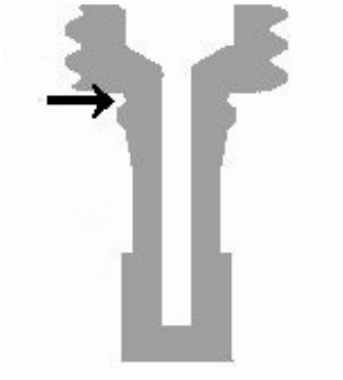

Figure 8. Schematic drawing of a bolt; the notch where failures have been found in German gas turbine bolts is marked with an arrow.

The failure was reported to happen at a notch right below the bolt head as shown in the schematic drawing in Figure 8.

An overview of the specimens available for metallurgical studies is shown in Table 2. Bolts B1 and B2 were as shown in Figure 8 while B3 had an extra cooling hole in the bottom of the bolt.

Table 2. Test specimens.

	Cooling hole	**Eqv. service hours / EOH**	**Number of starts**	**Estimated service temperature at bolt-head**
B1	no	89198	2279	500–550°C
B2	no	57100	543	
B3	yes	57100	543	
ref		0	0	N/A

3.1 Experimental procedures

Cross sections were prepared from all four bolts and studied in a light optical microscope (LOM) in order to look for signs of creep damage, and the oxidation of the surface of the service exposed bolts was studied in the scanning electron microscope (SEM).

The presence of the ordered Ni_2Cr phase described in the literature was investigated in a transmission electron microscope (TEM) using diffraction mode. TEM thin foils were prepared from different locations in all the bolts. Thinning of the foils was done by electropolishing in perchloric acid.

Finally part of the bolt B3 was sent to the materials research department (AFM) at Risoe National Laboratory for dilatometer testing.

3.2 Stereo microscopy and light optical microscopy

Investigation in the stereo microscope and in the light optical microscope indicated no presence of creep cavities or beginning creep failure neither at the notch where it has been found in German Nimonic 80A gas turbine bolts or anywhere else in the bolts. Figure 9 shows the microstructure of one of the service exposed bolts.

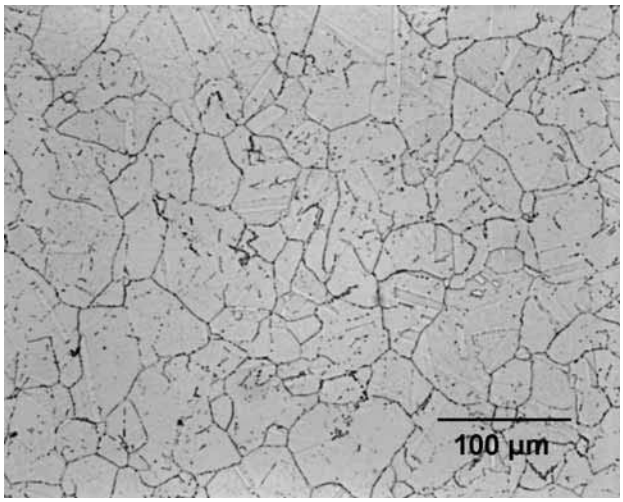

Figure 9. LOM micrograph of the microstructure of bolt B2; discrete carbide particles are located at grain boundaries.

3.3 Transmission electron microscopy (TEM)

TEM specimens revealed the presence of the ordered Ni_2Cr phase in all the bolts that have been in service. In the bolts that did not have a cooling hole running through the entire length of the bolt the ordered phase was only present in the lower part of the bolt, while it was present in the entire body of B3. The ordered phase was not found in any of the bolt-heads where the temperature has probably been too high for the ordered phase to be thermodynamically stable; also the ordered phase was not present in the reference bolt.

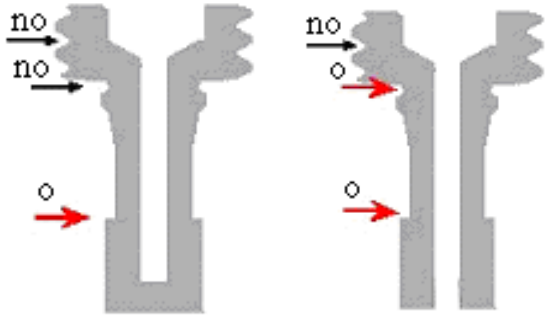

Figure 10. Schematic drawing of the bolts. The arrows indicate the locations from which TEM thin foils were prepared; arrows marked "no" indicates areas where ordering was not found (No Ordering) and arrows marked "o" indicates areas where the ordered phase was found.

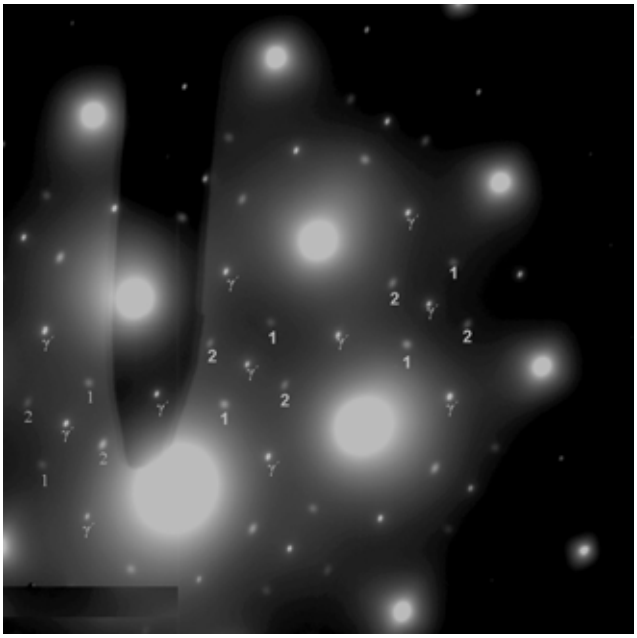

Figure 11. [001] Electron diffraction pattern from the lower part of bolt B1. 1 and 2 indicate diffraction points from two different Ni_2Cr super-lattices. γ´ indicates super-reflections from the Ni_3Al ordered phase.

The fact that the ordered phase is not present in the upper part of bolts B1 and B2 indicates that the temperature of this part has been above the critical temperature for the formation of the ordered Ni_2Cr phase. The extra cooling of bolt B3 has brought the temperature down to an area below T_c making the ordered phase energetically favorable.

3.4 Scanning electron microscopy (SEM)

Investigation of cross sections in the scanning electron microscope shows that the head of the bolts have seen a substantially higher temperature than the body of the bolts. It is clear that the heads are much more attacked by oxidation. Both surface and internal oxidation can be seen in the bolt heads (Figure 12), while the bolt body only shows signs of surface oxidation (Figure 13). This implies that the bolt heads have seen a higher service temperature than the other parts of the bolt.

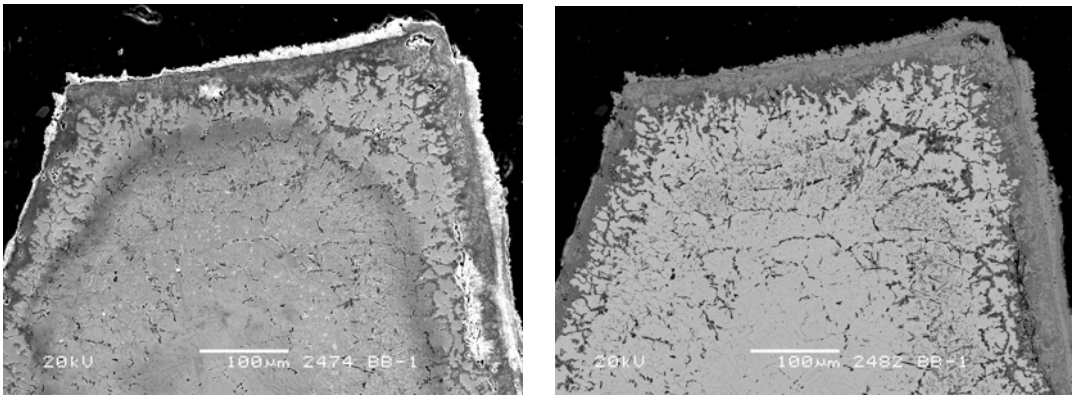

Figure 12. SEM images of part of the bolt head. The bolt head is heavily oxidized. (left) SE image and (right) BSE image of the exactly same area.

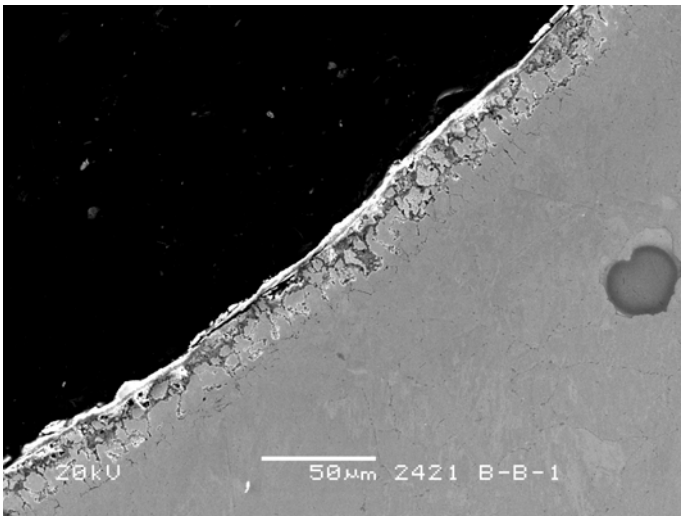

Figure 13. SEM SE image of the oxidation along the body of the same bolt shown in figure 12; notice the different scales.

This result corresponds nicely with the TEM results since it was speculated that the temperature in the bolt heads had been above the critical temperature for the formation of the ordered phase, while the body of the bolts had seen a lower service temperature.

3.5 Dilatometer

The material was heated up to 700ºC at a rate of 2ºC/min and the expansion of the material with temperature was recorded.

The tests show that the presence of the ordered phase indeed introduces a lattice contraction of about 0.1% in the lower part of the bolts.

Figure 16 shows the measured dilatometer curve for material from the lower part of bolt B3. During the first heating cycle an extra expansion is found due to the disappearance of the ordered phase at temperatures above T_c. After the specimen has been cooled to room temperature the experiment is repeated and the specimen is reheated. Now the extra expansion is no longer present in the curve (2nd cycle in Figure 14).

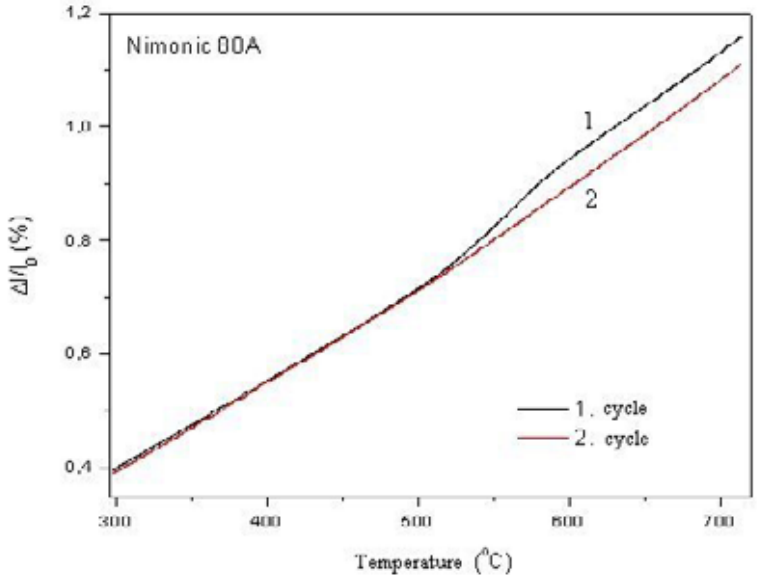

Figure 14. Dilatometer curve for lower part of B3.

This experiment shows that it is very easy to remove the ordering by holding specimens for a short while at a temperature above T_c. The second heating cycle does not show the same extra expansion because of the sluggish kinetics of the ordering formation. Like the initial formation of the ordering it will take several thousands of hours in the temperature regime 400–550ºC to again reestablish the ordering.

4. Discussion

The Nimonic 80A alloy does not normally suffer from excessive creep in the temperature regime 500–550ºC. However it has previously been found that negative creep in combination with an excessive prestraining of the bolts during tightening has led to failure of steam turbine bolts [6]. In the present case several different factors contribute and the sum of these factors may have led to the failure of the German gas turbine bolts.

Unlike steam turbine bolts the investigated bolts experience a temperature gradient during service. The temperatures are such that the Ni_2Cr ordered phase is thermodynamically stable in the lower part of the bolts but not in the bolt

heads. This leads to negative creep occurring in the lower part of the bolts but not in the bolt heads and will very likely result in a stress buildup in the exact area where the failure was found to initiate. Furthermore a notch is located at exactly this location (right below the bolt head) and acts as initiation site for the creep rupture. It is not believed that any of these factors by themselves can cause a failure, but the combination of differences in temperature, negative creep, the location of the notch and perhaps an initial overtightening may have lead to the observed failure of the German gas turbine bolts. The combination of factors contributing may also explain that the failure appeared as a typical creep failure, contrary to the brittle failures observed in steam turbine bolts.

5. Summary

Negative creep is the result of a solid-state transformation occurring during service or creep testing. For most applications the phenomenon is non-critical but for certain constrained components it may become critical.

For the alloy Nimonic 80A negative creep occurs due to ordering of the matrix phase resulting in the formation of the Ni_2Cr ordered phase. The negative creep is only observable after several thousand hours of exposure in the temperature regime 400–550ºC. The sluggish kinetics are probably caused by the deviation in composition from the 2:1 stoichiometry for Ni and Cr of the ordered phase. The ordering has in combination with other factors such as overtightening led to failure of steam turbine bolts.

A recent failure of Nimonic 80A gas turbine bolts in German gas turbines inspired an investigation of similar bolts from Danish gas turbines of the same type. Investigation in the TEM revealed the presence of the ordered phase in these bolts. The ordered phase was only found in the body of the bolts not in the bolt heads. This is because the temperature at the bolt heads was above the critical temperature for the ordering transformation.

It was shown by dilatometer experiments that the ordering transformation had resulted in a contraction of the lower part of the bolts of the order of size of 0.1%. It was also found that the ordering can be removed by a short heat treatment above the critical temperature for the ordering transformation.

It is believed that negative creep may have played a significant role in the failure of the German Nimonic 80A gas turbine bolts.

References

1. B. Reppich. Negatives Kriechen. Z. Metallkde. 75 (1984) 193.

2. R.W. Fountain & M. Korchynsky. The phenomenon of negative creep in alloys. Trans. ASM 51 (1959) 108.

3. K.H. Kloos, J. Granacher & H. Bartsch. Untersuchung des Kriechverhaltens hochwarmfester Gasturbinenwerkstoffe. Z. Werkstofftech 17 (1986), pp. 199–205.

4. E. Metcalfe, B. Nath & A. Wickens. Some effects of the ordering transformation in Nimonic 80A on stress relaxation behaviour. Materials Science and Engineering, 67 (1984), pp. 157–162.

5. E. Metcalfe & B. Nath. Proceedings of Conf. on Phase Transformations, York, 1979 Inst Metall. Conf. Ser. 3, 2(11) (1979) II-50.

6. S.M. Beech. 25 Years of experience of nickel based bolting materials. In: Strang, A. (Ed.) Performance of Bolting Materials in High Temperature Plant Applications, Conference Proceedings, 16–17 June 1994, York, UK. The Institute of Materials 1995. Pp. 259–270.

7. P. Vinders, R. Gommans, G. van Oppen & K. Verheesen. Brittle fracture of Alloy 80A stud bolts in a steam turbine. In: Strang, A. (Ed.) Performance of Bolting Materials in High Temperature Plant Applications, Conference Proceedings, 16–17 June 1994, York, UK. The Institute of Materials 1995. Pp. 271–283.

8. Marucco & B. Nath. Effects of ordering on the properties of Ni-Cr alloys. J. Materials Science 23 (1988), pp. 2107–2114.

9. A. Marucco & B. Nath. Effects of composition on ordering behaviour and rupture properties of Alloy 80A. In: High Temperature Materials for Power Engineering, Conference Proceedings, 24–27 September 1990, Liége, Belgium. Kluwer Academic Publishers 1990. Pp. 535–545.

10. Marucco and B. Nath. The effect of ordering on the high temperature deformation of nickel based alloys. In: Mechanical Behaviour of Materials – IV. Proceedings of the Fourth International Conference, 1984, 1, pp. 299–305.

11. S.M. Beech, S.R. Holdsworth, H.G. Mellor, D.A. Miller & B. Nath. An assessment of Alloy 80A as a high temperature bolting material for advanced steam conditions. Proceedings of Int. Conf. Advances in Material Technology for Fossil Power Plants, Chicago, 1987. Pp. 503–410.

12. A. Marucco. Atomic ordering in the Ni-Cr-Fe system. Materials Science and Engineering, A189, 1994, pp. 267–276.

13. K.H. Mayer & H. König. High temperature bolting of steam turbines for improved coal-fired power plants. Proceedings of Third International Conference on Improved Coal-Fired Power Plants (ICPP), San Francisco, 1991.

Appendix V

Identification of precipitates in IN792 after long time service exposure

- In Manuscript

Identification of precipitates in IN792 after long time service exposure

K. V. Dahl and J. Hald

Materials Technology, Dept of Manufacturing Engineering and Management,
Technical University of Denmark, DTU, Lyngby, Denmark.

Abstract

Plate-like precipitates were found in a service exposed IN792 gas turbine blade after service exposure for 40,000-60,000 hours in a temperature range of 680-760ºC. The precipitates were located in the metallic layer beneath the outer oxide layer formed during service.

Cross-sections prepared from the turbine blade was studied using LOM and SEM. EDS-composition measurements of the plate-like precipitates were compared with results of thermodynamic equilibrium calculations using Thermo-Calc. Composition profiles across the interface between bulk material and oxide layer show that there was significant diffusion of *Al*, *Cr* and *Ti* from bulk material and outward to the oxide layer. Therefore the influence of this diffusion on phase stability was investigated using the Thermo-Calc software.

The investigations proved inconclusive as to the exact nature of the precipitates and therefore a TEM thin foil was made using advanced FIB equipment. TEM/EELS investigations revealed that the precipitates were carbides and not σ-phase as first expected.

Introduction

At the high service temperatures in gas turbines the microstructure of nickel base superalloy components such as blades or vanes is degraded with time. Typical examples of microstructure degradation are coarsening of the strengthening γ'-phase; decomposition of primary carbides and precipitation of lower carbides; precipitation of intermetallic phases such as σ or μ depending on alloy chemistry.

The precipitation of brittle intermetallic phases is generally unwanted since it may have a deleterious effect on mechanical properties of components, where the brittle phases are known to act as initiation sites for fracture [1]. Usually these phases are avoided by carefully controlling the alloy chemistry. Interdiffusion with an applied coating, or outward diffusion of active elements to sustain a protective surface oxide layer may however cause local changes in chemistry towards compositions that favour the precipitation of these phases.

Since nickel base superalloys often contain more than 10 different chemical elements it can be very difficult to control the behaviour of the microstructure of a component under the complex interaction with the environment in the gas turbine in terms of stress, temperature and gas composition. Consequently, surprising features are sometimes found during service overhauls. The present work investigates such a case where precipitation of plate-like precipitates was found in a service exposed IN792 turbine blade. The main purpose of the work was to find the exact nature of the precipitates and possibly the mechanism behind their precipitation. Another purpose was to relate the experimental findings to results of thermodynamic equilibrium modelling and thereby test the accuracy of the thermodynamic database available for phase prediction.

Experimental details

The blade that initiated the current investigation was an uncoated, conventionally cast IN792 turbine blade that has run for 40,000 to 60,000 hours (the exact service time is not known) at a temperature of 680-760ºC. The average chemical composition for the IN792 material is shown in table 1. The blade did not have any internal cooling. Plate-like precipitates were found in the near surface regions, especially near the leading edge.

The blade was sectioned and standard metallographic procedures were used to cut, mount and polish specimens in cross-section. Specimens were then ground and diamond polished to 1 μm finish. For the light optical microscope (LOM) the specimens were etched using Kallings reagent to etch the bulk microstructure and Murakami etchant to etch the plate-like precipitates only. For work in the scanning electron microscope (SEM) the specimens were used in the polished condition and coated with approximately 50 nm evaporated carbon.

Table 1: IN792 specification from supplier

C	Cr	Co	Mo	Ti	W	B	Al	Hf	Ta	Ni
0.08	12.4	8.9	1.9	3.9	3.9	0.015	3.5	0.5	4.2	bal

Observations and EDS spectroscopy was carried out in a JEOL 5900 SEM operated under high vacuum conditions; the EDS system used was INCA 400 from Oxford Instruments. The experimental results were compared with results of thermodynamic modelling using Thermo-Calc [**2**] version Q. Calculations were done using the thermodynamic database for nickel base alloys Ni-DATA v. 4 developed by Thermotech ltd. [3].

Since the nature of the precipitates could not be conclusively proven using only SEM EDS measurements a TEM thin foil was made using focused ion beam milling (FIB) equipment located at Chalmers in Göteborg. The use of FIB equipment was necessary since the precipitation only occurred in a thin section near the surface making it impossible to make a conventional TEM thin foil. Electron energy loss spectroscopy (EELS) was done in a JEOL 3000F FEG transmission electron microscope equipped with an Oxford Instruments Inca Link ISIS EDS and Gatan Imaging Filter.

Experimental observations (LOM and SEM)

Plate-like precipitates were found in large amounts near the leading edge of the blade where also severe surface oxidation could be observed. In other areas of the blade smaller amounts of precipitates were observed in the area beneath the outer oxide layer. Fig. 1 shows a LOM image of a cross-section. A clear change in microstructure from surface to bulk material can be observed: The oxide layer (top of the image) is followed by a thin metallic layer where the γ' structure has disappeared and there are very few precipitates. Further into the bulk material plate-like precipitates are found, and finally at the bottom, the original IN792 microstructure with no plate-like precipitates.

Fig. 1: LOM image showing the change in microstructure from surface to bulk. The specimen was etched using Kallings reagent.

Fig. 2 shows LOM images of the area near the leading edge. The morphology of the precipitates is very typical for the brittle intermetallic *TCP* (topologically close packed) phases like σ which in almost all cases appear as plate-like precipitates in superalloys.

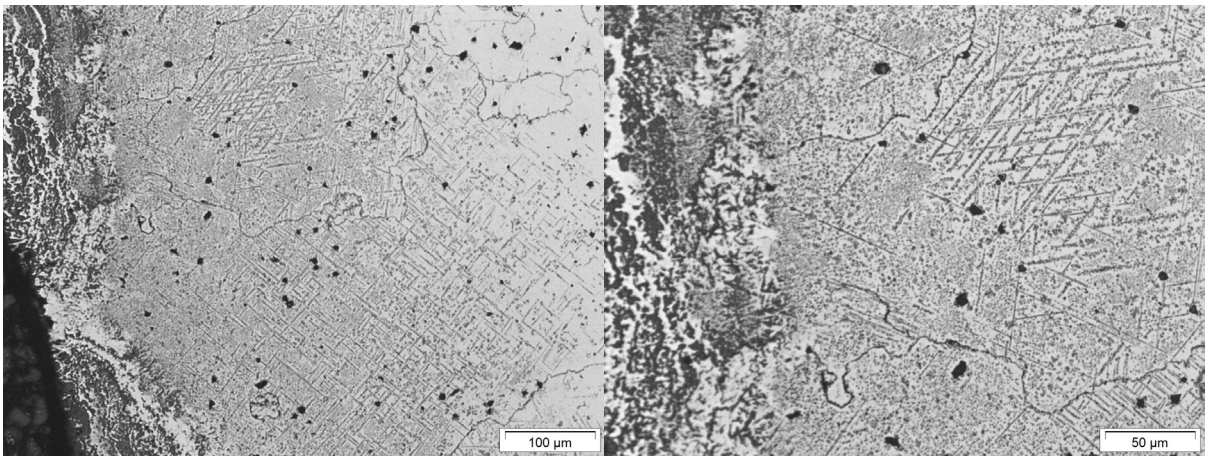

Fig. 2: Light optical micrographs showing plate-like precipitates in the area beneath the outer oxide layer.

The composition of the plate-like precipitates was measured using EDS spot analysis. The plate-like particles are very thin and therefore it is not possible to get an accurate analysis since there will also be some response from the matrix phase. It is however possible to see some trends. Fig. 4 shows a SEM micrograph using backscatter contrast of both plate-like and grain boundary precipitates. The location of EDS spot measurements are shown in the picture and the results are presented in table 2.

The EDS measurements show that the precipitates are rich in *Cr* which is consistent with σ-phase that has a typical composition of $(Cr, Mo)_x(Ni, Co)_y$, where x and y can vary from 1 to 7 [**1**], but the *Co* content seems to be lower in the precipitates than in the surrounding matrix, which is not expected for the σ-phase. X-ray mapping clearly shows the presence of *Cr* within the precipitates (Fig. 3).

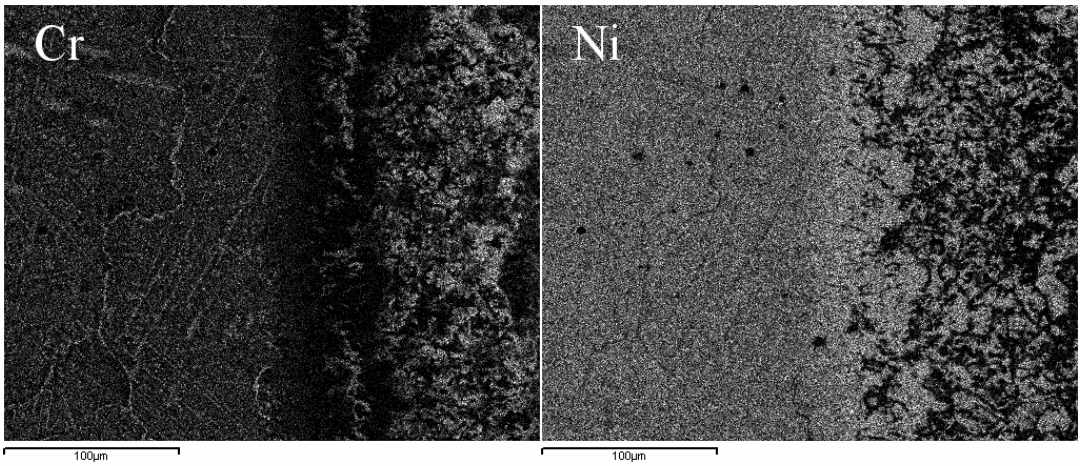

Fig. 3: *Cr* and *Ni* x-ray maps with the oxide layer located to the right in the images. The *Cr*-rich precipitates are clearly visible and also the *Cr*-depleted layer beneath the outer oxide layer.

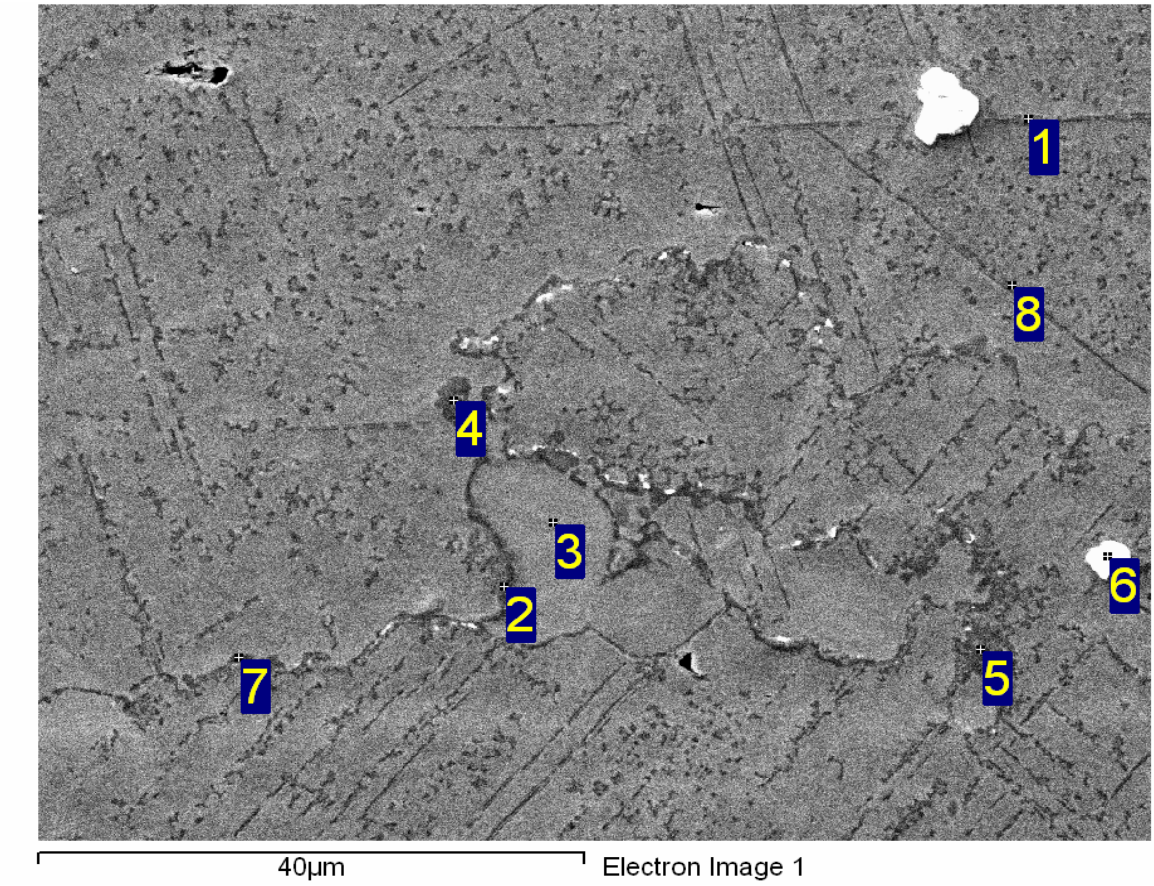

Fig. 4: SEM BSE image of plate-like precipitates with location of EDS measurement positions plotted.

Table 2: Results of EDS spot analysis in mass %.

Type	Nr.	Al	Ti	Cr	Co	Ni	Mo	Hf	Ta	W
Plate	1	2.1	2.8	32.2	7.5	43.1	3.9		2.0	6.4
Plate	8	2.3	2.9	34.2	6.7	40.8	4.6		2.1	6.4
GB	2	1.7	2.3	48.3	4.0	30.2	6.3			7.2
GB	4	2.7	3.1	31.9	5.2	43.1	5.2		2.2	6.6
GB	5	1.4	3.0	42.5	3.5	35.5	6.6			7.5
GB	7	~0.7	1.2	58.4	4.7	19.8	7.7			7.5
γ′	3	4.5	7.0	3.4	4.8	68.4		2.4	7.0	2.5
MC	6		25.4	1.4	~0.7	4.0	3.1		54.8	10.6
Area	Area	3.0	4.6	11.9	8.7	58.6	2.3		6.9	4.0

The grain boundary precipitates and plate-like precipitates show the same trends. Compared to the overall composition the precipitates contain higher amounts of *Mo* and *W* and lower amounts of *Ni* and *Co*.

$M_{23}C_6$ is also very rich in *Cr* and has been known to precipitate with the same morphology as *σ*-phase in some cases [4]. Distinguishing between *σ*-phase and $M_{23}C_6$ can however be difficult in the SEM, since it is not possible to measure for *C* using EDS. The dark contrast of the precipitates in BSE mode indicate that the mean atomic number of the precipitates is lower than that of the matrix, which could be an indication that they are carbides.

The distribution of elements near the oxide layer was investigated from x-ray elemental-maps. Composition profiles were plotted from the intensity information stored in the images; this was possible using the grey scale conversion method described in a previous article [5]. The profiles that are shown in Fig. 5 show that significant diffusion of *Cr*, *Al* and also *Ti* takes place towards the oxide layer at the surface. Underneath the oxide layer there is a metallic zone depleted of *Cr* and *Al*. The plate-like precipitates are then found in the area beneath this depleted zone.

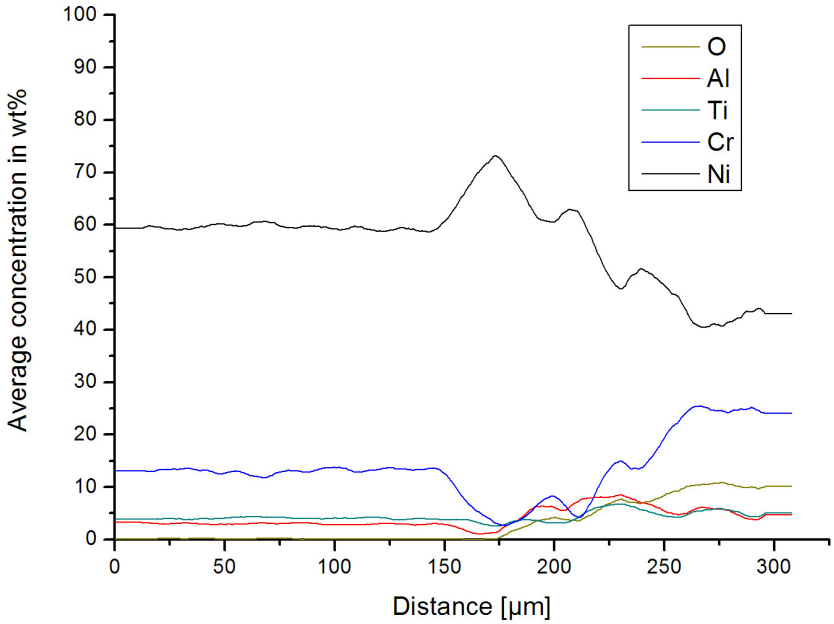

Fig. 5: Composition profiles for chosen elements for the area shown in the BSE SEM image in Fig. 3. The profiles were measured using the method described in [5] and applying a smoothening procedure.

Thermodynamic modelling

Thermodynamic modelling was done using Thermo-Calc version Q with the superalloy database Ni-DATA v. 4 developed by Thermotech ltd. [3]. Calculations were set up using the specified composition shown in table 1 and done considering the phases γ-fcc, γ', $M_{23}C_6$, M_7C_3, M_6C, MC and σ. The calculations predict that σ-phase is thermodynamically stable up to approximately 770ºC (Fig. 6).

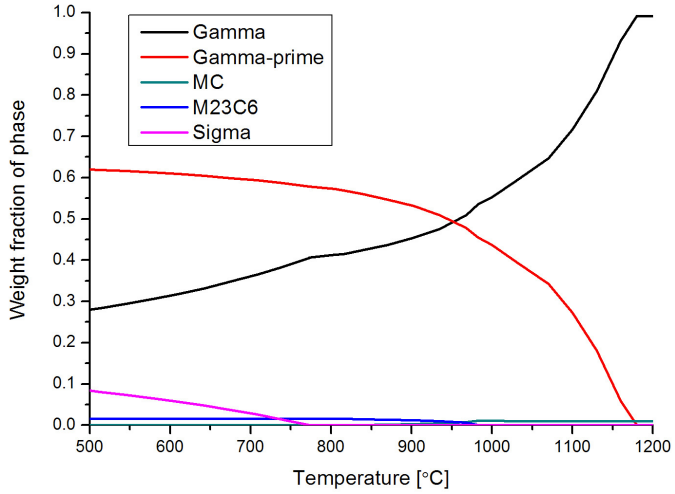

Fig. 6: calculated phase fractions as a function of temperature.

For comparison with EDS composition measurements the predicted compositions of stable phases at 700ºC are presented in Table 3.

Table 3: Calculated phase compositions in mass%.

	C	Al	Ti	Cr	Co	Ni	Mo	Hf	Ta	W
FCC	-	0.5	0.1	24.9	15.2	50.2	3.1	-	0.2	5.8
γ′	-	5.6	6.5	1.6	4.7	70.1	0.2	0.8	7.0	2.9
$M_{23}C_6$	5.1	-	-	68.7	2.1	4.2	18.5	-	-	1.4
σ	-	-	-	48.8	20.0	16.0	12.9	-	-	2.4

The calculated composition of *γ′* is in excellent agreement with the experimental measurement thought to be *γ′* (measurement 3 in table 2). The measured chromium content of both plate-like precipitates and grain boundary precipitates is low compared to the calculated value for $M_{23}C_6$ but fits quite well with the content calculated for *σ*. The measured trend with lower *Co* content in the precipitates than for the overall composition does however not match with calculated results for *σ*-phase where a higher *Co*-content is predicted.

When doing spot analysis of a precipitate in the SEM the measured results may contain a response from the matrix surrounding the precipitate if the electron interaction volume is larger than the size of the precipitate. In the present case the matrix contains less chromium but more cobalt than the precipitates. This could influence the measured values in the way that the measured chromium content of the precipitates would be lower than the actual content while the measured cobalt value would be higher. This effect can therefore explain that the measured chromium content is lower than the calculated contents of both *σ* and $M_{23}C_6$. It can however not explain the low cobalt content of the precipitates. Therefore if the thermodynamic data used for the calculations are accurate this points in the direction that the precipitates are actually carbides.

At 700ºC the thermodynamic equilibrium calculations predict that the IN792 alloy lies within the *γ*, *γ′*, $M_{23}C_6$ and *σ* phase area (Fig. 7). The amount of *σ*-phase in the calculations follows the *Cr*-content. It would therefore be expected that if the precipitates were actually *σ*-phase then an increased *Cr*-content would be visible in the composition profiles in Fig. 5 in the area where the precipitates are found. This is not the case. The amount of $M_{23}C_6$ follows the *C*-content but this could not be measured using EDS-equipment.

The combination of SEM investigations and calculated results therefore seem to indicate that the precipitates are carbides.

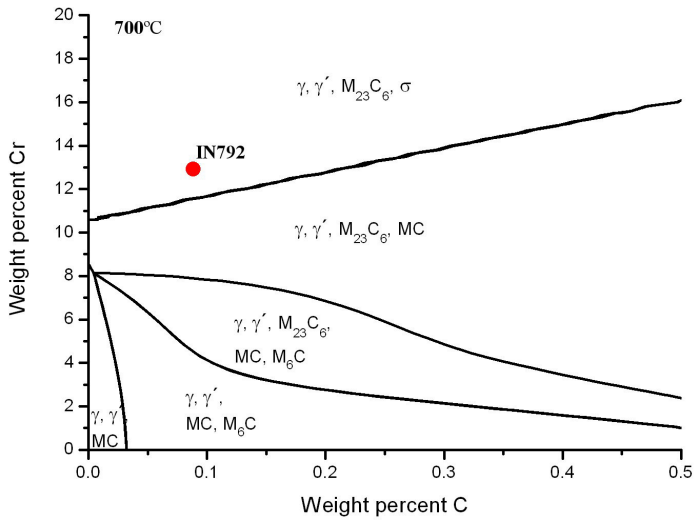

Fig. 7: Calculated isothermal diagram for 700ºC showing the influence of varying *Cr* and *C* content with *Ni* as dependent variable.

Experimental observations (TEM, EELS)

In order to experimentally verify the indications from the thermodynamic equilibrium calculations, a TEM thin foil was made with FIB equipment using the lift out technique, which allows controlled localised sampling. A SEM image of the final thin foil can be observed in Fig. 8. The plate-like precipitates are clearly visible in the image, a larger more bulky particle can also be observed.

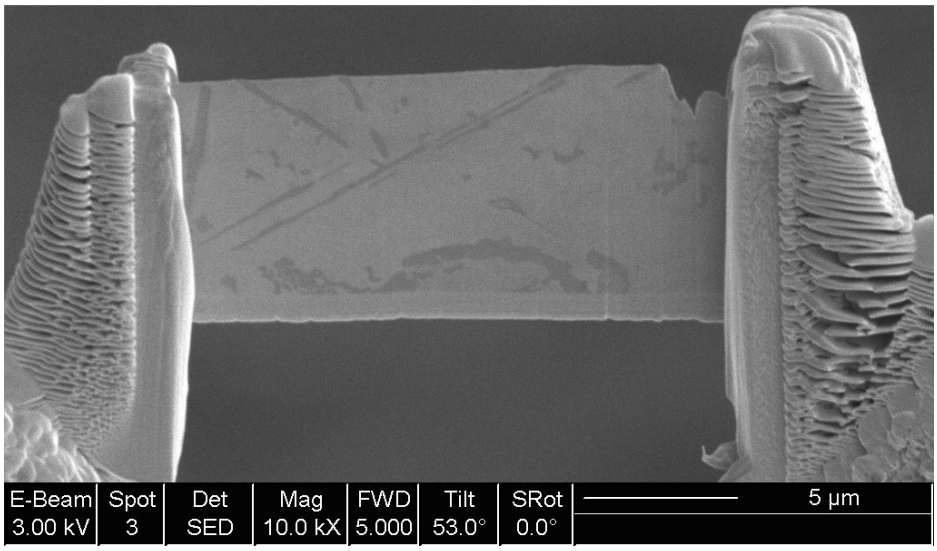

Fig. 8: TEM thin foil made using focused ion beam milling.

Electron energy loss spectroscopy (EELS) was then used to map the chemical distribution of selected elements. From Fig. 9 it is again clearly seen that the plate-like precipitates are rich in *Cr,* and in the background *Ni*-rich *γ′*-particles can be observed.

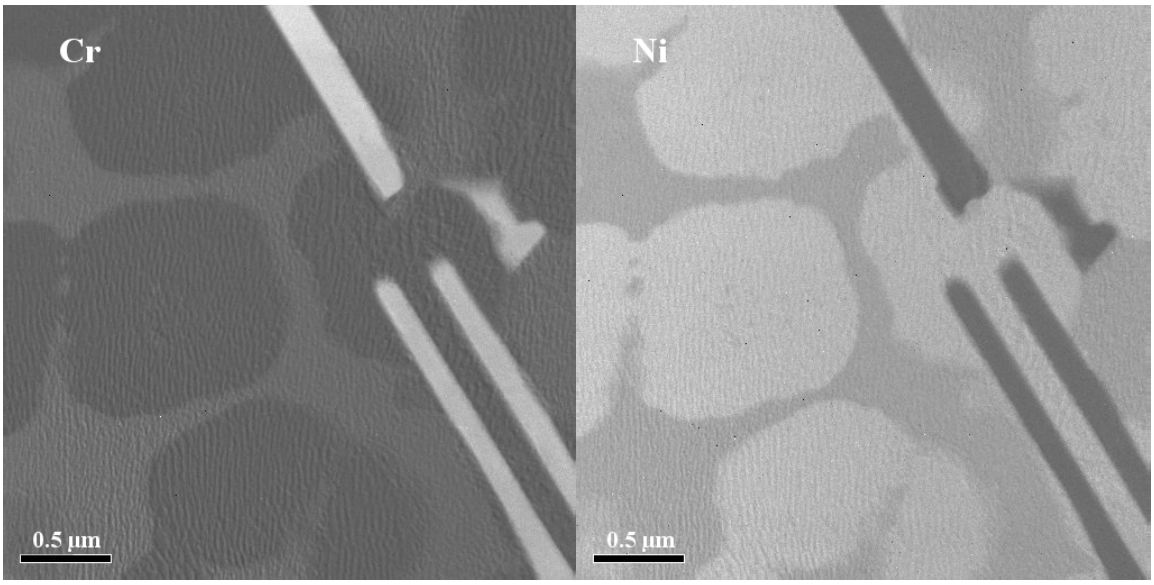

Fig. 9: EELS elemental maps showing *Cr* (left) and *Ni* contrast (right). The *Cr*-rich plate-like precipitates can easily be identified along with cuboidal *γ′*-particles rich in *Ni* and low in *Cr*.

In the same manner chemical imaging can be used to see if the precipitates contain carbon. Fig. 10 shows chemical image maps of the distribution of *C* and *Ti*. The bright contrast in the *C* maps indicate that they are rich in *C*, and therefore that the precipitates are carbides. Another interesting feature was observed since the image maps indicate that the plate-like precipitates grow next to *Ti*-rich primary carbides also visible in the images. At the service temperature (~700ºC) the primary carbides are thermodynamically unstable but only dissolve very slowly. The carbon released when they dissolve is then precipitated in secondary carbides. This must however be expected to occur in the same manner at all locations in the turbine blade since it is not internally cooled, and can therefore not explain the local precipitation of a large amount of secondary carbides.

Instead the mechanism suggested by Berthod et al. [4] seems likely: During service secondary carbides formed during the initial heat treatment, which are located near the outer surface are dissolved because of diffusion of *Cr* towards the oxide layer. The carbon released by this process diffuses in the opposite direction into the bulk material and results in an increased amount of secondary carbides in the area right beneath the *Cr* depleted zone. For the present case it is expected that diffusion of *Ti* towards the oxide layer will also result in a faster

dissolution of the primary *Ti*-rich carbides in the surface area, resulting in even more *C* being able to diffuse inwards.

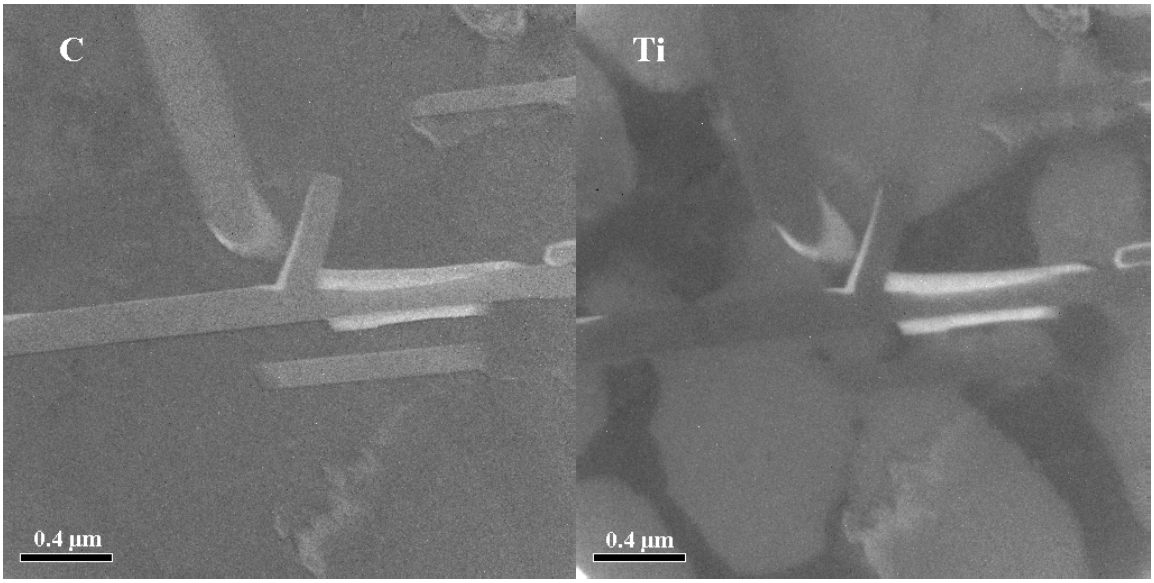

Fig. 10: EELS elemental maps showing *C* (left) and *Ti* contrast (right). The plate-like particles are rich in *C*, and often grow next to *Ti*-rich particles also containing *C*.

Conclusions

A combination of SEM EDS investigations and thermodynamic modelling indicated that the precipitates were carbides, but more experimental proof was needed in order to be conclusive. This was gained from chemical imaging using EELS. In the process of making a suitable TEM thin foil from the local area where the precipitates were found it was necessary to use FIB equipment.

The experimental investigations revealed that the precipitates found in the turbine blade were chromium rich carbides and not σ-phase as initially expected from the morphology of the precipitates. The combined approach using SEM EDS measurements and thermodynamic modelling was therefore able to point in the correct direction, even though the thermodynamic data predicted both σ-phase and $M_{23}C_6$ carbides to be thermodynamically stable.

It seems likely that the carbide precipitation is caused by inward diffusion of carbon. The carbon is released from a chromium depleted zone right beneath the oxide layer where the carbides present in the initial microstructure are dissolved because of the outward diffusion of *Cr* and *Ti* into the oxide layer.

Acknowledgements

The authors wish to thank:

Fredrik Karlsson from Demag Delaval Industrial Turbomachinery AB, Finspong, Sweden for providing specimens.

A. Hansson from Dept. of Manufacturing Engineering and Management, Technical University of Denmark and Jonathan Weidow from Chalmers University, Göteborg, Sweden for help preparing the TEM thin foil using FIB.

F. Grumsen and H. Danielsen both from the Dept of Manufacturing Engineering and Management, Technical University of Denmark for help with TEM and EELS investigations.

References

[1] C.T Sims and W.C. Hagel: *The Superalloys*, John Wiley & Sons, USA, 1972.
[2] B. Sundman, B. Jansson and J. -O. Andersson, *Calphad*, 1985, **9** (2), 153-190.
[3] N. Saunders, *SUPERALLOYS 1996 - Procedings of the Eight International Symposium on Superalloys*, Champion, Pennsylvania, 1996, 101-110. Edited by R. D. Kissinger et al.
[4] P. Berthod, S. Michon, J. Di Martino, S. Mathieu, S. Nöel, R. Podor and C. Rapin: *Computer Coupling of Phase Diagrams and Thermochemistry*, 2003, **27** 279-288.
[5] K.V. Dahl. J. Hald and A. Horsewell: *Material submitted to Journal of Microscopy*.